A mobile, high-precision atom-interferometer and its application to gravity observations

D I S S E R T A T I O N

zur Erlangung des akademischen Grades
doctor rerum naturalium
(Dr. rer. nat.)
im Fach Physik

eingereicht an der
Mathemathisch-Naturwissenschaftlichen Fakultät
Humboldt-Universität zu Berlin

von
Dipl.-Phys. Matthias Hauth

Präsident der Humboldt-Universität zu Berlin:
Prof. Dr. Jan-Hendrik Olbertz

Dekan der Mathemathisch-Naturwissenschaftlichen Fakultät:
Prof. Dr. Elmar Kulke

Gutachter:
1. Prof. Achim Peters, Ph.D.
2. Prof. Dr. Oliver Benson
3. Prof. Dr. Holger Müller

Tag der mündlichen Prüfung: 06.03.2015

Abstract

Atom interferometry offers a very precise and sensitive measurement tool for various areas of application whereof one is the registration of the gravity acceleration. While the vast majority of atom interferometers include large and stationary setups, this field very often implies the additional request for a mobile apparatus. The Gravimetric Atom Interferometer (GAIN) project has been started to meet this requirement and to provide best possible accuracy at the same time. It aims to realize an alternative to other types of gravimeters and to combine important qualities such as high sensitivity and absolute accuracy in one instrument.

The GAIN sensor is based on laser-cooled ^{87}Rb atoms in a 1 m atomic fountain. Stimulated Raman transitions form a Mach-Zehnder type interferometer which is sensitive to accelerations. In this work it has been advanced to meet all requirements for mobile and drift-free long-term operation. Therefore, selected parts of the laser system have been improved or redeveloped. A second focus has been on systematic effects for the same objective. They have been analyzed and measures for their suppression have been undertaken.

The apparatus has been transported, tested in relevant environments, and compared to the most important state-of-the-art gravimeter types where a competitive performance has been achieved. It is demonstrated, that the gravity signal of this sensor allows for a precise calibration of the relative gravimeter types. During the measurements a best sensitivity of $138\,\mathrm{nm/s^2}/\sqrt{\mathrm{Hz}}$ and a stability of 5×10^{-11}g after 10^5 s has been reached.

Zusammenfassung

Atom Interferometrie ist eine sehr genaue und sensitive Methode mit einer Vielzahl von Anwendungsmöglichkeiten, zu der auch die Messung der Erdbeschleunigung zählt. Während die meisten Atom Interferometer aus großen, ortsfesten Aufbauten bestehen, werden auf diesem Gebiet häufig mobile Messgeräte benötigt. Das Gravimetric Atom Interferometer (GAIN) Projekt wurde ins Leben gerufen, um dieser zusätzlichen Anforderung bei bestmöglicher Messgenauigkeit gerecht zu werden. Es soll eine Alternative zu anderen modernsten Gravimetertypen geschaffen werden, die wichtige funktionale Eigenschaften wie eine hohe Auflösung und absolute Genauigkeit in einem Gerät vereint.

Der GAIN Sensor verwendet lasergekühlte ^{87}Rb Atome in einer 1 m hohen Fontäne. Mit Hilfe von stimulierten Raman Übergängen wird ein beschleunigungssensitives Interferometer realisiert. In dieser Arbeit wurde der Sensor mit Blick auf mobile und driftfreie Langzeitmessungen weiterentwickelt. Dafür wurden einzelne Subsysteme des Laseraufbaus auf die daraus resultierenden Anforderungen hin angepasst oder neu entwickelt. Mit derselben Zielstellung wurden weiterhin systematische Effekte in dem Messaufbau untersucht und Maßnahmen für ihre Reduzierung realisiert.

Der Aufbau wurde transportiert und in relevanten Umgebungen getestet. Dabei konnte gezeigt werden, dass die Leistungsfäigkeit dieses Aufbaus mit denen der wichtigsten und modernsten Gravimeter konkurieren kann, sie teilweise übertrifft und dass dieser Sensor zur präzisen Kalibrierung der relativen Gravimeter verwendet werden kann. In den Messungen wurde eine Sensitivität von $138\,\mathrm{nm/s^2/\sqrt{Hz}}$ sowie eine Langzeitstabilität von 5×10^{-11}g über 10^5 s erreicht.

Contents

1. Introduction

The gravitational force is one of four fundamental interactions in physics. Though it is about 10^{29} to 10^{38} times smaller than the electromagnetic, the weak, and the strong interaction, it plays an important role on macroscopic scales such as in the field of cosmology. But also in everyday life we are familiar with this force. All matter, including ourselves, fall back to Earth if not dominated by other forces. Observations done over the course of several hundred years led to a profound description of this force. Important milestone were the examinations of the free fall made by Galileo and his conclusion that all matter is accelerated at the same rate. The first complete mathematical description was given by Sir Isaac Newton in his famous work "Philosophiæ Naturalis Principia Mathematica" in 1687. Newton's law of universal gravitation describes the attracting force F_g between any two bodies which is proportional to their masses m_1 and m_2

$$F_g = G\frac{m_1 m_2}{r^2} \tag{1.1}$$

where G denotes the gravitational constant and r the distance between the centers of the masses. The gravitational force has some characteristic properties: It is always attractive, has infinite range, and it cannot be shielded. By now, Newton's law of universal gravitation can be seen as an approximation of Einstein's general theory of relativity which is the current theory of gravitation. It holds very precise in the limits of low mass densities and non-relativistic velocities [1, 2].

Equation (1.1) includes four parts which have been, in parts intensively, investigated in the past and are still matter of ongoing research. These are:

The gravitational constant G has been measured by a large number of experiments but still is the fundamental constant with the by far largest inaccuracy [3, 4].

The inverse-square law describes the decreasing strength with the distance r between the masses. Possible violations have been tested on different length scales [4–6].

The gravitational acceleration $a_g = F_g/m_1 \propto \sum_n m_{2,n}/r_n^2$ an object with mass m_1 is subjected to is the consequence of the gravitational force. The latter is determined by the distribution of all masses $m_{2,n}$ of the near and also the far environment at distances r_n. Thus a precise investigation of this force or the corresponding acceleration gives the sum over all masses weighted with their distances. Temporal and spatial observations can allow to draw conclusions, e.g., on the mass distribution above and below the surface of the Earth and thereby on its composition [7–9].

The weak equivalence principle, also known as the universality of free fall (UFF) or as the Galilean equivalence principle, states that "the motion of any freely falling test particle is independent of its composition and structure" [2]. It is one important aspect of general

relativity. In combination with Newton's second law of motion $F = m_i a$ the equivalence between the inertial mass m_i and the gravitational mass of the test particle m_1 in Eq. (1.1) can be tested.

For studies of all four aspects of the gravitational law it is necessary to measure either the gravitational force F_g or the consequent gravitational acceleration a_g which acts on the test mass m_1. A variety of experimental apparatus have been developed during the last centuries to investigate one or the other. Atom interferometers are one of the newest devices which are among other things sensitive to accelerations. Here, their application to gravity observations, which include the aspect of the gravitational acceleration, will be covered.

1.1. Gravity and its variations on Earth

All matter on Earth is subjected to the gravitational acceleration. However, the acceleration which can be observed includes a second contribution which cannot be avoided. The Earth is a non-inertial reference frame because of its rotation and causes a centrifugal force

$$F_z = m\omega^2 d. \tag{1.2}$$

Here, m denotes the observed mass, ω the rotation rate, and d the distance between the mass and the rotation axis of the Earth. The sum of both forces determines the acceleration all matter is subjected to. Throughout this thesis and in accordance with literature [8, 9] the term "gravity acceleration" or shorter "gravity" will denote the combined effect of the gravitational acceleration and the centrifugal acceleration due to Earth's rotation. The instruments used for measuring the gravity value are gravimeters.

Gravity acceleration is altered by a variation of influences in time and space. Global variations on Earth can already be visible at the second decimal place. The difference in gravity between, e.g., Berlin-Adlershof and Wettzell in the Bavarian Forest, two locations where measurement campaigns have been performed during this thesis, amounts to 4×10^{-4} g. Regional variations, on the other hand, are typically on the order of 10^{-6} g. Temporal influences are even slightly smaller. The largest one is the basic tidal effect reaching magnitudes of up to almost 3×10^{-7} g, whereas the effects of mass redistributions in the atmosphere or below the surface of the Earth and also of man-made changes are again smaller.

An overview of the different effects and their magnitudes is given in Fig. 1.1. Short introductions into the physics of the Earth tides and the interest in resolving the effect of mass redistribution are given in the following.

Tidal effect

The Earth is attracted by the gravitation arising from external bodies like the sun, the moon, and to a minor extend other planets. Due to the inverse-square law the resulting acceleration is non-homogeneous throughout the Earth but changes with position. On the other hand, the whole Earth underlies an orbital acceleration which is connected to its orbital motion. Both

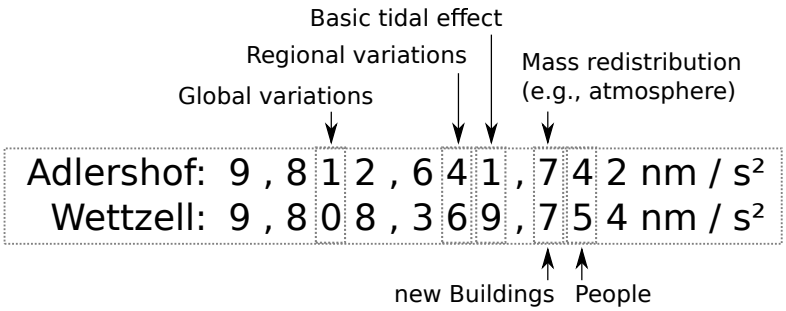

Figure 1.1.: Gravity acceleration measured within this work in Berlin-Adlershof and Wettzell (Bavaria). The values are influenced by a variety of effects causing changes at different decimal places which are indicated by the arrows.

accelerations exactly match at a certain point in general and for a spherical symmetric Earth in its center of mass. At other locations their difference gives a remaining tidal acceleration [9, 10].

The tidal effect is visualized in Fig. 1.2 for a simplified system with a non-rotating Earth and its Moon. Both bodies orbit around their common barycenter resulting in the Earth's orbital acceleration which only coincides with the gravitational acceleration $\boldsymbol{a}_O$ in the Earth's center of mass O. At a point P located at the Earth's surface the local gravitational acceleration a differs. Here, the difference of both accelerations results in the tidal acceleration a_t, which can be expressed using Newton's gravitational law as

$$\boldsymbol{a}_t = \boldsymbol{a} - \boldsymbol{a}_O = \frac{GM_m}{d^2}\frac{\boldsymbol{d}}{d} - \frac{GM_m}{r^2}\frac{\boldsymbol{r}}{r} \tag{1.3}$$

where G, $\boldsymbol{d}$, and $\boldsymbol{r}$ denote the gravitational constant and the distances between point O and the Moon and point P and the Moon respectively. As a result the tidal effect lowers gravity on the side of the Earth facing the Moon as well as on the opposite side and the acting forces cause elastic deformations of the Earth's shape which can reach up to 40 cm.

In addition, a semidiurnal and diurnal variation is induced by the Earth's rotation which then causes the well-known rise and fall of sea levels. The moving water masses themselves give an additional contribution to gravity variations by direct attraction (ocean tides) and also by loading effects which again cause elastic deformations of the Earth's shape (ocean load tides). The latter are subject to phase leads. Even more temporal variations are introduced by changing distances between the Earth and the Moon and between the Earth and the Sun as well as by seasons and lunar phases. All effects together result in a variety of semidiurnal, diurnal, and long-period tides.

Tidal effects can be calculated using theoretical models together with ephemerides of celestial bodies and local parameters obtained from former gravity observations, see Appendix A. Thus, gravimetric measurements can be reduced for these dominating temporal effects and other influences become visible.

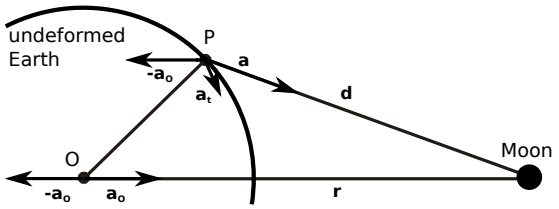

Figure 1.2.: Emergence of the tidal effect caused by the moon.

Polar motion

The Earth's rotation axis is subjected to slight temporal variations of its orientation relative to the Earth's surface. Their intersection points (poles) move several meters per year with periodic and long-term drift components. As a consequence the distance between a fixed location on the Earth's surface and the rotation axis also evolves over time and thereby the resulting centrifugal acceleration undergoes temporal changes. The latter are typically within $\pm 50\,\mathrm{nm/s^2}$ in Northern Germany [12]. They can be calculated using Earth observation parameters from the International Earth Rotation and Reference Systems Service (IERS) and then be reduced from gravity observations.

Mass redistribution

Mass redistributions above as well as below the surface of the Earth occur due to a variety of causes. They change the local gravity acceleration according to Eq. (1.1) and their influence typically reaches magnitudes of a few times $10^{-8}\,\mathrm{g}$. One important aspect is the influence of atmospheric mass variations which we were also able to observe during our measurements. It causes gravitational attraction and also an additional loading effect. The latter vertically deforms the crust and mantle of the Earth. The atmospheric variations at the same time cause changes of the local air pressure which can be used in a simple model for corrections. Applying the correlation

$$g_{\mathrm{atm}} = a_{\mathrm{atm}}(p - p_0) \tag{1.4}$$

with the admittance factor $a_{\mathrm{atm}} \approx 3.0\,\mathrm{nm/s^2/hPa}$ and the normal atmospheric pressure p_0 for the specific height, the main part of the effect can be removed. Other mass redistributions are induced, e.g., by rainfall and hydrology. Here, observations with gravimeters can be of interest to get further insights and support other methods like water table observation wells. Beyond that general studies of mass convections below the surface of the Earth are of interest in geodynamics where amongst others magma transport and tectonic plate movements are investigated [13, 14].

Free air gravity gradient

The inverse square law in Eq. (1.1) causes the gravity value to decrease with the height h. This results in a vertical gravity gradient in free air of $\gamma = \frac{\partial g}{\partial h} \approx 3080\,\mathrm{nm/s^2/m}$ near the surface of the Earth [9].

1.2. Gravimeters based on atom interferometry

1.2.1. Atom interferometry

Atom interferometers were realized almost in parallel by different research groups in the early 1990s. They achieved the coherent splitting and recombination which are necessary to observe interference with the help of various experimental implementations. Two of the groups worked with micro-fabricated structures of which one was similar to Young's double slit [15] and the second a transmission grating [16]. The other approaches used laser waves in a traveling wave configuration [17] and in a pulsed configuration with stimulated Raman transitions [18]. Thereafter, especially atom interferometers with laser waves as beam splitters had been increased in their sensitivities and were used for precise measurements of the fine structure constant [19, 20] and of the gravitational constant [21–24]. The principle was also employed in different configurations for precise inertial sensors like gyroscopes [25–27], accelerometers and absolute gravimeters [28–30], and gravity gradiometers [31]. The latter are able to measure gravity gradients.

The experiments demonstrated that the possible sensitivities and absolute accuracies are competitive to state-of-the-art instruments which are based on different working principles. For gravimeters based on this principle, the best reported sensitivities so far are $230\,\mathrm{nm/s^2/\sqrt{Hz}}$ [29], $80\,\mathrm{nm/s^2/\sqrt{Hz}}$ [32], and recently for a measurement in a particular quiet seismic environment $42\,\mathrm{nm/s^2/\sqrt{Hz}}$ [33]. While most atom interferometers are constrained to fixed laboratories, several approaches have been started to develop mobile devices. The idea is to make inertial sensing based on atom interferometry applicable to, e.g., navigation and geophysics [34–36].

Further possible fields of application are fundamental precision measurements for testing general relativity [37–39]. Ground based tests of the UFF already achieved Eötvös ratios $\eta = \Delta g/g$ of $(1.2 \pm 3.2) \times 10^{-7}$ and $(0.3 \pm 5.4) \times 10^{-7}$ for the combinations $^{85}\mathrm{Rb}-^{87}\mathrm{Rb}$ [40] and $^{87}\mathrm{Rb}-^{39}\mathrm{K}$ [41] respectively. Studies for space missions propose to drastically increase the accuracy by several orders of magnitudes mainly due to extended times of free evolution between the interferometer pulses. Within several European Space Agency (ESA) projects a compact atom interferometry demonstrator (Space Atom Interferometer (SAI) project [42]) and further concepts for sensors in space (Space-Time Explorer and Quantum Equivalence Principle Space Test (STE-QUEST) [43, 44]) have already been developed. Another concept describes the possibility to detect gravitational waves with the help of atom interferometers in space [45].

1.2.2. Working principle

The atom interferometer discussed in this work is based on stimulated Raman transitions [18] which are applied to a cold ensemble of rubidium-87 atoms inside a ultra-high vacuum (UHV) chamber. The atoms are laser-cooled in a magneto-optical trap (MOT) and a subsequent optical molasses to about $2\,\mu\mathrm{K}$ in order to realize low velocities and long observation times of the cloud of nearly 1 s. In comparison to a light interferometer the roles of light and matter are interchanged. After preparation the atoms are coherently transferred to a superposition of two internal energy states with different external momenta. As a consequence the states evolve onto two different paths. Afterwards, they are redirected and finally recombined. The necessary beam splitters and mirrors are realized by means of laser light pulses which drive the atomic transition ω_a between

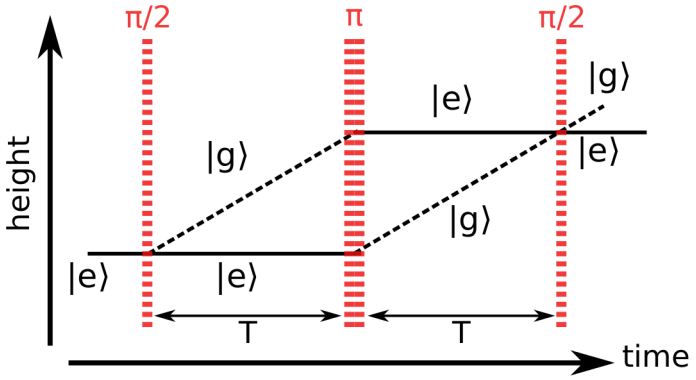

Figure 1.3.: Mach-Zehnder type atom interferometer with three Raman light pulses ($\pi/2-\pi-\pi/2$ sequence). The first pulse creates a superposition of two internal states $|g\rangle$ and $|e\rangle$ with different momenta. They evolve onto separate paths. The second and third pulse reflect the paths and close the interferometer.

the two hyperfine states. Therefore, the frequency difference of two laser beams $\omega_1-\omega_2$ is tuned to be in resonance with the atomic transition. The single laser beams are not in resonance with any transition but near the D_2 ($5^2S_{1/2} \rightarrow 5^2P_{3/2}$) transition at a wavelength of 780 nm. If an atom undergoes the Raman transition a photon of one light field is absorbed while at the same time the emission of another photon is stimulated by the other light field. This way energy and also momentum are transferred to or extracted from the atom depending on its initial state.

In a Mach-Zehnder type atom interferometer, which is used in this work, three Raman light pulses are applied, see Fig. 1.3. After the atoms have been prepared to be all in the same internal state, the first pulse transfers each of the atoms into a superposition of the two hyperfine states $|g\rangle$ and $|e\rangle$. Its light intensity and pulse length are tuned to reach equal probabilities of occupancy for both states ($\pi/2$ pulse). As a consequence the different states spatially separate, due to the transferred momenta, onto two paths. After a time T a second pulse with double length (π pulse) is applied. It inverts both the internal state and the external momentum the atoms have on the two paths. The latter meet again after another time T. The third pulse, which is again a $\pi/2$ pulse, finally closes the interferometer. The splitting between the paths and the phase sensitivity becomes maximal for counter-propagating laser beams.

At the output, interference can be observed. The resulting state population depends on the phase difference $\Delta\phi$ between the two paths and the probability of the atoms to be transferred to the other internal state is given by

$$P = \frac{1}{2}(1-\cos\Delta\phi). \tag{1.5}$$

$\Delta\phi$ includes contributions from the exact paths in space as well as from the interaction of the atoms with the Raman laser pulses.

Atom interferometers can be used to measure influences on their phase very precisely. Depending on the implemented configuration a variety of different effects, e.g., rotations or accelerations due to gravitational or other forces, can be observed. In order to use atom interferometers for

high-precision experiments it is necessary to obtain a very good control on laser phases and to suppress all but the desired influence to a sufficient level. A configuration with free falling atoms along the vertical direction and anti-parallel laser beams which are aligned along the same axis allows to measure gravity acceleration [28, 46]. The latter causes a phase shift of

$$\Delta\phi \approx \boldsymbol{k}_{\text{eff}}\boldsymbol{g}T^2 \tag{1.6}$$

where $\boldsymbol{g}$ is the gravity acceleration, $\boldsymbol{k}_{\text{eff}}$ the effective wave vector resulting from the Raman laser beams, and T the time between consecutive laser pulses. Equation (1.6) shows that it is favorable to realize long interferometer times T in order to increase the sensitivity of a setup.

1.2.3. The Gravimetric Atom Interferometer (GAIN)

The GAIN experiment is an atom interferometer which has been designed to allow for high-precision gravity measurements at different locations. This field of application implicates much stronger and partly new requirements in comparison to experiments in optical laboratories. Many parts, especially for the laser setup, have been redesigned in order to drastically shrink them in size and achieve a transportable sensor. Transportable in this context means that it can be transported by a small truck and moved around on wheels to the location of interest. Other design criteria have been a fast recommissioning after transportation and a reliable drift-free operation. At the same time the sensor has to maintain or increase the sensitivity of previous laboratory experiments and has to compete with state-of-the-art gravimeters which are based on various other measurement principles. With respect to applications of gravimeters, see Sec. 1.3.4, the GAIN sensor should be able to demonstrate that a single instrument based on this technique can fulfill most or even all of their requirements. For the future, it is aimed at reaching an accuracy of the absolute gravity value of 5×10^{-10} g.

1.3. Classical gravimeters

Today, there are mainly three different types of classical gravimeters in use, which are state-of-the-art and well established. They will be referred to as classical gravimeters to distinguish their working principles from the one of the atom interferometer. While two types of them, mechanical spring type gravimeters and superconducting gravimeters, allow for relative observations, laser interferometer absolute gravimeters give an absolute value of the measured gravity. Since all of them have their individual advantages, we performed comparisons with our atom interferometer together with all three types. The different working principles are shortly introduced in the following.

1.3.1. Mechanical spring type gravimeters

Mechanical spring type gravimeters are based on a test mass m which is attached to a spring of initial length l_0 [9]. Variations in gravity and their resulting changes of the gravitational force

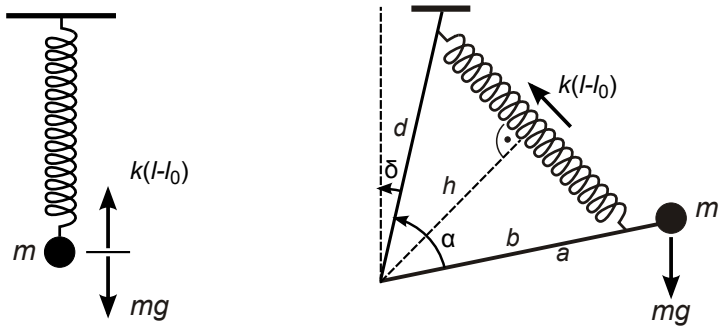

Figure 1.4.: Principles of mechanical spring type gravimeters: vertical spring balance (left) and lever spring balance (right), from [11].

acting on the mass then cause different elongations of the spring due to Hooke's law

$$mg = k(l - l_0) \tag{1.7}$$

where k denotes the spring constant and l the length under load. As a result, changes in gravity are proportional to changes in elongation of the spring. With a modification of the vertical spring balance to a lever spring balance, see Fig. 1.4, the instrumental sensitivity can further be increased. The mass is held by a hinged cantilever and torques due to the spring force and the gravitational force are balanced:

$$mga\sin(\alpha + \delta) = kbd\frac{l - l_0}{l}\sin\alpha \tag{1.8}$$

For a zero-length spring ($l_0 = 0$) and $\alpha + \delta = 90°$ Eq. (1.8) simplifies to

$$mga = kbd\sin\alpha \tag{1.9}$$

and the sensitivity of the balance gets maximal for $\alpha = 90°$ ("astatisation"). Todays gravimeters based on this principle and equipped with position read-out systems with sub micron resolution reach precisions of $100\,\mathrm{nm/s^2}$ and better. Their dynamic range is increased by electronic feedback systems which hold the mass in optimum position.

Accuracy of mechanical spring type gravimeters is limited by alterations of the spring constant and also of the length of the spring which are due to environmental and aging effects. These are minimized by using special housings which are pressure-tight and stabilized in temperature. Still, drifts in the order of $100\,\mathrm{nm/s^2/day}$ to $1000\,\mathrm{nm/s^2/day}$ cannot be avoided. Common instruments are the Scintrex CG-3 and CG-5 vertical spring gravimeters and the gPhone spring lever gravimeter [12, 14].

1.3.2. Superconducting gravimeters

In a superconducting gravimeter (SG) the mechanical spring is replaced by magnetic fields which levitate a spherical test mass. Operated at helium temperature its superconductive coils

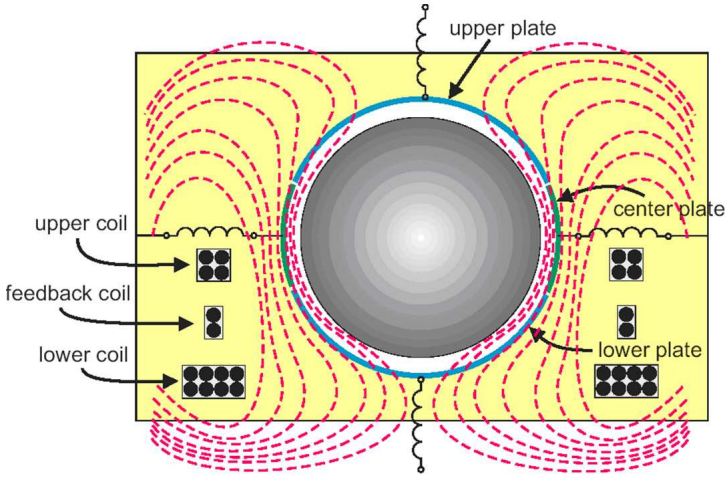

Figure 1.5.: Principle of superconductive gravimeters: the section view shows coils and sphere with magnetic flux lines, from [13].

permanently keep an initial current which is set to compensate the gravitational force. This principle allows the instrument to achieve very low and almost linear drift rates [13, 47, 48].

The spherical test mass is vertically aligned within two niobium wire coils inside a vacuum can. A section view is shown in Fig. 1.5. The coils generate a magnetic field which induces additional currents on the surface of the sphere. Initial as well as induced currents are perfectly stable in time since no ohmic losses occur in the coils and the sphere which are made out of superconductive niobium. Currents are initialized such that the sphere levitates just above the upper coil. The current ratio between upper and lower coil is fine tuned in order to create a low field gradient. Consequently, already weak changes of the gravitational force cause large displacements of the sphere analogue to a small spring constant in the case of a mechanical spring balance.

The displacement is precisely read out by a capacitance bridge surrounding the sphere. In order to increase the dynamical range and to keep the sphere in its optimal position with optimal sensitivity, an additional current is fed back to a third coil which is used to balance temporal changes of the gravitational force.

SG can realize drift rates below $0.15\,\mathrm{nm/s^2/day}$ when operated stationary over several years. Noise levels of only a few $\mathrm{nm/s^2/\sqrt{Hz}}$ can be reached. For correct conversion from the necessary feedback voltage to relative gravity changes, the scaling factor of the individual instrument has to be determined experimentally. One common method is the comparison of data obtained from the SG and an absolute gravimeter (AG) during parallel registration. Most SGs are installed at fixed locations and permanently operated over several years such that their full performance is achieved.

1.3.3. Laser interferometer absolute gravimeters

Today, the absolute gravity value is commonly determined with the help of free fall gravimeters like the FG5 from Micro-g LaCoste and its successor FG5-X [49, 50]. The instruments include a

test mass inside a vacuum chamber, whose position is tracked during a free fall distance of 20 cm (FG5) up to 30 cm (FG5-X) by a laser interferometer in Mach-Zehnder configuration. Laser light from an iodine stabilized helium-neon laser is guided by an optical fiber to the vacuum chamber where it is split up. One beam, which is vertical oriented, is first retro-reflected by the test mass and afterwards by an inertial reference. Finally, it is recombined with the other beam and the resulting interference pattern is recorded by a photo-detector.

The change in path difference of the two interferometer arms is mainly influenced by the changing distance between the test mass and the inertial reference. Analysis of the time evolution of the fringe pattern reveals the acceleration of the test mass. The inertial reference is situated inside a "super spring", which is a seismic isolation and decouples the reference from floor vibrations [51].

The test mass is placed inside a lift, which co-propagates at the same increasing velocity without any contact between them during free fall. It therefore does not disturb the free fall but instead reduces influences of residual rest gas still present in the vacuum chamber. After each drop the lift automatically elevates the test mass to its initial position.

During typical operation 50 or 100 drops are recorded within an hour and added together into one set. The scheme is repeated for 8 to 12 hours when man-made microseism is low and the average value of 2 or 3 nights give the final gravity value [11]. At comparison campaigns like the European Comparison of Absolute Gravimeters (ECAG) accuracies of about 20 $\mathrm{nm/s^2}$ have been reached [52].

1.3.4. Applications

Gravity observations are an important tool in the field of geodesy, geophysics, and metrology. In geodesy the shape of the Earth is studied which is strongly influenced by gravity. The so-called geoid, which represents an equipotential surface in the gravity field and coincides with the mean sea level, is used here as a height datum. In particular it is used for elevation determination in cartography and navigation. Furthermore, its exact morphology is important for studies of oceanic currents, changes of the mean sea level, and in the field of hydrology. In geophysics especially anomalies of the gravity field are investigated. They reveal information on mass distribution and mass transportation within the Earth and thus on the geological structure and on geodynamics. Certain structures, e.g., are typically connected with oil and gas occurrence. Geodynamics include processes like plate tectonics, volcanism and mountain building. Another observable effect is the land uplift due to post-glacial rebound. In metrology the local gravity value is required, e.g., for force and pressure measurements which are used for the calibration of pressure gauges or the redefinition of the Kilogram standard (watt balance).

The accuracy requirements vary for the different applications and in general it has to be distinguished between relative and absolute accuracy and the temporal resolution (sensitivity). The requirements can reach the order of 10^{-8} g to 10^{-10} g in relative accuracy, e.g., for the observation of geodynamical processes, and of 10^{-9} g in absolute accuracy, e.g., for applications in metrology. Because there is no single instrument up to now meeting all of them, each of the different types introduced before has its own fields of application. A more detailed and extensive description on applications and operation of the different classical gravimeters can be found, e.g., in [8, 9, 53].

1.4. Organization of this thesis

The topic and aim of this research was to prepare the Gravimetric Atom Interferometer (GAIN) for mobile measurements and to utilize this feature for comparison campaigns at other locations. By this means, its performance could be investigated and compared to different state-of-the-art gravimeters which are based on other working principles. A second objective was the improvement of the stability of the experiment in order to prevent variations and drifts which had been observed during former measurements. This is also a major precondition for the determination of the absolute gravity value in the future.

In Chapter 2 the theory of atom interferometry is presented. It provides the relation between the acceleration of the atoms and the phase measured in the experiment. In addition, it gives insight into some of the limitations of the performance and into possible sources for drifts and systematic offsets.

The experimental realization of the GAIN sensor is described in Chapter 3. Important modifications which have been developed within this thesis for mobile and reliable operation are motivated and discussed. They include the development of a new laser sub-system and further modifications necessary to achieve the required performance.

Thereafter, the measurement procedure, its several experimental phases, and the data processing are described in Chapter 4. The course of action shows how the gravity acceleration is determined. It remains the same for the parts that follow.

In Chapter 5 major systematic effects, which have been responsible for systematic offsets and temporal drifts of the gravity signal, are discussed. Well-known and also new implementations for their stabilization and suppression are introduced. Amongst others, an improved tilt stabilization is presented and the influence of the used detection on the gravimeter phase is analyzed.

The potential of the GAIN sensor is investigated in Chapter 6. During three comparison campaigns, each performed together with one type of the classical gravimeters, its sensitivity and long-term stability is analyzed and directly compared. Furthermore, the obtained mobility is demonstrated and improvements achieved on this field become visible.

Finally, a conclusion and an outlook is given in Chapter 7.

2. Theoretical background

The atom interferometer used in this work is based on a sequence of Raman light pulses acting on a cloud of laser-cooled Rubidium atoms in free fall. Three Raman light pulses split the wave function of each atom onto two paths, reflect and recombine them and thus form a Mach-Zehnder type interferometer. The outputs of the interferometer are sensitive to phase differences between these paths which also include a contribution from accelerations acting on the atoms during the interferometer sequence.

In this chapter, first, the interaction between a simplified three-level atom and a single Raman light pulse is described. In Sec. 2.2 the result is extended to a $\pi/2 - \pi - \pi/2$ interferometer sequence which becomes sensitive to accelerations. The important equations for the calculation of the gravity value from the measured phase are derived. Afterwards, the impact of laser phase noise, vibrations and a gravity gradient is discussed. The effect of additional energy levels of the ^{87}Rb atom and their AC-Stark shift, which can cause offsets and drifts, is included in Sec. 2.3.

2.1. Stimulated Raman transition

The energy difference ω_{eg} between two hyperfine ground states $|g\rangle$ and $|e\rangle$ of an atom typically corresponds to frequencies of several gigahertz (e.g., 6.8 GHz for ^{87}Rb). Besides a coupling of these states via microwave frequencies, it is also possible to drive the atomic transition in a two-photon, stimulated Raman process with optical frequencies ω_1 and ω_2 and corresponding wave vectors $\boldsymbol{k}_1$ and $\boldsymbol{k}_2$ [46]. The light waves are detuned by a frequency Δ to the transition frequencies to an intermediate level $|i\rangle$ and have a frequency difference close to the hyperfine splitting ω_{eg}, see Fig. 2.1, left. An initial velocity of the atom $\boldsymbol{v}$ induces a Doppler shift $\Delta\omega_D$ that is proportional to the effective wave vector $\boldsymbol{k}_{\mathrm{eff}} = \boldsymbol{k}_1 - \boldsymbol{k}_2$ and to $\boldsymbol{v}$.

$$\Delta\omega_D = \boldsymbol{k}_{\mathrm{eff}} \cdot \boldsymbol{v} \tag{2.1}$$

For counter propagating light beams, it is several orders of magnitude larger than the Doppler shift for a microwave field. Thus, the Raman process is more favorable for a precise measurement of the velocity or, in a sequence of multiple pulses, of the velocity change (acceleration) of an atom. In the latter case the sensitivity can be increased using phase contributions from the Raman pulses which occur during the atom light interaction in an interferometer scheme.

The theory presented here follows the ideas made in [54] and [55].

Atom light interaction

During the absorption or emission of photons the inner state and the external momentum of the atom is changed simultaneously, see Fig. 2.1, right. It is useful to extend each inner energy state

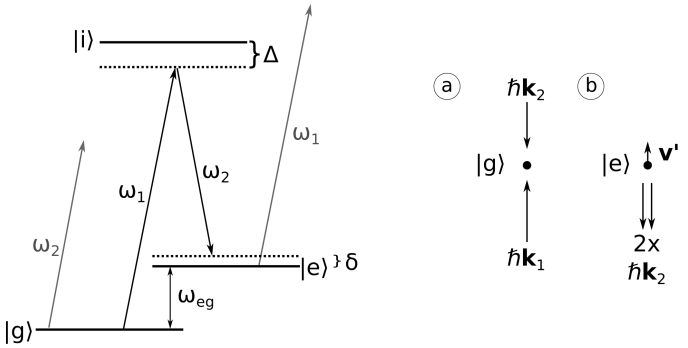

Figure 2.1.: Left: Three-level atom: two optical waves couple the hyperfine levels $|g\rangle$ and $|e\rangle$ via an intermediate level $|i\rangle$. The lasers are detuned by a frequency Δ from the intermediate level and their difference by δ from ω_{eg}. Right: (a) the atom gets additional momentum from the absorption and stimulated emission resulting in a changed velocity $\boldsymbol{v}'$ after the Raman transition (b).

with the corresponding external momentum. The resulting atomic states can now be described by the tensor product of the two Hilbert spaces

$$\begin{aligned} |g, \boldsymbol{p}_g\rangle &= |g\rangle \otimes |p_g\rangle \\ |e, \boldsymbol{p}_e\rangle &= |e\rangle \otimes |p_e\rangle \\ |i, \boldsymbol{p}_{ij}\rangle &= |i\rangle \otimes |p_{ij}\rangle. \end{aligned} \tag{2.2}$$

Starting with one initial inner state and momentum, e.g., $|g, \boldsymbol{p}_g\rangle$, the two ground states have a constant momentum relation and their momenta differ by $\hbar \boldsymbol{k}_{\mathrm{eff}}$. In contrast, the intermediate state can take three different momenta resulting from the combinations of two frequencies and two ground states (two out of four combinations have the same result). This is indicated by the additional index j. All five possibilities form a closed-momentum family and the quantum state of a single atom can be described by the following wave function

$$|\Psi(t)\rangle = a_g(t)|g, \boldsymbol{p}_g\rangle + a_e(t)|e, \boldsymbol{p}_e\rangle + a_{i1}(t)|i, \boldsymbol{p}_{i1}\rangle + a_{i2}(t)|i, \boldsymbol{p}_{i2}\rangle + a_{i3}(t)|i, \boldsymbol{p}_{i3}\rangle \tag{2.3}$$

with time-dependent coefficients $a_n(t)$ and the momenta

$$\boldsymbol{p}_g = \boldsymbol{p}, \quad \boldsymbol{p}_e = \boldsymbol{p} + \hbar \boldsymbol{k}_{\mathrm{eff}}, \quad \boldsymbol{p}_{i1} = \boldsymbol{p} + \hbar \boldsymbol{k}_1, \quad \boldsymbol{p}_{i2} = \boldsymbol{p} + \hbar \boldsymbol{k}_2, \quad \boldsymbol{p}_{i3} = \boldsymbol{p} + \hbar(\boldsymbol{k}_{\mathrm{eff}} + \boldsymbol{k}_1). \tag{2.4}$$

During a Raman pulse the atom interacts with two counter-propagating electromagnetic fields with optical frequencies ω_1 and ω_2 forming a total field

$$\boldsymbol{E} = \boldsymbol{E}_1 \cos(\boldsymbol{k}_1 \cdot \boldsymbol{x} - \omega_1 t + \phi_1) + \boldsymbol{E}_2 \cos(\boldsymbol{k}_2 \cdot \boldsymbol{x} - \omega_2 t + \phi_2). \tag{2.5}$$

The time evolution of the quantum state, given by the Schrödinger equation, can now be described in the light field by using the electric dipole approximation. The Hamiltonian of the system becomes

$$\hat{H} = \frac{\hat{\boldsymbol{p}}^2}{2m} + \hbar\omega_g |g\rangle\langle g| + \hbar\omega_e |e\rangle\langle e| + \hbar\omega_i |i\rangle\langle i| - \hat{\boldsymbol{d}} \cdot \boldsymbol{E} \tag{2.6}$$

with the mass of the atom m, the momentum operator $\hat{\boldsymbol{p}}$ acting on the momentum state and the electric dipole momentum operator $\hat{\boldsymbol{d}}$. Here, spontaneous emission of the intermediate state is neglected since a large detuning Δ relative to the linewidth of this energy state is assumed. Applying the Hamiltonian to the wave function in Eq. (2.3) gives

$$\begin{aligned}\hat{H}|\Psi(t)\rangle = &\left[\left(\frac{\boldsymbol{p}_g^2}{2m}+\hbar\omega_g\right)a_g - \langle g,p_g|\hat{\boldsymbol{d}}\cdot\boldsymbol{E}\sum_{j=1}^{3}a_{ij}|i,p_{ij}\rangle\right]|g,p_g\rangle \\ &+\left[\left(\frac{\boldsymbol{p}_e^2}{2m}+\hbar\omega_e\right)a_e - \langle e,p_e|\hat{\boldsymbol{d}}\cdot\boldsymbol{E}\sum_{j=1}^{3}a_{ij}|i,p_{ij}\rangle\right]|e,p_e\rangle \\ &+\sum_{j=1}^{3}\left[\left(\frac{\boldsymbol{p}_{ij}^2}{2m}+\hbar\omega_i\right)a_{ij} - \langle i,p_{ij}|\hat{\boldsymbol{d}}\cdot\boldsymbol{E}\Big(a_g|g,p_g\rangle + a_e|e,p_e\rangle\Big)\right]|i,p_{ij}\rangle.\end{aligned} \tag{2.7}$$

Each atomic state has a prefactor (in square brackets) which includes contributions from its external and internal energies and from its coupling strengths to the other states. The coefficients a_k contain fast oscillations at atomic frequencies which can be separated from the slowly varying part by applying a change of variables.

$$a_k(t) = c_k(t)\mathrm{e}^{-\mathrm{i}\left(\omega_k+\frac{|\boldsymbol{p}_k|^2}{2m\hbar}\right)t} \tag{2.8}$$

$$\Rightarrow \mathrm{i}\hbar\dot{c}_k(t) = \left[\mathrm{i}\hbar\dot{a}_k(t) - \left(\frac{\boldsymbol{p}_k^2}{2m}+\hbar\omega_k\right)a_k(t)\right]\mathrm{e}^{\mathrm{i}\left(\omega_k+\frac{|\boldsymbol{p}_k|^2}{2m\hbar}\right)t} \tag{2.9}$$

The Schrödinger equation $\mathrm{i}\hbar\frac{\partial}{\partial t}|\Psi(t)\rangle = \hat{H}|\Psi(t)\rangle$ now gives in terms of the new coefficients

$$\begin{aligned}
\mathrm{i}\hbar\dot{c}_g(t) = &-\langle g,p_g|\hat{\boldsymbol{d}}\cdot\boldsymbol{E}_1\mathrm{e}^{-\mathrm{i}\boldsymbol{k}_1\cdot\boldsymbol{x}}|i,p_{i1}\rangle\frac{c_{i1}}{2}\mathrm{e}^{-\mathrm{i}\left(\omega_i-\omega_g-\omega_1+\frac{|\boldsymbol{p}_{i1}|^2-|\boldsymbol{p}_g|^2}{2m\hbar}\right)t}\mathrm{e}^{-\mathrm{i}\phi_1} \\
&-\langle g,p_g|\hat{\boldsymbol{d}}\cdot\boldsymbol{E}_2\mathrm{e}^{-\mathrm{i}\boldsymbol{k}_2\cdot\boldsymbol{x}}|i,p_{i2}\rangle\frac{c_{i2}}{2}\mathrm{e}^{-\mathrm{i}\left(\omega_i-\omega_g-\omega_2+\frac{|\boldsymbol{p}_{i2}|^2-|\boldsymbol{p}_g|^2}{2m\hbar}\right)t}\mathrm{e}^{-\mathrm{i}\phi_2} \\
\mathrm{i}\hbar\dot{c}_e(t) = &-\langle e,p_e|\hat{\boldsymbol{d}}\cdot\boldsymbol{E}_1\mathrm{e}^{-\mathrm{i}\boldsymbol{k}_1\cdot\boldsymbol{x}}|i,p_{i3}\rangle\frac{c_{i3}}{2}\mathrm{e}^{-\mathrm{i}\left(\omega_i-\omega_e-\omega_1+\frac{|\boldsymbol{p}_{i3}|^2-|\boldsymbol{p}_e|^2}{2m\hbar}\right)t}\mathrm{e}^{-\mathrm{i}\phi_1} \\
&-\langle e,p_e|\hat{\boldsymbol{d}}\cdot\boldsymbol{E}_2\mathrm{e}^{-\mathrm{i}\boldsymbol{k}_2\cdot\boldsymbol{x}}|i,p_{i1}\rangle\frac{c_{i1}}{2}\mathrm{e}^{-\mathrm{i}\left(\omega_i-\omega_e-\omega_2+\frac{|\boldsymbol{p}_{i1}|^2-|\boldsymbol{p}_e|^2}{2m\hbar}\right)t}\mathrm{e}^{-\mathrm{i}\phi_2} \\
\mathrm{i}\hbar\dot{c}_{i1}(t) = &-\langle i,p_{i1}|\hat{\boldsymbol{d}}\cdot\boldsymbol{E}_1\mathrm{e}^{\mathrm{i}\boldsymbol{k}_1\cdot\boldsymbol{x}}|g,p_g\rangle\frac{c_g}{2}\mathrm{e}^{\mathrm{i}\left(\omega_i-\omega_g-\omega_1+\frac{|\boldsymbol{p}_{i1}|^2-|\boldsymbol{p}_g|^2}{2m\hbar}\right)t}\mathrm{e}^{\mathrm{i}\phi_1} \\
&-\langle i,p_{i1}|\hat{\boldsymbol{d}}\cdot\boldsymbol{E}_2\mathrm{e}^{\mathrm{i}\boldsymbol{k}_2\cdot\boldsymbol{x}}|e,p_e\rangle\frac{c_e}{2}\mathrm{e}^{\mathrm{i}\left(\omega_i-\omega_e-\omega_2+\frac{|\boldsymbol{p}_{i1}|^2-|\boldsymbol{p}_e|^2}{2m\hbar}\right)t}\mathrm{e}^{\mathrm{i}\phi_2} \\
\mathrm{i}\hbar\dot{c}_{i2}(t) = &-\langle i,p_{i2}|\hat{\boldsymbol{d}}\cdot\boldsymbol{E}_2\mathrm{e}^{\mathrm{i}\boldsymbol{k}_2\cdot\boldsymbol{x}}|g,p_g\rangle\frac{c_g}{2}\mathrm{e}^{\mathrm{i}\left(\omega_i-\omega_g-\omega_2+\frac{|\boldsymbol{p}_{i2}|^2-|\boldsymbol{p}_g|^2}{2m\hbar}\right)t}\mathrm{e}^{\mathrm{i}\phi_2} \\
\mathrm{i}\hbar\dot{c}_{i3}(t) = &-\langle i,p_{i3}|\hat{\boldsymbol{d}}\cdot\boldsymbol{E}_1\mathrm{e}^{\mathrm{i}\boldsymbol{k}_1\cdot\boldsymbol{x}}|e,p_e\rangle\frac{c_e}{2}\mathrm{e}^{\mathrm{i}\left(\omega_i-\omega_e-\omega_1+\frac{|\boldsymbol{p}_{i3}|^2-|\boldsymbol{p}_e|^2}{2m\hbar}\right)t}\mathrm{e}^{\mathrm{i}\phi_1}
\end{aligned} \tag{2.10}$$

where fast rotating terms at optical frequencies $\omega_i - \omega_g + \omega_1$ have been neglected (rotating wave approximation (RWA)). At this point the fixed relative momenta between the internal states become visible when inserting the closure relation in Eq. (2.10)

$$\mathrm{e}^{-\mathrm{i}\boldsymbol{k}_1\cdot\boldsymbol{x}} = \int d^3\boldsymbol{p}\mathrm{e}^{-\mathrm{i}\boldsymbol{k}_1\cdot\boldsymbol{x}}|\boldsymbol{p}\rangle\langle\boldsymbol{p}| = \int d^3\boldsymbol{p}|\boldsymbol{p}\rangle\langle\boldsymbol{p}+\hbar\boldsymbol{k}_1|. \tag{2.11}$$

The external momentum of the atom absorbing a single photon is changed by the photon recoil $\hbar\boldsymbol{k}_1$ and $\hbar\boldsymbol{k}_2$, respectively, leading to the momenta already listed in Eq. (2.4). Terms with no coupling have already been omitted in Eq. (2.10).

The coupling strength between two states is described by the Rabi frequency Ω_{jk} and the detunings Δ, δ, δ_2 and δ_3 of the lasers which include the Doppler shifts and shifts due to photon recoil.

$$\Omega_{jk} \equiv -\frac{\langle i|\hat{\boldsymbol{d}}\cdot\boldsymbol{E}_k|j\rangle}{\hbar} \tag{2.12}$$

$$\Delta \equiv -\left(\omega_i - \omega_g - \omega_1 + \frac{|\boldsymbol{p}+\hbar\boldsymbol{k}_1|^2 - |\boldsymbol{p}|^2}{2m\hbar}\right) = \omega_1 - \left(\omega_i - \omega_g + \frac{\boldsymbol{p}\cdot\boldsymbol{k}_1}{m} + \frac{\hbar|\boldsymbol{k}_1|^2}{2m}\right) \tag{2.13}$$

$$\delta \equiv \omega_1 - \omega_2 - \omega_{\mathrm{eg}} + \frac{|\boldsymbol{p}|^2 - |\boldsymbol{p}+\hbar\boldsymbol{k}_{\mathrm{eff}}|^2}{2m\hbar} = \omega_1 - \omega_2 - \left(\omega_{\mathrm{eg}} + \frac{\boldsymbol{p}\cdot\boldsymbol{k}_{\mathrm{eff}}}{m} + \frac{\hbar|\boldsymbol{k}_{\mathrm{eff}}|^2}{2m}\right) \tag{2.14}$$

$$\delta_2 \equiv \frac{\hbar\boldsymbol{k}_2\cdot\boldsymbol{k}_{\mathrm{eff}}}{m}, \quad \delta_3 \equiv \frac{\hbar\boldsymbol{k}_1\cdot\boldsymbol{k}_{\mathrm{eff}}}{m} \tag{2.15}$$

Inserting these definitions and the the appropriate closure relations into Eq. (2.10) the following equation system is obtained:

$$\begin{aligned}
\mathrm{i}\dot{c}_g(t) &= \frac{c_{i1}(t)}{2}\Omega^*_{g1}\mathrm{e}^{\mathrm{i}\Delta t}\mathrm{e}^{-\mathrm{i}\phi_1} + \frac{c_{i2}(t)}{2}\Omega^*_{g2}\mathrm{e}^{\mathrm{i}(\Delta-\delta-\omega_{\mathrm{eg}}+\delta_2)t}\mathrm{e}^{-\mathrm{i}\phi_2}\\
\mathrm{i}\dot{c}_e(t) &= \frac{c_{i3}(t)}{2}\Omega^*_{e1}\mathrm{e}^{\mathrm{i}(\Delta+\omega_{\mathrm{eg}}-\delta_3)t}\mathrm{e}^{-\mathrm{i}\phi_1} + \frac{c_{i1}(t)}{2}\Omega^*_{e2}\mathrm{e}^{\mathrm{i}(\Delta-\delta)t}\mathrm{e}^{-\mathrm{i}\phi_2}\\
\mathrm{i}\dot{c}_{i1}(t) &= \frac{c_g(t)}{2}\Omega_{g1}\mathrm{e}^{-\mathrm{i}\Delta t}\mathrm{e}^{\mathrm{i}\phi_1} + \frac{c_e(t)}{2}\Omega_{e2}\mathrm{e}^{-\mathrm{i}(\Delta-\delta)t}\mathrm{e}^{\mathrm{i}\phi_2}\\
\mathrm{i}\dot{c}_{i2}(t) &= \frac{c_g(t)}{2}\Omega_{g2}\mathrm{e}^{-\mathrm{i}(\Delta-\delta-\omega_{\mathrm{eg}}+\delta_2)t}\mathrm{e}^{\mathrm{i}\phi_2}\\
\mathrm{i}\dot{c}_{i3}(t) &= \frac{c_e(t)}{2}\Omega_{e1}\mathrm{e}^{-\mathrm{i}(\Delta+\omega_{\mathrm{eg}}-\delta_3)t}\mathrm{e}^{\mathrm{i}\phi_1}
\end{aligned} \tag{2.16}$$

Adiabatic elimination - effective two-level system

At this point we assume that the Rabi frequencies Ω_{jk} are much smaller than the absolute value of the detuning $|\Delta|$. As a consequence the coefficients $c_g(t)$ and $c_e(t)$ change much more slowly than the explicitly time-dependent terms. Thus, the equation system (2.16) can be simplified to a two-level equation system by adiabatic elimination of the intermediate states. $\dot{c}_{i1}(t)$, $\dot{c}_{i2}(t)$ and $\dot{c}_{i3}(t)$ are integrated while keeping the coefficients $c_g(t)$ and $c_e(t)$ constant. Substituting the results into the remaining equations gives the description of a two-level system in an effective

external field.

$$\begin{aligned}\dot{c}_g(t) &= -\mathrm{i}\left(\frac{|\Omega_{g1}|^2}{4\Delta} + \frac{|\Omega_{g2}|^2}{4(\Delta-\delta-\omega_{\mathrm{eg}}+\delta_2)}\right)c_g(t) - \mathrm{i}\left(\frac{\Omega_{e2}^*\Omega_{g1}}{4(\Delta-\delta)}\mathrm{e}^{\mathrm{i}(\delta t+\phi_2-\phi_1)}\right)c_e(t)\\ \dot{c}_e(t) &= -\mathrm{i}\left(\frac{|\Omega_{e1}|^2}{4(\Delta+\omega_{\mathrm{eg}}-\delta_3)} + \frac{|\Omega_{e2}|^2}{4(\Delta-\delta)}\right)c_e(t) - \mathrm{i}\left(\frac{\Omega_{e2}^*\Omega_{g1}}{4\Delta}\mathrm{e}^{-\mathrm{i}(\delta t+\phi_2-\phi_1)}\right)c_g(t)\end{aligned} \tag{2.17}$$

For typical experimental parameters where $|\Delta| \gg |\delta|, |\delta_2|, |\delta_3|$ Eqs. (2.17) can be approximated by

$$\begin{aligned}\dot{c}_g(t) &= -\mathrm{i}\Omega_g^{\mathrm{AC}}c_g(t) - \mathrm{i}\left(\frac{\Omega_{\mathrm{eff}}}{2}\mathrm{e}^{\mathrm{i}(\delta_{12}t+\phi_{\mathrm{eff}})}\right)c_e(t)\\ \dot{c}_e(t) &= -\mathrm{i}\Omega_e^{\mathrm{AC}}c_e(t) - \mathrm{i}\left(\frac{\Omega_{\mathrm{eff}}}{2}\mathrm{e}^{-\mathrm{i}(\delta_{12}t+\phi_{\mathrm{eff}})}\right)c_g(t)\end{aligned} \tag{2.18}$$

with the following definitions of the effective Rabi frequency, the effective phase between the two light fields and the light shifts of the hyperfine levels

$$\Omega_{\mathrm{eff}} \equiv \frac{\Omega_{e2}^*\Omega_{g1}}{2\Delta} \tag{2.19}$$

$$\phi_{\mathrm{eff}} \equiv \phi_2 - \phi_1 \tag{2.20}$$

$$\Omega_g^{\mathrm{AC}} \equiv \frac{|\Omega_{g1}|^2}{4\Delta} + \frac{|\Omega_{g2}|^2}{4(\Delta-\omega_{\mathrm{eg}})}, \qquad \Omega_e^{\mathrm{AC}} \equiv \frac{|\Omega_{e1}|^2}{4(\Delta+\omega_{\mathrm{eg}})} + \frac{|\Omega_{e2}|^2}{4\Delta}. \tag{2.21}$$

The equation system (2.18) is well-known from nuclear magnetic resonance spectroscopy and has been solved in [56, 57]. Its solution describes the evolution of the coefficients with time in the rotating frame.

$$\begin{aligned}c_g(t_0+\tau) &= \mathrm{e}^{-\mathrm{i}(\Omega^{\mathrm{AC}}-\delta)\tau/2}\\ &\quad\cdot\left[\left(\cos\frac{\Omega_r\tau}{2} + \frac{\mathrm{i}(\delta^{\mathrm{AC}}-\delta)}{\Omega_r}\sin\frac{\Omega_r\tau}{2}\right)c_g(t_0) - \mathrm{i}\frac{\Omega_{\mathrm{eff}}}{\Omega_r}\sin\frac{\Omega_r\tau}{2}\mathrm{e}^{\mathrm{i}(\delta t_0+\phi_{\mathrm{eff}})}c_e(t_0)\right]\\ c_e(t_0+\tau) &= \mathrm{e}^{-\mathrm{i}(\Omega^{\mathrm{AC}}+\delta)\tau/2}\\ &\quad\cdot\left[\left(\cos\frac{\Omega_r\tau}{2} - \frac{\mathrm{i}(\delta^{\mathrm{AC}}-\delta)}{\Omega_r}\sin\frac{\Omega_r\tau}{2}\right)c_e(t_0) - \mathrm{i}\frac{\Omega_{\mathrm{eff}}}{\Omega_r}\sin\frac{\Omega_r\tau}{2}\mathrm{e}^{-\mathrm{i}(\delta t_0+\phi_{\mathrm{eff}})}c_g(t_0)\right]\end{aligned} \tag{2.22}$$

δ^{AC} and Ω^{AC} denote the differential and cumulative AC-Stark shifts

$$\delta^{\mathrm{AC}} \equiv \Omega_e^{\mathrm{AC}} - \Omega_g^{\mathrm{AC}} \tag{2.23}$$

$$\Omega^{\mathrm{AC}} \equiv \Omega_g^{\mathrm{AC}} + \Omega_e^{\mathrm{AC}} \tag{2.24}$$

and Ω_r is the Rabi frequency in the rotating frame

$$\Omega_r \equiv \sqrt{\Omega_{\text{eff}}^2 + (\delta - \delta^{\text{AC}})^2}. \tag{2.25}$$

In the non-rotating frame Eq. (2.22) becomes

$$\begin{aligned} a_g(t_0+\tau) &= \mathrm{e}^{-\mathrm{i}(\Omega^{\text{AC}}-\delta+2\omega_g')\tau/2} \\ &\quad \cdot \left[\left(\cos\frac{\Omega_r\tau}{2} + \frac{\mathrm{i}(\delta^{\text{AC}}-\delta)}{\Omega_r}\sin\frac{\Omega_r\tau}{2}\right) a_g(t_0) - \mathrm{i}\frac{\Omega_{\text{eff}}}{\Omega_r}\sin\frac{\Omega_r\tau}{2}\mathrm{e}^{\mathrm{i}(\omega_{\text{eff}}t_0+\phi_{\text{eff}})} a_e(t_0)\right] \\ a_e(t_0+\tau) &= \mathrm{e}^{-\mathrm{i}(\Omega^{\text{AC}}+\delta+2\omega_e')\tau/2} \\ &\quad \cdot \left[\left(\cos\frac{\Omega_r\tau}{2} - \frac{\mathrm{i}(\delta^{\text{AC}}-\delta)}{\Omega_r}\sin\frac{\Omega_r\tau}{2}\right) a_e(t_0) - \mathrm{i}\frac{\Omega_{\text{eff}}}{\Omega_r}\sin\frac{\Omega_r\tau}{2}\mathrm{e}^{-\mathrm{i}(\omega_{\text{eff}}t_0+\phi_{\text{eff}})} a_g(t_0)\right] \end{aligned} \tag{2.26}$$

with the effective wavelength $\omega_{\text{eff}} = \omega_1 - \omega_2$ and

$$\omega_g' = \omega_g + \frac{|\boldsymbol{p}|^2}{2m\hbar}, \qquad \omega_e' = \omega_e + \frac{|\boldsymbol{p} + \hbar\boldsymbol{k}_{\text{eff}}|^2}{2m\hbar}. \tag{2.27}$$

Raman transitions

Equations (2.22) and (2.26) describe the temporal evolution of the atomic system in the rotating and in the initial (non-rotating) frame, respectively. Starting with an atom initially in state $|g\rangle$, a Raman pulse creates a superposition of the two ground states. In the special case of a resonant Raman pulse ($\delta = 0$) without AC Stark shift and with pulse length τ Eq. (2.22) simplifies to

$$c_e(\tau) = -\mathrm{i}\sin\frac{\Omega_{\text{eff}}\tau}{2}\mathrm{e}^{-\mathrm{i}\phi_{\text{eff}}}. \tag{2.28}$$

Thus, the probability of the atom to change its internal state in the rotating frame as well as in the initial frame is modulated by the product of effective Rabi frequency Ω_{eff} and pulse length τ.

$$|a_e|^2 = |c_e|^2 = \frac{1}{2}\left(1 - \cos\Omega_{\text{eff}}\tau\right) \tag{2.29}$$

By adjusting the product to $\Omega_{\text{eff}}\tau = \pi$ or $\Omega_{\text{eff}}\tau = \pi/2$ either the internal state is inverted (π pulse) or an equiprobable superposition is created ($\pi/2$ pulse). Combining Eqs. (2.19) and (2.12) shows, that the effective Rabi frequency is proportional to the total light intensity for a fixed relative intensity $q = I_2/I_1$ and can be used to tune the transition probability.

$$\Omega_{\text{eff}} \propto \sqrt{I_1 I_2} = \frac{\sqrt{q}}{1+q} I_{1+2} \tag{2.30}$$

Transition	Phase shift
$\|g,\boldsymbol{p}\rangle \rightarrow \|g,\boldsymbol{p}\rangle$	$(-\Omega^{\mathrm{AC}}+\delta-2\omega_g')\tau/2+\theta^0$
$\|g,\boldsymbol{p}\rangle \rightarrow \|e,\boldsymbol{p}+\hbar\boldsymbol{k}_{\mathrm{eff}}\rangle$	$(-\Omega^{\mathrm{AC}}-\delta-2\omega_e')\tau/2-\pi/2-\omega_{\mathrm{eff}}t_0-\phi_{\mathrm{eff}}$
$\|e,\boldsymbol{p}+\hbar\boldsymbol{k}_{\mathrm{eff}}\rangle \rightarrow \|g,\boldsymbol{p}\rangle$	$(-\Omega^{\mathrm{AC}}+\delta-2\omega_g')\tau/2-\pi/2+\omega_{\mathrm{eff}}t_0+\phi_{\mathrm{eff}}$
$\|e,\boldsymbol{p}+\hbar\boldsymbol{k}_{\mathrm{eff}}\rangle \rightarrow \|e,\boldsymbol{p}+\hbar\boldsymbol{k}_{\mathrm{eff}}\rangle$	$(-\Omega^{\mathrm{AC}}-\delta-2\omega_e')\tau/2-\theta^0$

Table 2.1.: Phase shifts induced by Raman pulses of length τ to different combinations of initial and final states.

In the absence of light fields it follows that $\Omega_{\mathrm{eff}}=\Omega^{\mathrm{AC}}=0$ and $\Omega_r=|\delta|$ and Eq. (2.22) reduces to

$$\begin{aligned} c_g(t_0+\tau) &= \mathrm{e}^{\mathrm{i}\delta\tau/2}\left(\cos\frac{|\delta|\tau}{2}-\frac{\mathrm{i}\delta}{|\delta|}\sin\frac{|\delta|\tau}{2}\right)c_g(t_0)=c_g(t_0)\\ c_e(t_0+\tau) &= \mathrm{e}^{-\mathrm{i}\delta\tau/2}\left(\cos\frac{|\delta|\tau}{2}+\frac{\mathrm{i}\delta}{|\delta|}\sin\frac{|\delta|\tau}{2}\right)c_e(t_0)=c_e(t_0) \end{aligned} \tag{2.31}$$

Hence, the coefficients in the rotating frame $c_g(t)$ and $c_e(t)$ stay constant during a free evolution.

When the atom is subjected to a sequence of Raman pulses the additional phase contributions in Eq. (2.26) become important for the final population. The phase shifts for the more general case of a Raman pulse with length τ depend on the initial and final state and are shown in Table 2.1. The term θ^0 denotes the phase of $\cos\frac{\Omega_r\tau}{2}+\frac{\mathrm{i}(\delta^{\mathrm{AC}}-\delta)}{\Omega_r}\sin\frac{\Omega_r\tau}{2}$.

2.2. Atom Interferometer

By combining a $\pi/2$, a π and another $\pi/2$ Raman pulse spaced by the time T, a Mach-Zehnder type interferometer is realized, see Fig. 2.2. The photon recoil transferred during the first pulse causes the hyperfine state $|g\rangle$ to spatially separate from the initial state $|e\rangle$ with time. The second pulse inverts states and velocities and the third pulse closes the interferometer.

The population of the two states at the output ports of the interferometer can be calculated by successively applying Eq. (2.26) to the initial state. Therefore, it is convenient to rewrite the equation system using the matrix formalism

$$\begin{pmatrix} a_g(t_0+\tau)\\ a_e(t_0+\tau)\end{pmatrix} = M(t_0,\tau,\Omega_r,\phi_{\mathrm{eff}})\begin{pmatrix} a_g(t_0)\\ a_e(t_0)\end{pmatrix}. \tag{2.32}$$

For resonant pulses starting at time t_0 and without AC Stark shifts the evolution matrix becomes

$$M(t_0,\tau,\Omega_r,\phi_{\mathrm{eff}}) = \begin{pmatrix} \mathrm{e}^{-\mathrm{i}\omega_g'\tau}\cos\frac{\Omega_r\tau}{2} & -\mathrm{i}\mathrm{e}^{-\mathrm{i}\omega_g'\tau}\mathrm{e}^{\mathrm{i}(\omega_{\mathrm{eff}}t_0+\phi_{\mathrm{eff}})}\sin\frac{\Omega_r\tau}{2}\\ -\mathrm{i}\mathrm{e}^{-\mathrm{i}\omega_e'\tau}\mathrm{e}^{-\mathrm{i}(\omega_{\mathrm{eff}}t_0+\phi_{\mathrm{eff}})}\sin\frac{\Omega_r\tau}{2} & \mathrm{e}^{-\mathrm{i}\omega_e'\tau}\cos\frac{\Omega_r\tau}{2}\end{pmatrix} \tag{2.33}$$

The complete light interaction during the interferometer sequence can now be described using

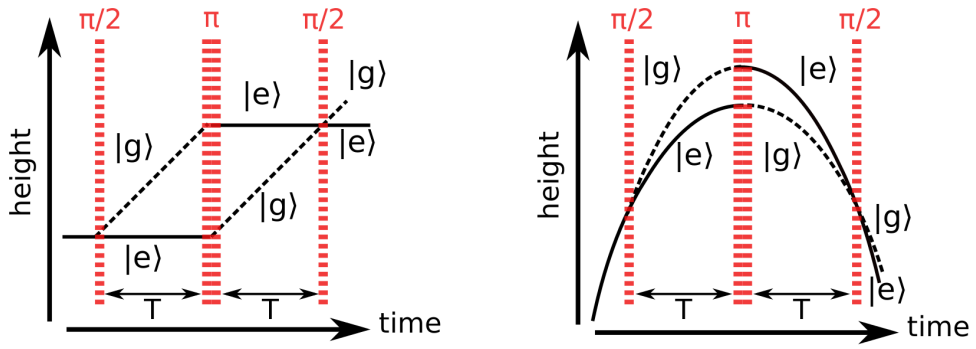

Figure 2.2.: Left: A $\pi/2$-π-$\pi/2$ sequence of Raman pulses splits the atomic wave function onto two different paths, reflects and finally recombines them and thereby forms a Mach-Zehnder type interferometer (left). The two atomic ground states $|g\rangle$ and $|e\rangle$ are indicated as dashed and solid lines. The right figure shows the paths under the influence of gravity and an initial velocity pointing upwards.

matrix multiplication

$$M(2T+3\tau,\tau,\Omega_r,\phi_{\text{eff},3})M(T+3\tau,T,0,0)M(T+\tau,2\tau,\Omega_r,\phi_{\text{eff},2})M(\tau,T,0,0)M(0,\tau,\Omega_r,\phi_{\text{eff},1}) \tag{2.34}$$

which gives the final populations of the two states. The probability of atoms initially prepared in the lower state of being transferred to the upper state is given at the end of the sequence at time $2T+4\tau$ by

$$P = |a_e(2T+4\tau)|^2 = \bar{P} - \frac{C}{2}\cos(\Delta\Phi). \tag{2.35}$$

It depends on the effective laser phases during the Raman pulses

$$\Delta\Phi = \phi_{\text{eff},1} - 2\phi_{\text{eff},2} + \phi_{\text{eff},3}. \tag{2.36}$$

The mean population $\bar{P}$ and the contrast C are equal to one half and unity respectively for perfect $\pi/2$ and π Raman pulses. In the more general case, e.g., when not all atoms obtain the same Rabi frequency due to a inhomogeneous intensity profile, $\bar{P}$ can slightly differ from one half and the contrast of the interferometer C is reduced. In addition, a non-perfect π pulse is again a beam splitter and initiates additional paths for the atoms. These arms, however, do not cause interference because their spatial separation $\Delta x = \hbar k_{\text{eff}} T/m$ is much larger than the spatial coherence length of the atomic ensemble $l_c = \hbar/\Delta p$ at the end of the interferometer sequence [19]. Here, Δp denotes the momentum spread of the ensemble.

The interferometer phase can also be obtained by calculating the difference between the phases accumulated along the different paths using the phase shifts listed in Table 2.1.

$$\Delta\Phi = \phi_{\text{eff},1} - 2\phi_{\text{eff},2} + \phi_{\text{eff},3} - (\theta_1^0 - \theta_3^0) \tag{2.37}$$

The result also includes two additional phase contributions θ_1^0 and θ_3^0 which arise from the difference between the detuning and the differential AC Stark shift $(\delta^{AC} - \delta)$. If θ^0 is different

for the first and third pulse, e.g., due to changing intensities, a remaining phase shift is caused. A cancellation of the effect will be discussed in Sec. 2.3.

2.2.1. Sensitivity function

The phase contributions $\phi_{\mathrm{eff,i}}$ during the light interactions can be determined with the help of the sensitivity function, which was introduced and experimentally verified for an atom interferometer in [58]. It allows to calculate the influence on the transition probability $\delta P(\delta\phi, t)$ for a phase jump $\delta\phi$ of the Raman phase at a time t and is defined by

$$g(t) = 2 \lim_{\delta\phi \to 0} \frac{\delta P(\delta\phi, t)}{\delta\phi}. \tag{2.38}$$

Since the highest sensitivity in phase is achieved for an atom interferometer operated at $\Delta\Phi = \pi/2$, it is useful to apply a series expansion to Eq. (2.35) at this point and insert the result into Eq. (2.38). This gives

$$g(t) = \lim_{\delta\phi \to 0} \frac{\delta\Phi(\delta\phi, t)}{\delta\phi}. \tag{2.39}$$

By analyzing Eq. (2.36) the sensitivity function can be obtained. For an instant phase jump $\delta\phi$ at time t the correspondent matrix in Eq. (2.34) is replaced by a matrix product treating the evolution before and after the phase jump individually

$$M'_{t,\delta\phi}(t_0, \tau, \Omega_r, \phi_0) = M(t, \tau - (t - t_0), \Omega_r, \phi_0 + \delta\phi) M(t_0, (t - t_0), \Omega_r, \phi_0). \tag{2.40}$$

A phase jump $\delta\phi > 0$ between the second and third interferometer pulse, for example, would only effect $\phi_{\mathrm{eff,3}}$ and would increase $\Delta\Phi$, whereas a phase jump between the first and second pulse would result in a decrease. The complete sensitivity function for an atom interferometer becomes [58]

$$g(t) = \begin{cases} \sin(\Omega_R(T + t)) & -T - 2\tau < t < -T - \tau \\ -1 & -T - \tau < t < -\tau \\ \sin(\Omega_R(t)) & -\tau < t < \tau \\ 1 & \tau < t < T + \tau \\ -\sin(\Omega_R(T - t)) & T + \tau < t < T + 2\tau \\ 0 & \text{else.} \end{cases} \tag{2.41}$$

It is visualized in Fig. 2.3. The time origin is chosen to be at the center of the second pulse to emphasize $g(t)$ being an odd function. The interferometer phase can now be calculated by integrating phase variations of the lasers with the weighting function

$$\Delta\Phi = \int_{-\infty}^{+\infty} g(t) \mathrm{d}\phi(t) = \int_{-\infty}^{+\infty} g(t) \frac{\mathrm{d}\phi(t)}{\mathrm{d}t} \mathrm{d}t. \tag{2.42}$$

In the rest frame of a free-falling atom the laser phase changes over time. In order to fulfill the resonance condition for all Raman pulses a linear frequency ramp α is typically applied to

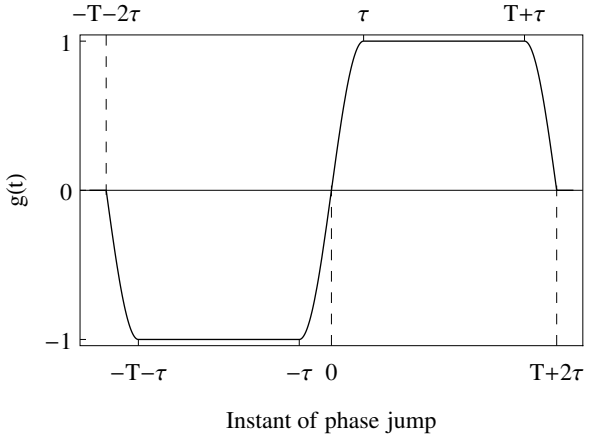

Figure 2.3.: Sensitivity function $g(t)$ for different instants t of the interferometer sequence.

one of the lasers canceling the Doppler shift. The effective laser phase for an atom with initial position $\boldsymbol{z}_0$ and velocity $\boldsymbol{v}_0$ becomes

$$\phi(t) = \boldsymbol{k}_{\text{eff}}(\boldsymbol{z}_0 + \boldsymbol{v}_0 t - \frac{1}{2}\boldsymbol{g}t^2) + \frac{1}{2}\alpha t^2 + \phi_0 \tag{2.43}$$

where $\boldsymbol{g}$ denotes the gravity acceleration. Combining Eqs. (2.42) with (2.43) gives

$$\Delta\Phi = (\boldsymbol{k}_{\text{eff}}\boldsymbol{g} - \alpha)\,(T + 2\tau)\left(T + \frac{4\tau}{\pi}\right) \tag{2.44}$$

which is comparable to [59]. The result is independent of the initial position and velocity because of the symmetry of the interferometer sequence and its odd sensitivity function.

Finally, by inserting Eq. (2.44) into Eq. (2.35) the probability of atoms initially prepared in one state to be transferred to the other state can be written as

$$\boxed{P = \bar{P} - \frac{C}{2}\cos\left((\boldsymbol{k}_{\text{eff}}\boldsymbol{g} - \alpha)\,(T + 2\tau)\left(T + \frac{4\tau}{\pi}\right) + \Delta\phi_L\right)} \tag{2.45}$$

with the mean population $\bar{P}$ and the interferometer contrast C. The additional contribution $\Delta\phi_L$ is inserted here to consider for a phase jump in between the second and third pulse which will be applied to the laser in the experiment.

2.2.2. Phase noise due to laser phase noise

The sensitivity function just presented can also be used to analyze the impact from phase noise introduced into the system. The two most important noise sources are remaining phase noise from the Raman phase lock including noise from its frequency reference and phase noise introduced into the Raman laser light by vibrations of the retro-reflecting mirror.

The transfer function of the system $H(\omega)$ gives the interferometer phase response to a sinu-

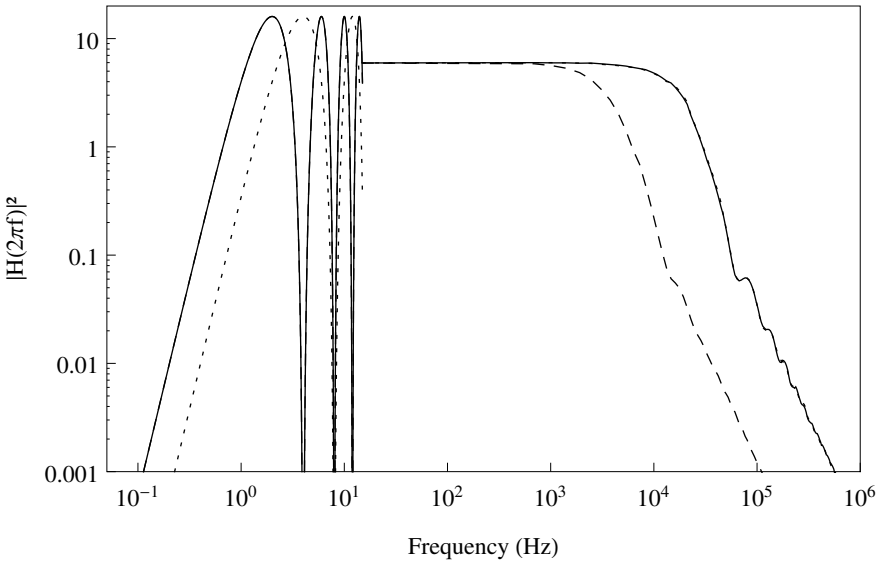

Figure 2.4.: Weighting function $|H(\omega)|^2$ calculated for T=250 ms and τ=20 µs (solid line), typical parameters of the GAIN experiment. The function is averaged for frequencies above 25 Hz. A shorter pulse separation changes the sensitivity at low frequencies but leaves the average unchanged at high frequencies (dotted line: T=125 ms). In contrast, the pulse length mainly determines the cutoff frequency of the low-pass behavior (dashed line: τ=100 µs).

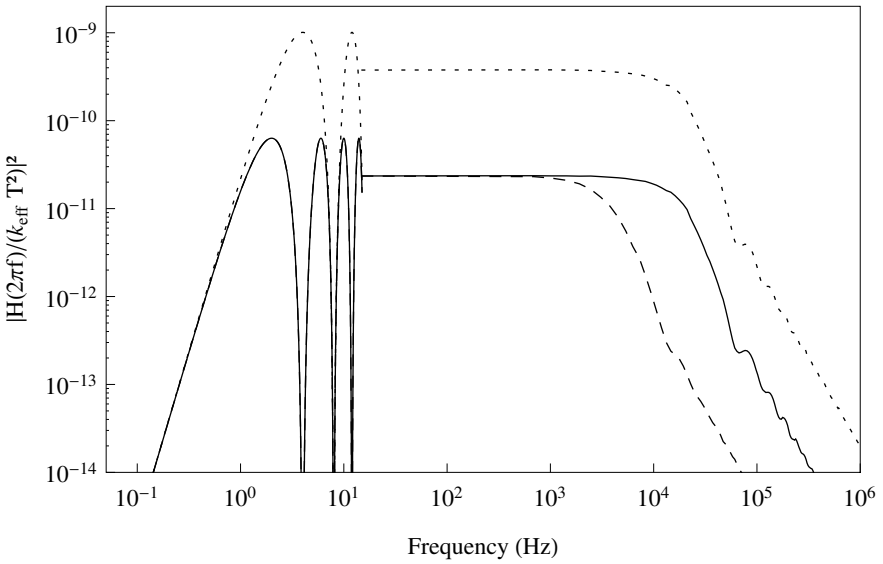

Figure 2.5.: Normalized weighting function for an acceleration sensor $|H(\omega)/(k_{\text{eff}}T^2)|^2$ calculated for T=250 ms and τ=20 µs (solid line). The sensitivity at low frequencies is unaffected by changed pulse separation times but at all other frequencies the average increases for shorter times (dotted line: T=125 ms). The influence of the pulse length remains. It determines the cutoff frequency of the low-pass behavior (dashed line: τ=100 µs). The functions are averaged for frequencies above 25 Hz.

soidal oscillation of the form $\phi(t) = A_0 \cos(\omega_0 t + \psi)$ of the Raman phase and is related to the Fourier transform of the sensitivity function [58]

$$H(\omega) = \omega G(\omega) \tag{2.46}$$

with

$$G(\omega) = \int_{-\infty}^{+\infty} \mathrm{e}^{-\mathrm{i}\omega t} g(t) \mathrm{d}t. \tag{2.47}$$

The transfer function for an interferometer with the sensitivity function from Eq. (2.41) becomes

$$H(\omega) = \frac{4\mathrm{i}\omega\Omega_R}{\omega^2 - \Omega_R^2} \sin\left(\frac{\omega(T+2\tau)}{2}\right) \times \left(\cos\left(\frac{\omega(T+2\tau)}{2}\right) + \frac{\Omega_R}{\omega} \sin\left(\frac{\omega T}{2}\right)\right) \tag{2.48}$$

and can be approximated at frequencies much lower than the Rabi frequency ($\omega \ll \Omega_r$) by

$$H(\omega) = -4\mathrm{i} \sin^2\left(\frac{\omega T}{2}\right) \tag{2.49}$$

Figure 2.4 shows the weighting function $|H(\omega)|^2$ evaluated for different pulse separation times T and pulse lengths τ. The fast oscillations are averaged above 25 Hz. The function shows characteristics of a band pass filter combined with an oscillating part causing a series of zeros. The cutoff frequency of the low-pass behavior at high frequencies is determined by the Rabi frequency and in consequence by the inverse pulse length ($f_c \propto \Omega_r \propto 1/\tau$). Longer Raman pulses narrow down the influence of phase noise at high frequencies. The sensitivity at low frequencies and the positions of the zeros are influenced by the pulse separation times. The former increases with growing pulse separation.

Inserting the perturbation $\phi(t)$ into the weighting function (Eq. (2.42)) and assuming a random distribution of the modulation phase ψ of different measurements gives the rms value of the interferometer phase

$$\delta\Phi^{\mathrm{rms}} = |A_0 H(\omega_0)| \tag{2.50}$$

and the rms standard deviation for uncorrelated Raman phase noise

$$(\sigma_\Phi^{\mathrm{rms}})^2 = \int_0^{+\infty} |H(\omega)|^2 S_\phi(\omega) \mathrm{d}\omega. \tag{2.51}$$

$S_\phi(\omega)$ denotes the power spectral density (PSD) of the Raman phase noise.

The influence of phase noise on the measured acceleration g shows a slightly different behavior. According to Eq. (2.44) the phase and consequently the transfer function have to be divided by approximately $k_{\mathrm{eff}} T^2$ to obtain the acceleration. As a result a longer pulse separation time does not increase the influence of phase noise at very low frequencies but lowers its weight on average at all other frequencies including high frequencies, see Fig. 2.5. Zeros are again shifted. The influence of a changed pulse length stays the same.

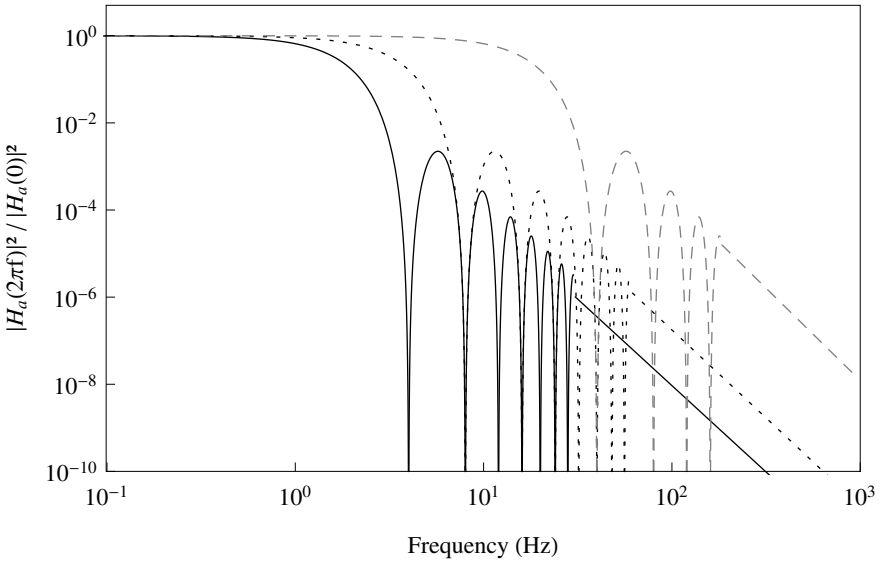

Figure 2.6.: Relative weighting function for mirror vibrations $|H_a(\omega)|^2/|H_a(0)|^2$ calculated for T=250 ms (solid line), 125 ms (dotted line) and 25 ms (dashed line) with τ=20 µs. The function is averaged at higher frequencies.

2.2.3. Phase noise due to mirror vibrations

In order to minimize phase noise between the two Raman beams they are often guided as long as possible together to the atoms. This can be achieved with both beams entering the vacuum chamber from, e.g., the top of the chamber. A mirror at the lower end retro-reflects both beams and a combination of one beam pointing downwards and the other pointing upwards drives the Raman transition. The favored beam pair can be selected by tuning the frequency difference to resonance considering the present Doppler shift. Consequently, another contribution to phase noise is introduced by the retro-reflecting mirror since it is only included in the beam path of one of the Raman beams. Vibrations of the mirror cause path length changes δz and effect the effective Raman phase by $\delta\phi \approx k_{\text{eff}}\delta z$. The rms standard deviation for uncorrelated phase noise caused by vibrations becomes [60]

$$(\sigma_\Phi^{\text{rms}})^2 = \int_0^{+\infty} |H_a(\omega)|^2 S_a(\omega) \mathrm{d}\omega. \tag{2.52}$$

$S_a(\omega)$ is the PSD of the acceleration noise and $H_a(\omega)$ the acceleration noise transfer function given by

$$|H_a(\omega)|^2 = \frac{k_{\text{eff}}^2}{\omega^4} |H(\omega)|^2. \tag{2.53}$$

The square of this function normalized to the limit of a constant acceleration is shown in Fig. 2.6 for three different pulse separation times. Vibrational noise of the mirror at frequencies above several Hertz is more and more suppressed relative to slow changes of the acceleration for increasing pulse separations. Variations of the pulse length cause no significant changes.

2.2.4. Gravity gradient

The formalism for the calculation of the interferometer phase shift used up to here presumes the conservation of momentum states in between the light pulses. This holds in the absence of accelerations and also in the free falling rest frame of the atoms under constant gravity. In the presence of gravity gradients, however, conservation is not guaranteed any more and an exact solution as it is presented in [61] strongly increases complexity. In an alternative approach the two cases are calculated separately using the path integral description and the single results are summed up in the end [59, 62].

The total interferometer phase then becomes the sum of three different contributions arising from the light interactions $\Delta\Phi_{\text{light}}$ which we already considered, from the propagation on the two paths $\Delta\Phi_{\text{path}}$ and from different initial positions of the interfering wave packets $\Delta\Phi_{\text{split}}$

$$\Delta\Phi = \Delta\Phi_{\text{light}} + \Delta\Phi_{\text{path}} + \Delta\Phi_{\text{split}}. \tag{2.54}$$

The last term is very small under the experimental conditions used here and can therefore be neglected [59].

The phase contribution of the free evolution can be calculated from the different classical actions along the two paths

$$\Delta\Phi_{\text{path}} = \frac{\Delta S_{\text{Cl}}}{\hbar} = \frac{1}{\hbar}\oint L(z,\dot{z}) \tag{2.55}$$

where the Lagrangian for a gravitational field with a linear gradient γ is

$$L(z,\dot{z}) = \frac{m}{2}\dot{z}^2 - mg_0 z + \frac{m}{2}\gamma z^2. \tag{2.56}$$

m is the mass of the falling object. The solution of the Euler-Lagrange equation gives the trajectory of the object for an initial position z_0 and initial velocity v_0.

$$\begin{aligned} z(t) &= \frac{g_0}{\gamma} + \left(z_0 - \frac{g_0}{\gamma}\right)\cosh(t\sqrt{\gamma}) + \frac{v_0}{\sqrt{\gamma}}\sinh(t\sqrt{\gamma}) \\ &\approx z_o + v_0 t - \frac{1}{2}g_0 t^2 + \gamma t^2\left(\frac{1}{2}z_0 + \frac{1}{6}v_0 t - \frac{1}{24}g_0 t^2\right) \end{aligned} \tag{2.57}$$

The first three terms of Eq. (2.57) have already been considered in Eq. (2.43) when analyzing the influence of a constant gravitational field. The fourth summand which includes γ can now be used for a correction of the measured gravity value g in Eq. (2.45). For a final Raman pulse at height z_0 and the gravity value on the floor g_0 this gives

$$\boxed{g \approx \frac{\Delta\Phi_{\text{path}}}{k_{\text{eff}}T^2} \approx g_0 + \gamma\left(\frac{7}{12}g_0 T^2 - \overline{v}_0 T - z_0\right)} \tag{2.58}$$

where $\overline{v}_0 = v_0 + \frac{1}{2}v_{\text{rec}}$ is the average velocity of the two paths just before the last pulse. Second and higher order terms of the gradient are well below the targeted accuracy of 5×10^{-10} g and can be omitted. A detailed analysis of their contribution can be found in [63].

2.3. Interferometry with Rubidium 87

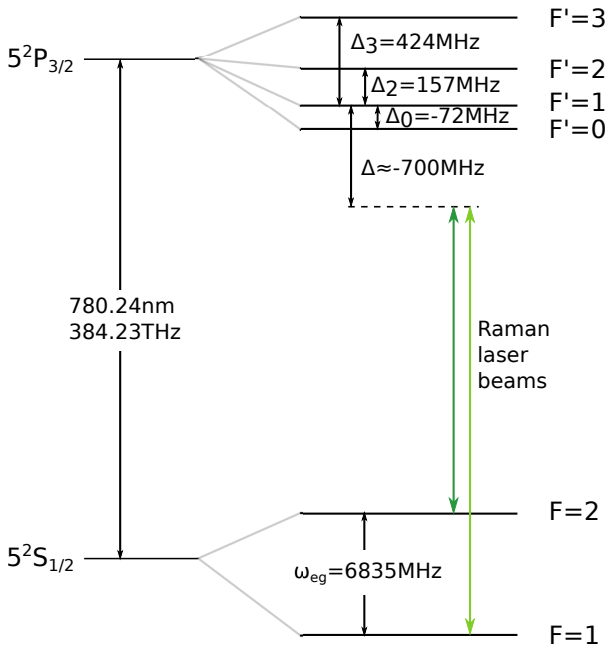

Figure 2.7.: Hyperfine structure of the D_2 transition in ^{87}Rb and Raman laser frequencies. Energy differences are not in scale. Values adopted from [64].

In the previous parts the interaction between the Raman pulses and a three-level atom has been used to calculate the phase of the atom interferometer sequence and its relation to the gravity acceleration. The GAIN experiment operates with ^{87}Rb atoms and uses Raman laser frequencies which are red detuned relative to the D_2 transition, see Fig. 2.7. They drive the transition between the two hyperfine states $|5^2S_{1/2}, F = 1\rangle$ and $|5^2S_{1/2}, F = 2\rangle$. The $|5^2P_{3/2}\rangle$ state splits into for hyperfine states due to the hyperfine splitting. Whereas all four contribute to the AC Stark light shifts, only the states $|5^2P_{3/2}, F' = 1\rangle$ and $|5^2P_{3/2}, F' = 2\rangle$ are involved in the Raman transitions because of the selection rules. Including the additional levels into the atom light interaction causes only a few changes. The four intermediate levels are removed during the adiabatic elimination in the same way a single intermediate level has been removed previously resulting again in an effective two-level transition. Only the definitions of the effective Rabi frequency and the occurring AC light shifts from Eqs. (2.19) and (2.21) have to be adapted. They become

$$\Omega_{\text{eff}} = \sum_m \frac{\Omega^*_{m,e2}\Omega_{m,g1}}{2(\Delta - \Delta_m)} \tag{2.59}$$

$$\Omega_g^{\text{AC}} = \sum_m \frac{|\Omega_{m,g1}|^2}{4(\Delta - \Delta_m)} + \frac{|\Omega_{m,g2}|^2}{4(\Delta - \omega_{\text{eg}} - \Delta_m)}, \qquad \Omega_e^{\text{AC}} = \sum_m \frac{|\Omega_{m,e1}|^2}{4(\Delta + \omega_{\text{eg}} - \Delta_m)} + \frac{|\Omega_{m,e2}|^2}{4(\Delta - \Delta_m)} \tag{2.60}$$

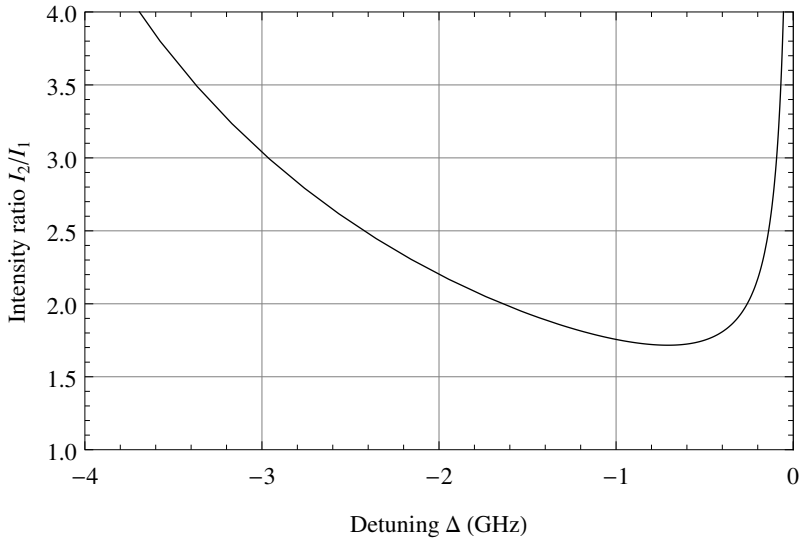

Figure 2.8.: Required intensity ratio between the two Raman laser beams for the cancellation of the differential AC Stark shift depending on the Raman detuning Δ.

where Δ_m and $\Omega_{m,jk}$ denote the detunings and Rabi frequencies for the single energy levels $|F' = 0\rangle$ to $|F' = 3\rangle$ with

$$\Omega_{m,jk} \equiv -\frac{\langle F' = m|\hat{\boldsymbol{d}} \cdot \boldsymbol{E}_k|j\rangle}{\hbar}. \tag{2.61}$$

AC Stark shift

The total light shift Ω^{AC} is the same for both paths during each of the pulses, compare Table 2.1, assuming a constant light intensity over the splitting of the paths. Its effect therefore cancels in the interferometer phase in Eq. (2.37). In contrast, the differential phase shift δ^{AC} is still included via the terms θ_1^0 and θ_3^0. Atoms with remaining horizontal velocities move within the Gaussian intensity profile causing different light intensities at the position of the atoms for the first and last pulse. As a consequence the two terms in general do not cancel completely. In order to avoid systematic offsets, it is important to cancel the differential AC Stark shift.

The AC Stark shifts for the two hyperfine levels can be calculated with Eq. (2.60) by inserting the corresponding Clebsch-Gordan coefficients from [64] for an orthogonal linear polarization of the Raman beams. This gives

$$\begin{aligned}
\Omega_g^{\mathrm{AC}} &= \frac{|\Omega_1|^2}{4}\left(\frac{5}{24\Delta} + \frac{1}{8(\Delta-\Delta_2)}\right) + \frac{|\Omega_2|^2}{4}\left(\frac{5}{24(\Delta-\omega_{\mathrm{eg}})} + \frac{1}{8(\Delta-\omega_{\mathrm{eg}}-\Delta_2)}\right) \\
\Omega_e^{\mathrm{AC}} &= \frac{|\Omega_1|^2}{4}\left(\frac{1}{120(\Delta+\omega_{\mathrm{eg}})} + \frac{1}{8(\Delta+\omega_{\mathrm{eg}}-\Delta_2)} + \frac{1}{5(\Delta+\omega_{\mathrm{eg}}-\Delta_3)}\right) \\
&\quad + \frac{|\Omega_2|^2}{4}\left(\frac{1}{120\Delta} + \frac{1}{8(\Delta-\Delta_2)} + \frac{1}{5(\Delta-\Delta_3)}\right)
\end{aligned} \tag{2.62}$$

with $\Omega_k = 2\boldsymbol{d} \cdot \boldsymbol{E}_k/\hbar$. The effective Rabi frequency becomes

$$\Omega_{\text{eff}} = \frac{\Omega_1 \Omega_2}{2} \underbrace{\left(\frac{1}{24\Delta} + \frac{1}{8(\Delta - \Delta_2)} \right)}_{\equiv \gamma}. \tag{2.63}$$

The differential AC Stark shift $\delta^{\text{AC}} = \Omega_e^{\text{AC}} - \Omega_g^{\text{AC}}$ can then be canceled by choosing the right intensity ratio between the two laser beams, which becomes a function of the Raman detuning Δ

$$\frac{|E_2|^2}{|E_1|^2} = \frac{I_2}{I_1} = \frac{\left(\frac{1}{120(\Delta+\omega_{\text{eg}})} + \frac{1}{8(\Delta+\omega_{\text{eg}}-\Delta_2)} + \frac{1}{5(\Delta+\omega_{\text{eg}}-\Delta_3)} \right) - \left(\frac{5}{24\Delta} + \frac{1}{8(\Delta-\Delta_2)} \right)}{\left(\frac{5}{24(\Delta-\omega_{\text{eg}})} + \frac{1}{8(\Delta-\omega_{\text{eg}}-\Delta_2)} \right) - \left(\frac{1}{120\Delta} + \frac{1}{8(\Delta-\Delta_2)} + \frac{1}{5(\Delta-\Delta_3)} \right)}. \tag{2.64}$$

The required intensity ratio is shown in Fig. 2.8 as a function of the detuning to the red ($\Delta < 0$) relative to the $|5^2P_{3/2}, F' = 1\rangle$ energy level.

If the differential AC Stark shift is not canceled, it can be calculated from

$$\delta^{\text{AC}} = \frac{|\Omega_1|^2}{4}\alpha - \frac{|\Omega_2|^2}{4}\beta \tag{2.65}$$

where α and β denote the numerator and denominator on the right side of Eq. (2.64). Using Eq. (2.63) and inserting $|\Omega_2|^2 = \frac{I_2}{I_1}|\Omega_1|^2$ this becomes

$$\delta^{\text{AC}} = \frac{|\Omega_1|^2}{4}(\alpha - \frac{I_2}{I_1}\beta) = \frac{1}{2}\frac{(\alpha - \frac{I_2}{I_1}\beta)}{\gamma\sqrt{I_2/I_1}}\Omega_{\text{eff}} \tag{2.66}$$

which is proportional to to effective Rabi frequency. For almost correct intensity ratios $q_0 + \delta q$ the remaining AC-Stark shift δ^{AC} is approximately proportional to the deviation δq

$$\delta^{\text{AC}} \approx \frac{1}{2}\frac{\beta\,\Omega_{\text{eff}}}{\gamma\sqrt{q_0}}\delta q \qquad \text{for} \quad |\delta q| \ll q_0. \tag{2.67}$$

3. Experimental setup

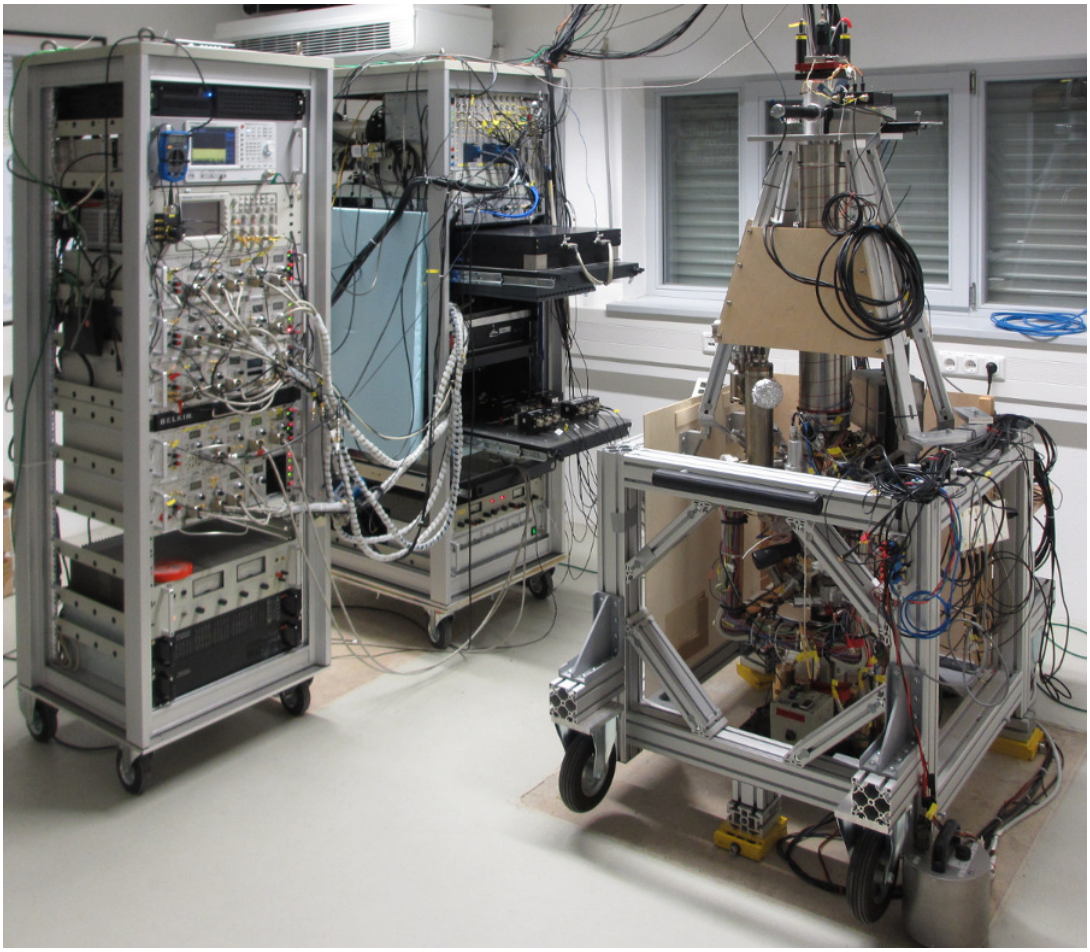

Figure 3.1.: Photograph of the GAIN experiment with its physics package comprising the vacuum chamber (right) and its two racks which include the laser system (middle) and electronics and computers (left).

In this chapter, the experimental setup of the experiment is briefly reviewed. Then, the modifications of the laser system are first described on the basis of the system overview in Sec. 3.2.2 and afterwards in detail. The limitations of the original laser switching system are analyzed. They are used to formulate design criteria with respect to the required high stability and reliability during long-term measurements and to a favored fast and easy recommissioning after transportation. On their basis, a completely new laser sub-system for combining, switching and

distribution of laser light has been developed during this work, see Sec. 3.2.4. It ensures constant beam powers and thus a stable MOT position which otherwise could introduce unsteady trajectories of the atomic cloud. They would introduce (changing) offsets in combination with the gravity gradient and the influence of rotations. In addition, a new feature has been implemented to the Raman sub-system with the same intention. There, an intensity stabilization for two overlapped laser beams has been realized (Sec. 3.2.5) to compensate for long-term drifts of the laser setup and thereby avoid especially (changing) AC Stark shifts during gravity measurements[1]. Furthermore, the implementation of the data storage based on a MySQL database is presented in Sec. 3.3. It allows to store the measured data together with an extensive parameter set and guarantees easy access and searching during the analysis afterwards.

Figure 3.1 shows a photograph of the experimental setup of the mobile GAIN experiment. It was taken during the measurement campaign with the superconducting gravimeter in Wettzell (Southern Germany) in November 2013. The system can be divided into two main parts, the physics package with the vacuum chamber in the foreground on the right hand side and the two 19" racks on the left hand side. They contain the laser system, which is situated in the black boxes on drawers in the right rack, and appropriate electronics to provide all required laser frequencies at the necessary powers for MOT and atom interferometer operation. A control computer with a field programmable gate array (FPGA) ensures the right timing. Both parts were initially designed and set up during the former theses of Alexander Senger [65] and Malte Schmidt [66]. Descriptions can also be found in [67, 68].

3.1. Physics package

3.1.1. Vacuum chamber

All interactions with the rubidium atoms, including initial preparation, the interferometer scheme, and final read-out, take place inside the vacuum chamber which is part of the physics package. The chamber is mainly made of titanium alloy which allows for UHV and has favorable properties such as a low density and a low magnetic permeability which is close to unity. Thus, stray magnetic fields occurring, e.g., after switching of the MOT coils, are kept low. A 20 l/s ion pump and a titanium sublimation pump, the latter is activated approximately every three months, maintain a pressure of 2×10^{-10} mbar. During operation of the interferometer, a dispenser from SAES getters releases rubidium into the MOT zone and the pressure is increased to the 1×10^{-9} mbar range.

The chamber design allows for an atomic fountain with a MOT and a vertical launch of the atoms in its lower part. Hence, the time of free fall is doubled to approximately 0.75 s of which 0.7 s can be used for the interferometer sequence. The vacuum chamber is built into a transportable cage setup, see Fig. 3.1, with overall dimensions of $193 \times 82 \times 127\,\mathrm{cm}^3$ and has a total mass of 160 kg. A section view of the vacuum chamber is shown in Fig. 3.2.

The chamber can be divided into three different parts of which each is dedicated to different phases of the experimental sequence:

[1] The mentioned effects are analyzed in Chapter 5.

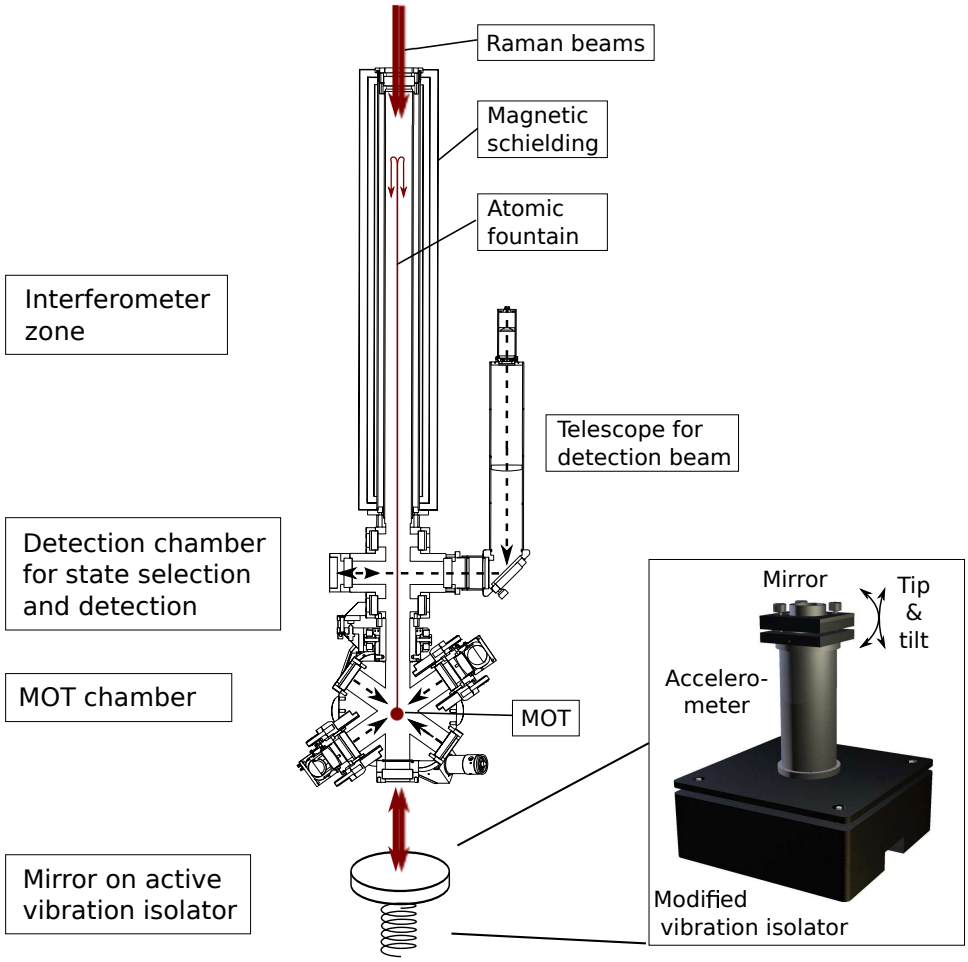

Figure 3.2.: Section view of the vacuum chamber with different zones dedicated for MOT/launch, state selection/detection and interferometry. Raman beams enter from the top and are retro-reflected by a mirror on an active vibration isolator. CAD model by [65].

The MOT chamber is situated on the lower end of the vacuum chamber. It has various windows for optical access, especially for three counter-propagating MOT beam pairs which are arranged orthogonal to each other. Each pair draws an angle of 45° with the vertical (1-1-1 configuration). Two coils in anti-Helmholtz configuration are integrated into the chamber creating a magnetic field gradient of 0.8 mT/cm with zero field strength in the center of the chamber. Their axis coincides with the axis of one of the laser beam pairs. Additional coils in Helmholtz configuration, placed around the MOT chamber (not shown here), are used to compensate for background magnetic fields in all three dimensions. A rubidium dispenser, which is attached to the chamber, points with its opening towards the center of the MOT region.

The detection chamber situated above the MOT chamber offers access for detection light, a

photo multiplier tube, and a microwave antenna. The two vacuum pumps are mounted outside of the visible plane on opposite sides of the detection chamber.

The interferometer zone is shielded by three layers of a nickel-iron alloy with high magnetic permeability (Mu-metal) to suppress environmental magnetic fields. Inside the inner shielding a precision-wound coil creates a well-defined and homogeneous magnetic field pointing in vertical direction which defines a quantization axis for the atoms. Windows located at the top of the interferometer zone and and at the bottom of the MOT chamber grant optical access for the Raman laser beams.

3.1.2. Active vibration isolator

Vibrations of the retro-reflecting mirror introduce phase noise into the interferometer (see Sec. 2.2.3). Therefore, it is necessary to isolate this component as good as possible from environmental vibrations mainly introduced via the floor of the location. Vibrations include seismic vibrations of the environment as well as man-made vibrations from inside and outside of the building, e.g., caused by machines, people, and traffic. According to the equivalence principle vibrations and accelerations of the mirror can fundamentally not be locally distinguished from accelerations of the atoms. It is only possible to distinguish between changes of the acceleration which occur at high and at low frequencies within a continuous measurement. In the context of gravity, signals at low frequencies with time scales of minutes, hours and longer are of main interest and filtering can remove the higher frequency components. In a pulsed measurement, however, there is a risk of aliasing. A second aspect is the limited region for a linear phase response of the interferometer. It gets smaller for longer time spacings between interferometer pulses which are used to increase its sensitivity. As a consequence, too strong changes of the measured acceleration between two consecutive measurements will degrade the interferometer outcome.

In order to avoid the risks described above and to be able to increase the sensitivity of the interferometer, an active vibration isolation stage is part of the physics package, see Fig. 3.2. It supports the mirror which retro-reflects the two Raman beams and decouples it from ground vibrations. The isolation system was developed and implemented by Christian Freier during his diploma thesis [69] following the ideas made in [70]. It is based on a commercial vibration isolator table 50BM-10 by MinusK which employs a mechanical spring system to isolate its load from vertical ground motions and an inverse pendulum mechanism to decouple it from horizontal vibrations [71]. The passive isolator can be tuned to achieve horizontal and vertical resonance frequencies as low as 0.5 Hz after customization by the manufacturer. A single axis seismometer (CMG-3VL by Guralp) mounted on top of the originally passive isolator detects residual vibrations. Its output signal is processed by a real-time compactRIO computer system by National Instruments controlling two voice-coils inside the vibration table. They exert an additional force on the platform [69, 72]. As a result the effective resonance frequency are lowered significantly to approximately 0.05 Hz and a suppression of one to two orders of magnitude for frequencies between approximately 0.1 Hz to 50 Hz is achieved in our laboratory, see Fig. 3.3. Thus, the isolator allows to use the maximal Raman pulse separation allowed by the height of the interferometer zone of approximately 260 ms and thereby to increase the sensitivity of

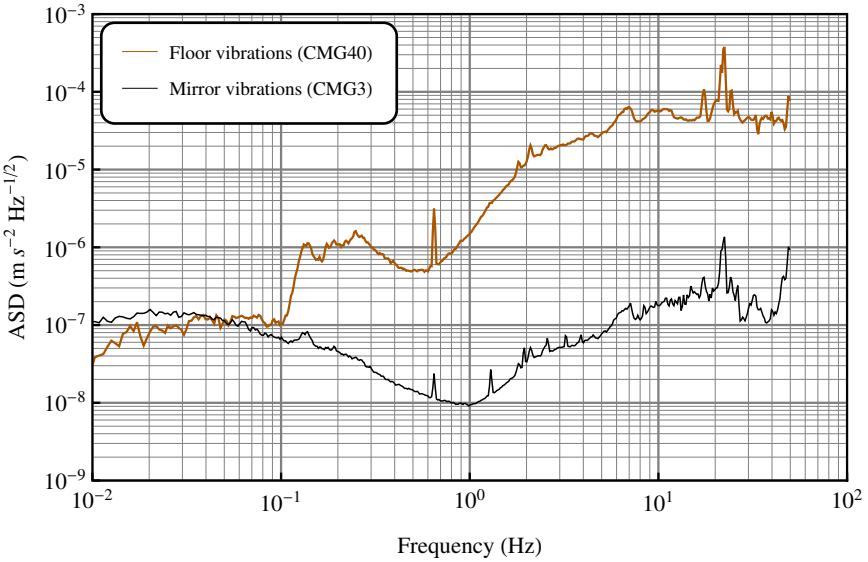

Figure 3.3.: amplitude spectral density (ASD) of the vibrations measured in our laboratory on the floor (orange) and on top of the active vibration isolation system (black). The peak at 0.67 Hz is at the repetition rate of the atom interferometer due to the influence of the MOT coils. The signal of the CMG40 decreases below 0.035 Hz because of its limited bandwidth.

the interferometer. The damping and the low resonance frequency, which is clearly below the Nyquist frequency of 0.35 Hz of the atom interferometer, restrict aliasing effects.

The retro-reflecting mirror is attached to a piezo driven tip/tilt stage (S-330 closed-loop by PI) which is mounted on top of the seismometer. The tip/tilt stage allows for precise control of the tilt of the mirror for correct alignment before and during the interferometer sequence.

Influence on gravity measurements

There are two different influences of the vibration isolation stage on the gravity measurements. The vibrational background, though reduced, is still present and introduces noise limiting the sensitivity of the interferometer. For the calculation, the PSD $S_a(\omega)$ of the mirror vibrations is weighted with the transfer function of the interferometer (see Eqs. (2.48), (2.53), and (2.52) in Chap. 2). This results in a limit for the sensitivity of the interferometer of 115 nm/s^2 per shot for the measurement in our laboratory. At other locations similar limitations occurred, e.g., 143 nm/s^2 per shot during our measurement campaign in Wettzell.

A second aspect is the influence on the phase of the transferred signals which could introduce time delays. It can be determined from the transfer function of the vibration isolator which has been analyzed in [70]. There, the vibration isolation system is described as a spring mass system with the following equation of motion:

$$\ddot{z} + 2\omega_0\zeta_0(\dot{z} - \dot{z_g}) + \omega_0^2(z - z_g) = 0. \tag{3.1}$$

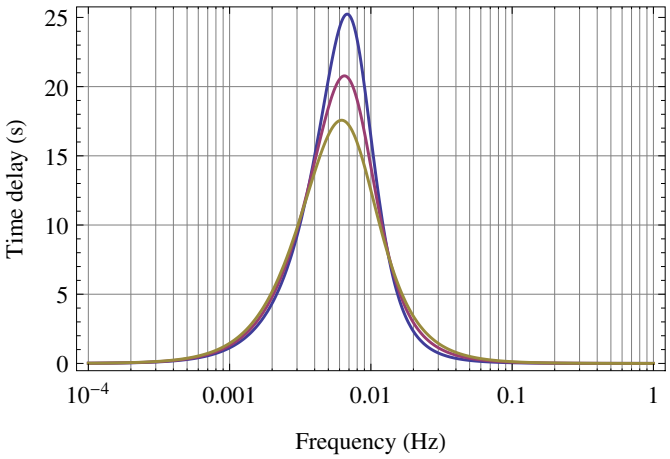

Figure 3.4.: Time delay induced by the active vibration isolator for $\omega_0 = 0.05\,\mathrm{Hz}$ and $\zeta_0 = 0.6$ (blue), 0.7 (red), and 0.8 (yellow).

Here, $\omega_0 = \sqrt{\frac{k}{m}}$ denotes the natural resonance frequency and $\zeta_0 = \frac{\beta}{2m\omega_0}$ is the damping ratio with spring stiffness k and spring damping β. z and z_g are the mass and ground positions. The resulting transfer function then is

$$G = \frac{\tilde{z}}{\tilde{z_g}} = \frac{2(\mathrm{i}\omega)\zeta_0\omega_0 + \omega_0^2}{-\omega^2 + 2(\mathrm{i}\omega)\zeta_0\omega_0 + \omega_0^2} \tag{3.2}$$

where $\tilde{z}$ and $\tilde{z_g}$ are the Fourier transforms of mass and ground motion. For the active system Eq. (3.1) is extended by additional driving forces F_{active} and thereby the effective resonance frequency ω_0 is lowered while the effective damping ratio ζ_0 is maintained or even increased in Eq. (3.2). A time delay $\tau(\omega)$ for transferred signals can be calculated from the phase ϕ of the transfer function

$$\tau(\omega) = -\frac{\mathrm{d}\phi}{\mathrm{d}\omega}. \tag{3.3}$$

The delay for our effective resonance frequency and different, possible damping ratios is shown in Fig. 3.4. There is a significant delay for signals around the resonance frequency. Signals present in our measurements (see Chap. 6) have frequencies above 0.1 Hz (microseism) and below $\approx 3 \times 10^{-4}\,\mathrm{Hz}$ (tidal signals) and are therefore essentially not delayed.

3.2. Laser system

The laser system for the GAIN experiment has to meet special requirements. In contrast to typical experimental laser setups, which cover large optical tables and benefit from their mechanical stability and from the precise temperature control typically available in optical laboratories, a mobile implementation has to fulfill additional and also much stronger requirements. Limitations regarding size and weight have to be considered and the performance and reliability have to be

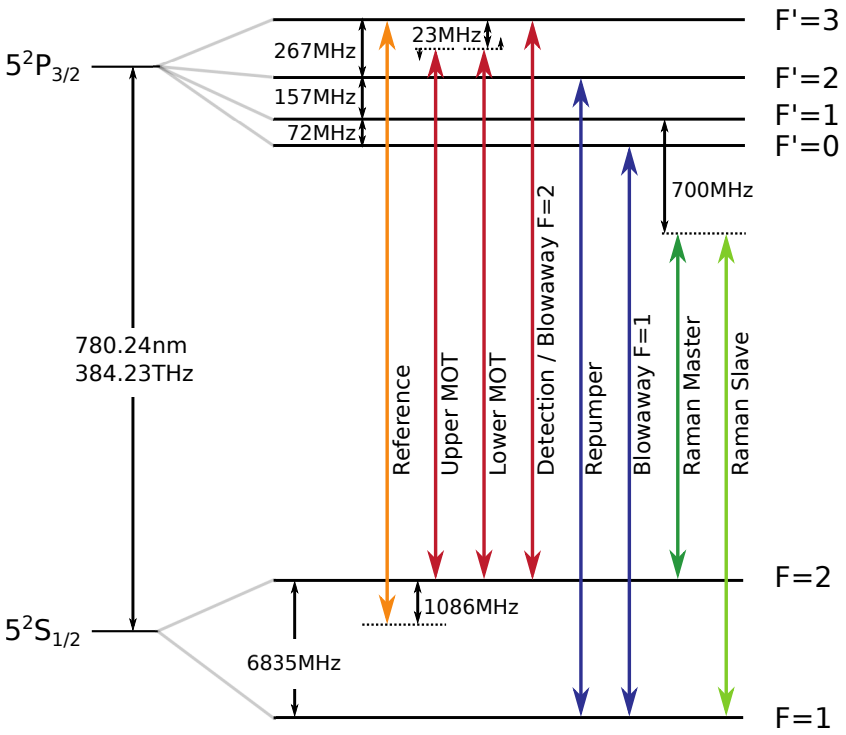

Figure 3.5.: ^{87}Rb D2 level scheme and laser frequencies required in the experiment. Values adopted from [64].

maintained while environmental influences increase at the same time. Especially the objective to perform precision measurements lasting for a few weeks which require constant conditions, e.g., regarding stability in optical frequency and optical power of several laser sources, have to be met.

The original implementation of the laser system including all laser sources and their stabilization were designed and described in detail during a former work by Malte Schmidt [66, 67]. For this reason only a brief introduction is given here on the original system and the main focus of this part concentrates on the strongly improved switching and distribution modules and on the newly implemented intensity stabilization for the Raman lasers.

3.2.1. Laser frequencies and sources

The laser system has to provide several specific frequencies at different powers during each single phase of the experimental cycle. All of them are generated by five semi-conductor laser diodes, either by extended cavity diode lasers (ECDLs) or distributed feedback lasers (DFBs). Three of them are afterwards amplified by tapered amplifiers (TAs) in order to provide sufficient optical powers.

Figure 3.5 illustrates the required frequencies and also shows the atomic level scheme related to the ^{87}Rb D2 transition. Each color represents one laser source. During the MOT phase cooling and repumper light is needed of which the former requires an adjustable detuning to the

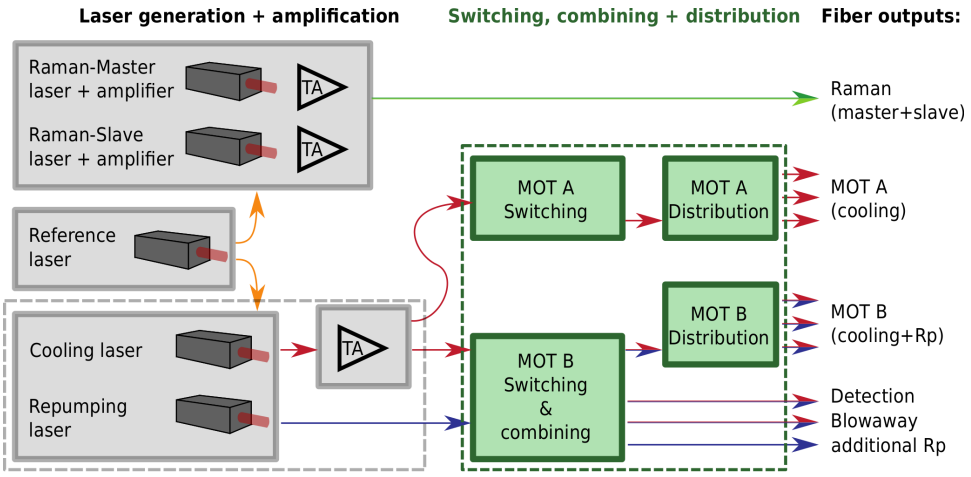

Figure 3.6.: Overview of the laser system and its optical connections: five laser sources on the left (gray) generate the required laser frequencies. A new developed distribution system (green solid boxes) allows for combining, fast switching and individual frequency detuning for upper and lower MOT beams while maintaining optical output powers over months even in the case of temperature variations. The dashed lines indicate the division of the former system.

red relative to the ^{87}Rb $|F = 2\rangle \rightarrow |F' = 3\rangle$ transition. In addition, the upper and lower MOT beams have to be detuned relative to each other for the launch of the atomic cloud. Detection and blow-away light can be obtained by further detuning of the two laser sources. Two more laser sources generate the Raman light. For the latter ECDL lasers are used because of their reduced linewidth below 100 kHz allowing for low noise phase locks. Another ECDL serves as a dedicated reference laser and is stabilized via Doppler free modulation transfer spectroscopy (MTS) near the ^{85}Rb $|F = 3\rangle \rightarrow |F' = 4\rangle$ transition. The frequencies of the other lasers are stabilized with adjustable offsets relative to this reference. Fast photodiodes detect the beat notes between the lasers whose phases are compared to the phases of radio frequencies (RFs) by electronic phase frequency detectors (PFDs) controlling among others the laser currents. Thus, each of these four laser diodes can be used for different purposes, e.g., for cooling, detection, and controlled removal of certain atoms (blow-away) when guided to the appropriate polarization maintaining (PM) optical fiber. Fast switching and the detuning between upper and lower MOT beams is achieved via acousto-optic modulators (AOMs).

3.2.2. Modular setup

The laser system is divided into different laser modules which are connected by PM optical fibers. The smaller units offer a higher mechanical stability and simplify the optical alignment in comparison to one larger module. An overview of the modular setup and the optical interface is shown in Fig. 3.6. The dashed boxes indicate the partition which was used in the original setup before the number of modules has been increased. Four (formerly three) modules house the laser sources, optics and electronics for frequency stabilization, and the TAs for amplification. A

new TA with an optical output power of 2 W[2] replaces two TAs with 1 W output power for the amplification of the cooling light which were included in the appropriate laser module before. The additional module ensures a more constant power output and particularly a more constant power ratio between its fiber outputs for MOT A and B. Its implementation and characterization was realized in a bachelor thesis and is described in [73]. Light of the Raman master and slave lasers is overlapped after amplification and guided by a single fiber to the experiment.

The switching, combining and distribution subsystem (in green) was originally implemented inside one complex module. Its tasks include fast switching and complete beam blocking via AOMs and mechanical shutters, overlapping of cooling and repumper light, and the distribution on a number of optical fibers. They finally guide the laser light to the vacuum chamber. In addition, the AOMs allow to detune the cooling light of the MOT A and B outputs to slightly different frequencies for the launch of the atoms. It has been replaced by four smaller and improved modules during this work in order to meet the requirements for mobile and long-term measurements. Starting with a study of the former module and its limitations, the development of the new modules is described in the following.

3.2.3. Original switching module

Figure 3.7 shows a CAD drawing of the original implementation of the switching and distribution module. It makes use of AOMs in double pass configuration, where the diffracted order is back-reflected to pass the AOM for a second time. The two times diffracted beam has a perpendicular polarization relative to the initial beam after passing a $\lambda/4$ waveplate twice. This way it can be separated with the help of a polarizing beam splitter (PBS) situated in front of each AOM. Additional $\lambda/2$ and PBS optics allow for overlapping of the different laser frequencies and for distribution onto the various output fibers afterwards. Each of the two cooling beam paths (red lines) have a lens included into the double pass, which in combination with the back-reflecting mirror forms a cats-eye configuration. For slightly changing AOM frequencies it ensures almost unvarying beam paths after the second transition and thereby constant fiber coupling efficiencies. When used in detection mode the AOMs are further tuned such that the beams hit small pick up mirrors and take different paths towards the fiber couplers for detection and blow-away light. For a detailed description see [66].

The realization of the double pass configuration and the pick up technique require a number of additional optics and result in long beam paths and a relative large module[3] with outer dimensions of $43 \times 43 \times 10\,\mathrm{cm}^3$. It was found that the module had to be readjusted after transportation to a different location in order to recover sufficient optical powers at the output ports. The time needed for this was several days due to the complex setup and the high number of adjustable mirrors. This was too long for a mobile system. Hysteresis effects and a quite inconvenient handling of the adjustable mirrors complicated the procedure. The former also influenced the long-term stability during several days after the re-alignment process.

[2] EYP-TPA-0780-02000-4006-CMT04-0000 from Eagleyard photonics

[3] The module is still much smaller than a typical setup on an optical table would be.

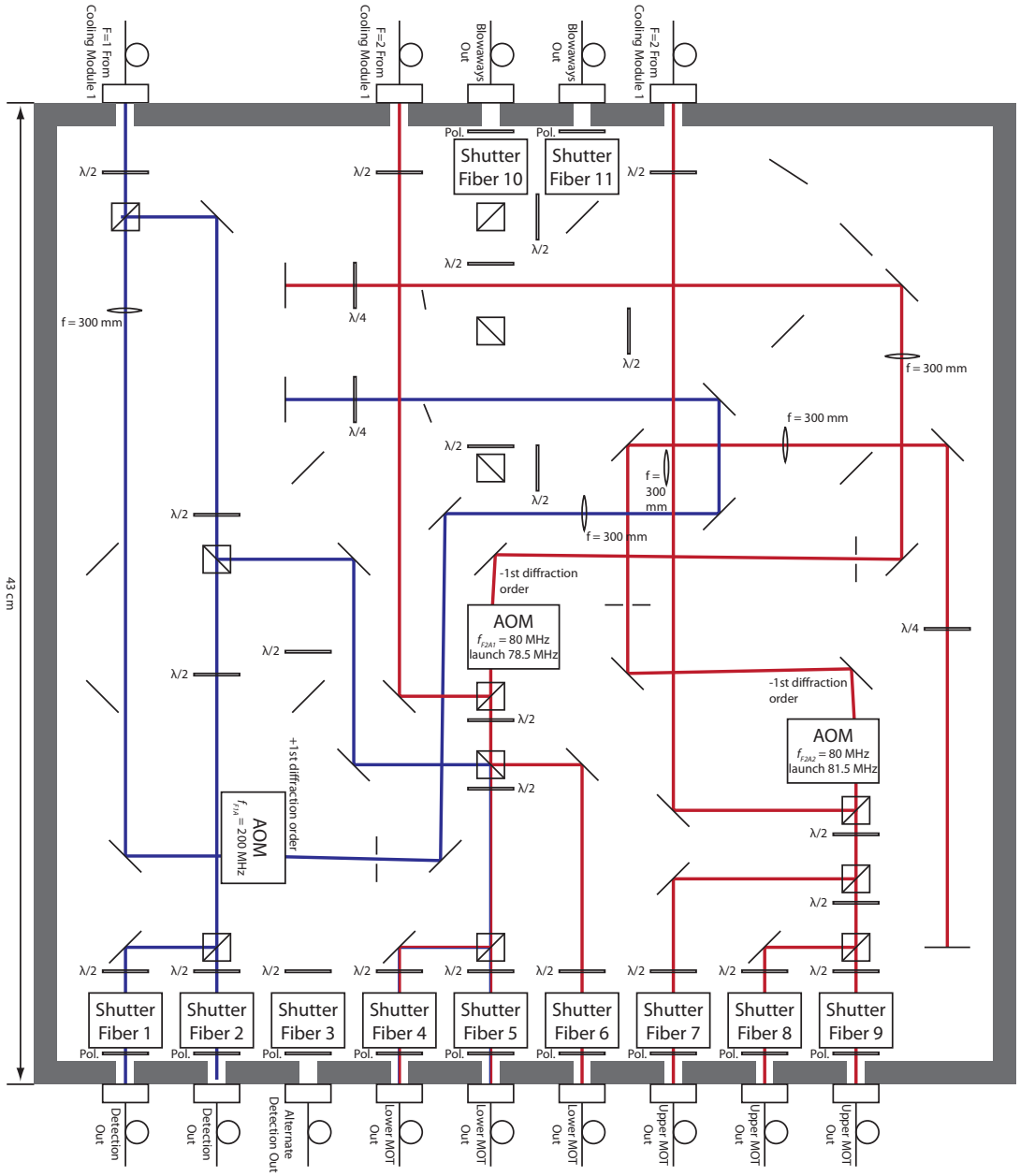

Figure 3.7.: Old laser module for MOT switching and distribution, from [66]. Beam paths of the cooling light (red) and repumper light (blue) are shown for the MOT operational mode. Optics which are not part of the shown paths are required for the second operational mode during detection.

3.2.4. New switching modules

A completely new switching and distribution sub-system has been developed during this work to meet the stability requirements outside of optical laboratories, reduce the time needed for re-alignment after long transportation, and allow for drift free long-term gravity measurements. The sub-system includes distinct modules for the upper and lower beam triplets of the MOT light (A and B), which allow for independent frequency detuning of each triplet and fast switching via AOMs. Additionally, cooling and repumping light is combined (only MOT B) and the light is distributed onto several output fibers guiding it to the vacuum chamber. The external optical interface of the sub-system has undergone only minor modifications and still covers all important outputs.

In order to fulfill all the requirements the new MOT switching system was designed with respect to the following design criteria:

Decrease in beam path lengths: Shorter path lengths reduce the impact of small changes of the pointing on the fiber coupling efficiency.

Lowering the number of adjustable mirrors: Temperature variations might cause creeping of the mirror mounts. In the new design only fixed mirror mounts are used.

Sub-division: Different functions are distributed among a few smaller sub-modules. Thus, the complexity of each module is further reduced.

Improvement of mechanical stability: Each module (baseplate including walls) is milled out of a single piece of aluminum to reduce mechanical stress.

MOT A module

CAD drawings of both switching modules are shown in Fig. 3.8. The MOT A module on the left involves one adjustable fiber coupler (cooling in), an AOM for fast switching and frequency detuning of the laser light and a shutter to completely block the light. At the output a fixed fiber collimator is used, which ensures that the position and angle of the output fiber relative to the AOM cannot drift. Thereby the degrees of freedom could again be reduced. The alignment of the elements has been realized with laser light pointing in reverse direction. An additional mirror in front of the shutter blocks the zeroth diffraction order of the AOM away. The PBS and the non-adjustable mirror allow to lead part of the light to a second, optional output. They are not included in the standard configuration.

The lenses included in the fiber coupler and the collimator[4] have a focal length of only 2 mm, which is the shortest focal length for this wavelength available from the manufacturer. As a result the beam diameter is only ≈ 0.5 mm for a fiber with a numerical aperture (NA) of 0.13 and the different diffraction orders of the AOM can be separated already in a distance of 5 cm. A second advantage is the more favorable dependence of the coupling efficiency regarding slightly inclined beams. The beam pointing changes with different Bragg angles at different AOM detunings. During the interferometer sequence the AOM frequency has to be changed

[4]Fiber coupler 60SMS-1-4-A2-02 and collimator 60FC-4-A2-02 from Schäfter+Kirchhoff

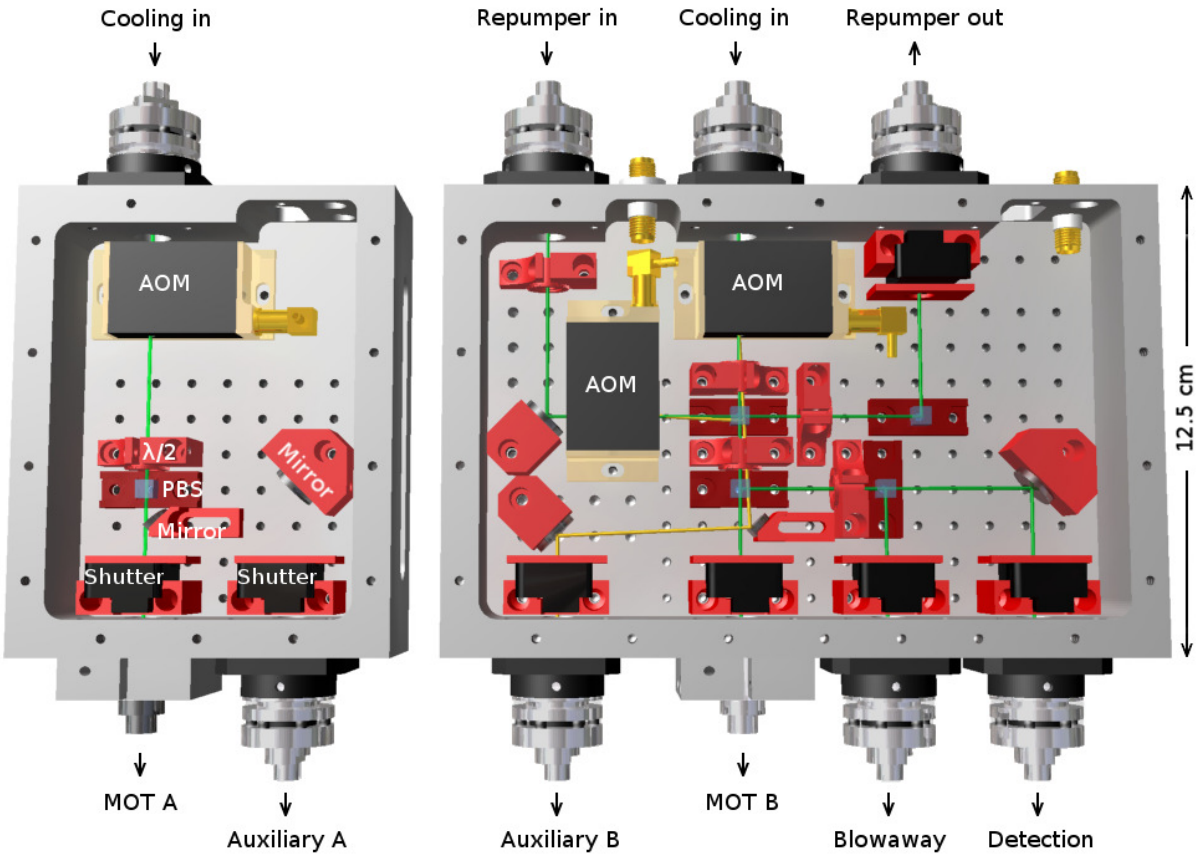

(a) MOT A switching module: the cooling laser beam is diffracted by an AOM and its +1st order is coupled into an optical output fiber. The zeroth order is removed with the help of a precisely placed mirror.

(b) MOT B switching module: the cooling-MOT path is similar to (a). In addition, the +1st order of the cooling beam is superimposed with the -1st order of a second beam (repumper) at the nearest PBS. Thus, both diffracted orders couple to the output fiber (MOT) while both 0th orders (yellow beams) hit the same mirror and can be guided to another fiber output (auxiliary port). At another PBS a small part of the light is extracted for the blow-away and detection beam outputs.

Figure 3.8.: CAD models of the new developed switching modules on a scale of $\approx 1:2$.

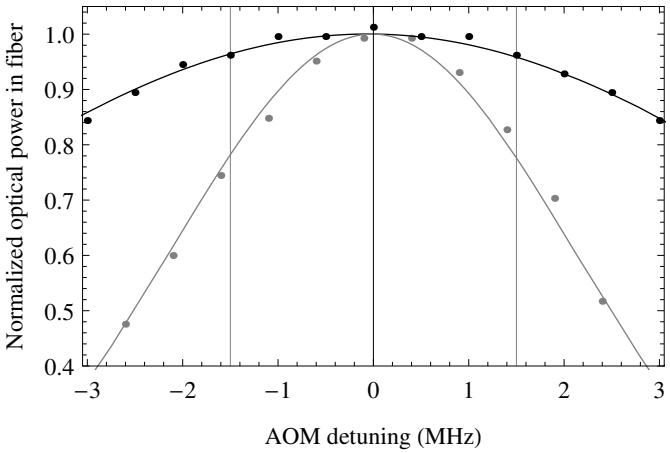

Figure 3.9.: Relative optical power in fiber depending on the AOM detuning for coupler lenses with a focal length of 4.5 mm (gray) and 2 mm (black). The measured values and the fitted curves are normalized with their maximum value at zero detuning.

by 3 MHz for launching the atom cloud. Using a focal length of 2 mm the additional losses for operation at ±1.5 MHz off from the center with maximal efficiency are reduced to 5 %. A lens with a focal length of 4.5 mm, which was used before, in comparison causes losses of 22 %. The reduction of the losses is due to the smaller distance between the lens and the fiber which results for a given tilt in a smaller lateral displacement between the mode fields of the fiber and the laser light. A measurement of the dependence on the AOM detuning is shown in Fig. 3.9 for both beam diameters .

The main disadvantage of a shorter focal length and thus a smaller beam diameter is the reduced maximal working range between two fiber couplers which is about 26 cm for the chosen configuration [74]. Longer distances would result in reduced fiber coupling efficiencies.

MOT B module

The MOT B module, shown in Fig. 3.8(b), has a similar configuration for the "cooling-MOT" beam path as the previous module but also includes several extensions. First, the cooling light is superimposed on a PBS with a second beam containing light from the repumping laser. Behind a second PBS the initially perpendicular polarizations become parallel at the cost of some power loss which is guided to the second output port. The latter is used for the blow-away and detection beams. The half-wave plates in front of each PBS determine their splitting ratios and guide 90 % of the cooling light and thus 10 % of the repumping light to the MOT fiber output.

The two AOMs are placed at equal distances from the nearest PBS and apply opposed diffraction orders, such that both their diffracted and non-diffracted orders are superimposed. In this way the latter (yellow beam in Fig. 3.8(b)) can both be separated by a small mirror and redirected to an auxiliary fiber port. It has no distinct function at the moment but might be used for future extensions such as a 2D-MOT or as a Raman laser source when supplied with appropriate laser light. The non-diffracted beams pointing towards the blow-away and detection

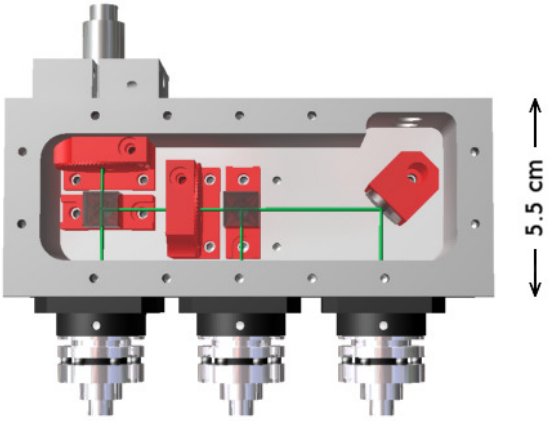

Figure 3.10.: The MOT distribution module (equal for MOT A and B). The incoming cooling (with superimposed repumper) light is distributed onto three fiber output couplers. Waveplates and PBSs allow to adjust the beam balances.

outputs are not shown since they carry far less power and do not couple into any fiber due to their displacement. The port at the top right can be used to extract only one of the two frequencies like the repumping light, which is selected by polarization. Each of the output ports is equipped with a mechanical shutter right in front, which allows to use different ports during different experimental phases.

In order to be able to monitor optical powers inside the module during the regular interferometer operation all mirror mounts house additional photodiodes. These are placed in the line of sight directly behind the mirrors such that a small fraction of the light still transmitted can be detected[5].

After having passed the switching modules the respective MOT light is guided via a PM fiber to one of two identical distribution modules. A drawing is shown in Fig. 3.10. Inside, combinations of wave plates and PBSs allow to adjust the beam balance of the output fiber triplet supplying the magneto-optical trap. For the input a fixed fiber collimator is applied in order to reduce redundant degrees of freedom and improve long-term stability. The mirror includes a photodiode for power monitoring.

Physical dimensions and efficiency

The physical dimensions of the modules could drastically be reduced compared to the former module. The total free optical path lengths up to the first output port of the MOT beam triplet, summed up for the switching and distribution modules, are only 18 cm and 24 cm long for the cooling and repumper light respectively. This is a reduction by a factor of ≈ 10 compared to the former module with path lengths of 173 cm and 274 cm. The shorter path lengths plus a lower

[5] Even though mirrors with a high reflective coating are applied, they still transmit a small part of the light. The fractional amount is dependent on the incident polarization. Thus, this method is only applicable to light with stable polarization for example after having passed a PBS or another optical polarizer.

	Losses	Remaining
Switching module MOT B		
Fiber input	-	100%
Typical AOM losses	15%	85%
AOM detuning	5%	81%
PBS losses (2 PBS)	8%	74%
Overlap with repumper/ splitting for detection and blowaway light	10%	67%
Typical fiber coupling losses	15%	57%
Distribution module		
PBS losses (2 PBS)	8%	52%
Typical fiber coupling losses	15%	44%

Table 3.1.: Optical losses and remaining powers inside the switching and distribution modules for MOT B.

beam height of only 8 mm (instead of 20 mm before) inside the switching modules reduce the volume of the largest laser module to only $12.5 \times 19 \times 4\,\mathrm{cm}^3 \approx 1\,\mathrm{l}$. All four modules together have a volume of 2.2 l, which is only 12 % in comparison to the volume of the former module.

The switching and distribution modules for MOT B allow to guide about 44 % of the incoming laser light for cooling to the vacuum chamber. The particular losses are listed in Tab. 3.1. An additional 6 % of the incoming light can be distributed between the blow-away and the detection beams. For MOT A the losses due to overlap/splitting cancel. The absolute optical powers are about 50 mW at each of the six MOT fibers while the TA is operated at approximately 80 % of its nominal output power.

Figure 3.11 shows the normalized intensities observed behind the three output fibers belonging to the MOT A distribution module over the course of ten days. They have been measured with photodiodes which are integrated in the MOT telescopes at the vacuum chamber. The variations include all effects from the TA, the switching/distribution modules, and the optical fibers and typically stay below 5 %. The oscillations on time scales of a few hours are only visible on fiber 7 and therefore cannot be caused by the TA or the modules. They are most likely due to a slightly changing polarization on the fiber which result in intensity variations at the polarizer in front of the photodiode. The intensities on fiber 8 and 9 show less variations. After one year without any re-alignment of the switching and distribution modules, which included a transport from South Germany back to Berlin within this period, their efficiencies still are nearly 40 %.

3.2.5. Raman intensity stabilization

The original Raman module (see [66]) has been extended by an active intensity stabilization. A schematic overview of the optical set-up with its electronics is shown in Fig. 3.12. The Raman laser light is generated in a master oscillator power amplifier (MOPA) configuration where two ECDLs generate the Raman Master and Slave laser light and two subsequent TAs amplify the light to achieve sufficient optical power. Optical isolators (not shown here) behind each laser

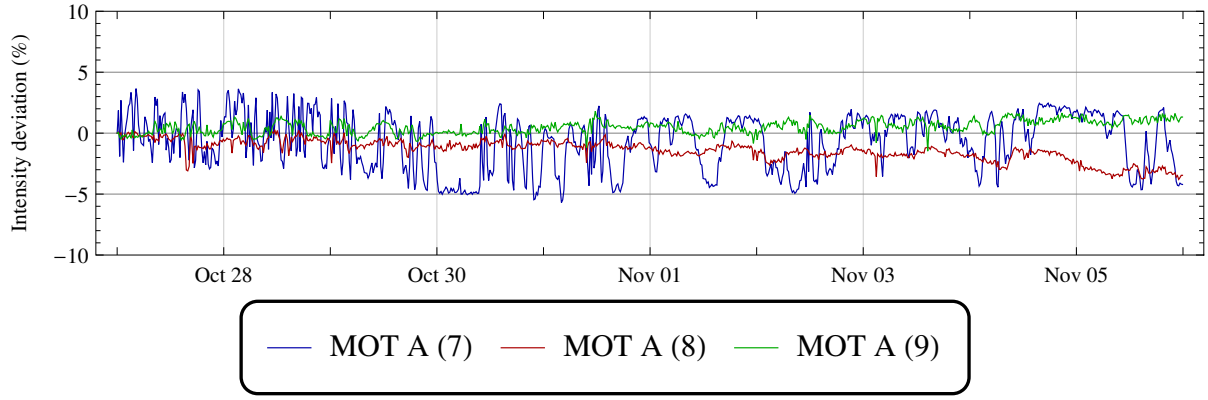

Figure 3.11.: Intensity deviations of the three MOT A fibers recorded behind a polarizer at the vacuum chamber. Data has been filtered using a moving average over ≈ 30 min. All variations stay below $\pm 5\,\%$. Fiber 7 (in blue) shows oscillations on time scales of a few hours which are not visible on fibers 8 (red) and 9 (green).

source and amplifier avoid that reflections from further components get back to the devices. The beams are superimposed and projected onto a common polarization by two consecutive PBSs. Then, the light is coupled into a short PM optical fiber which ensures identical pointing and therefore identical optical losses for both beams afterwards. Behind the fiber an AOM allows for fast switching and thus for precise and short Raman pulses before the light is coupled into the output fiber. Fast photodiodes detect the beat notes between the Raman Master and the reference laser beam and also between the two Raman beams for the electronic phase locks. Further photodiodes monitor the optical power of the laser beams (PD1) and laser light that gets back through the output fiber with rotated polarization (PD2). The latter is used for tilt monitoring and control (see Sec. 5.2).

The optical power of the Raman laser beams influences two different aspects of the Raman transitions. On the one hand, for fixed relative intensities, the total intensity of the master and the slave beam determines the Rabi frequency and hence the duration of a $\pi/2$ and a π pulse respectively. On the other hand, their relative intensities can in addition cause a phase shift in the interferometer due to AC-Stark shifts of the atomic level structure (see Sec. 5.6). In order to keep the Rabi frequency and light shifts constant, the intensity stabilization controller re-adjusts both TA input currents approximately every 20 min in between two consecutive series of measurement. Therefore, the controller includes two proportional-integral (PI) circuits which are directed by a micro controller. The circuit diagram can be found in the Appendix B.

During the regulation of the intensities the Raman Slave phase lock is switched to a “hold mode” that keeps the latest parameters (laser current and piezo voltage) for the ECDL constant. Then, the Raman Master beam is blocked by a shutter and the Slave intensity detected by “PD1” is regulated to its reference value. Afterwards, the Raman Slave beam is blocked instead and the Master intensity, detected by the same photodiode, is regulated. Finally, the beams are unblocked, the phase stabilization is automatically re-activated, and the TA currents are kept constant. The complete sequence lasts less than 0.1 s.

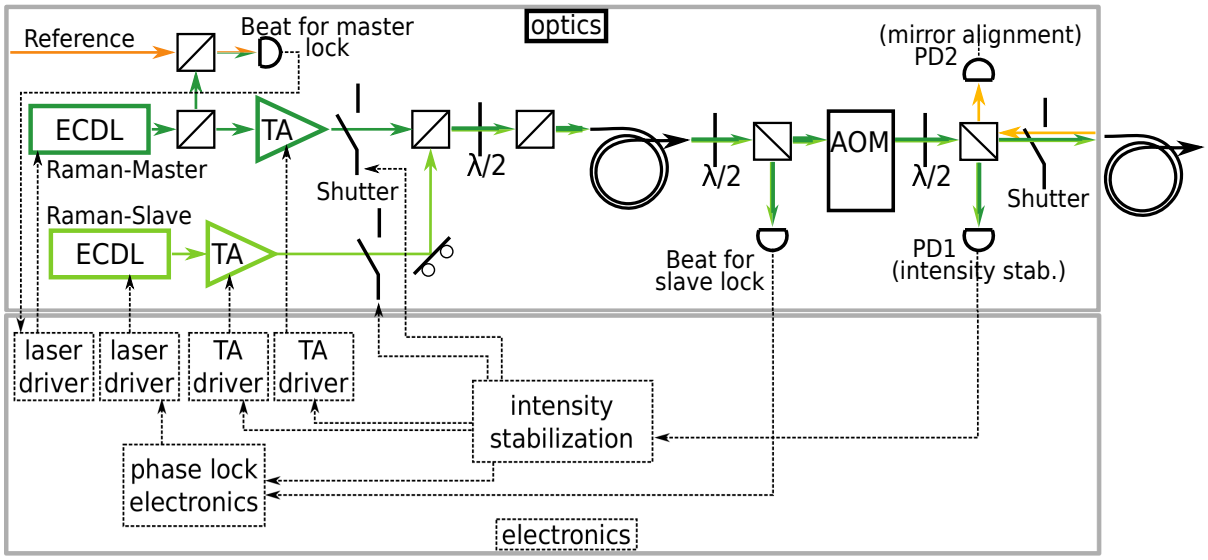

Figure 3.12.: Simplified scheme of the Raman optics and electronics with active optical intensity stabilization. Optical isolators and additional mirrors are not shown for clarity.

A second operational mode allows to block the Raman Slave laser for a longer period while again the parameters for the phase lock are kept constant and the phase stabilization is re-activated afterwards. This mode is used for sequences which include pulses with both beams and pulses with a single beam, e.g., for doing spectroscopy after the velocity selection (see Sec. 5.3.2).

3.3. Timing system and data storage

The successive phases of the experiment need very different configurations with diverse optical access ports and changing optical frequencies. For the Raman pulses, a very precise timing is required. These demands are met with a PXI computer system from National Instruments which includes a field programmable gate array (FPGA). The program on this system was realized with the visual programming language Labview. All events and their exact timing can be inserted in advance into a user interface. The program then creates the corresponding code for the FPGA. During the sequence the latter controls the experiment via digital and analog channels of additional I/O cards and by commanding five direct digital synthesizer (DDS) boards. They generate the required frequencies and frequency chirps for AOMs and laser frequency stabilization. In parallel the user or an additional routine can change the event list for the next run. The new sequence is loaded at the beginning of the next run during the MOT phase. All clocks of the FPGA and the DDS are synchronized to a stable frequency reference DLR-100 from Spectra Dynamics which generates 10, 100 and 300 MHz from a 5 MHz Wenzel Blue Top quartz. For a closer examination of the computer system and its timing accuracy see [65].

Data storage

For efficient and complete data storage a database structure has been developed as part of this work. It reflects the various control parameters and has been implemented into a MySQL database. For each experimental run the measured data and the complete control sequence, consisting of the event lists for the I/O cards and the DDS boards, are stored into the database. This way the parameters for each single measurement can be reloaded and compared to the ones of other measurements. The single measurements are organized in measurement series, e.g., representing a scan of a certain parameter. Using the database efficient storing and searching of the data is ensured.

The structure of the database is visualized in the enhanced entity-relationship diagram in Fig. 3.13. In the upper and lower box the tables for the measured data and the control sequence are shown, respectively. The series of measurements are stored in the table *Messreihen* and all individual measurements are saved in the table *Messungen*. Each series is connected to the corresponding measurements with a one-to-many (1-∞) relationship via an identifier. In the same way each single measurement is related to the many digitized samples of the photomultiplier tube (PMT) signal which are stored in the tables *Messwerte* and *Nullmessungen* for the detection and background detection signals, respectively. This way the sample rate and the total number of samples can be changed for different measurements. Digitized data from the seismometers are stored in the table *Vibration_Data*.

Each single measurement is connected to the corresponding computer sequence which has been used for controlling the experiment by a one-to-one (1-1) relationship. The sequences are stored in 5 tables in total of which the table *Sequenzen* contains a unique entry for each sequence. It provides identifier to resolve the relations to the other tables. A recent modification allows to reuse the identifier for entries in the table *Sequenz_Arrays*, when they have not changed in between consecutive measurements, for a more efficient storage. For a single run ($\approx 1.5\,\mathrm{s}$) typically 10^3 to 10^4 measured values and sequence parameters, such as timing information, channel numbers, output values and so on, of various data types and precision have to be stored. During continuous operation this results in memory requirements of $\approx 2\,\mathrm{GB}$ per day.

The tables can be easily extended if further parameters have to be stored in the future. Routines for the analysis will not be affected since every parameter can still be loaded via the measurement or sequence identifier and the parameter name. Data is subsequently stored starting with the tables on the lowest level to ensure that all available entries in the tables *Messungen* and *Sequenzen* represent a complete data set even in the case of failures, e.g., when the saving process has been interrupted for any reasons. The timing system has been prepared to automatically store all data whenever a measurement series is started such that no data can be lost. All information is nearly instantly available for analysis on any computer within the network and without the need to handle any files. An automatic duplication to another computer has been realized using the MySQL replication routine.

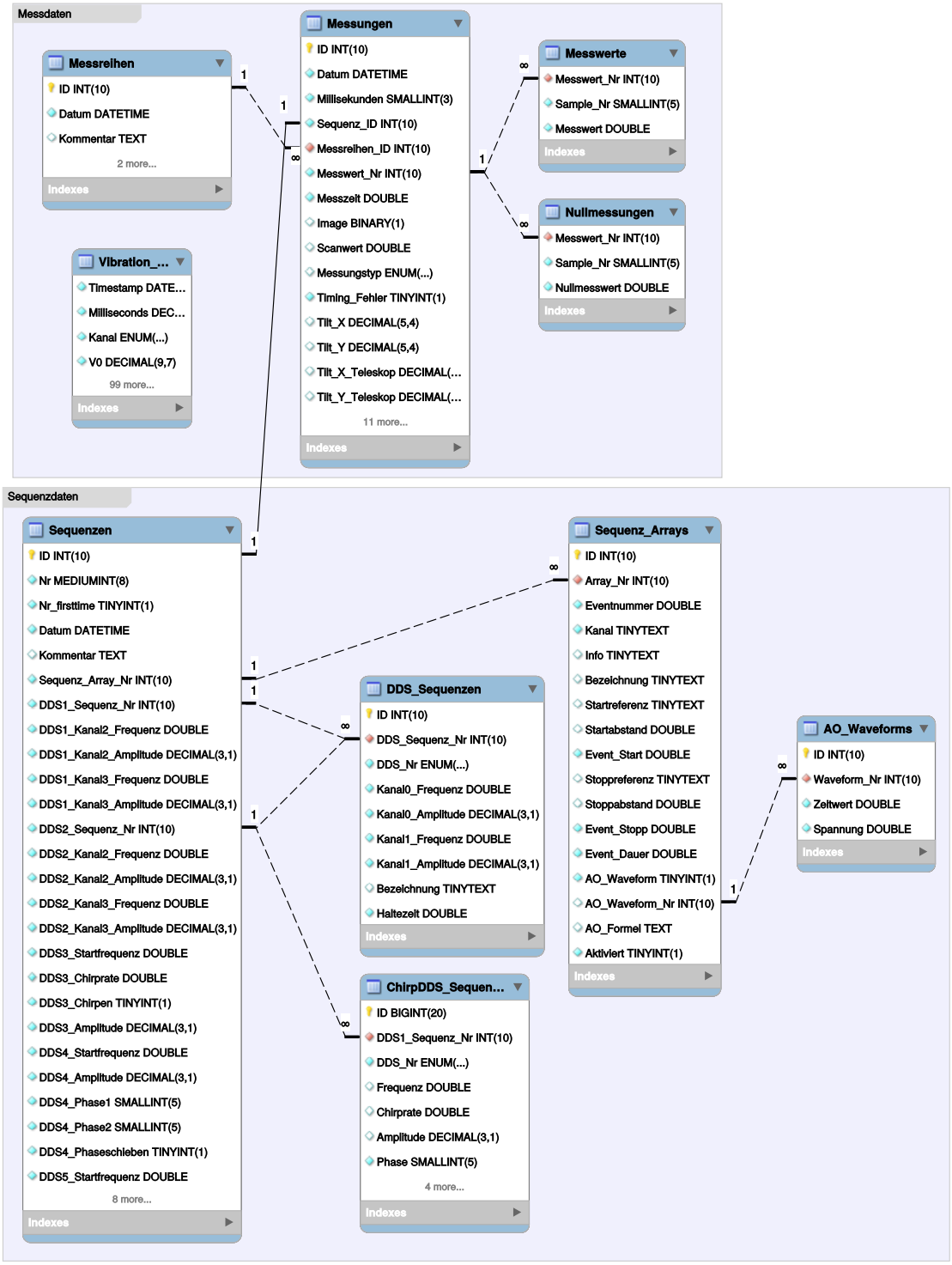

Figure 3.13.: Database structure with tables for measured data and experimental parameters (upper/lower box) and their relationships.

4. Gravity measurement

In this chapter, the experimental sequence, including the preparation of the atomic cloud, the interferometer pulses, and the detection, is described. It is applied during each single run of the interferometer. Afterwards, an initialization process, necessary to reach unambiguousness of the measured interferometer phase, and a measurement protocol are illustrated in Sec. 4.2. The procedure is the basic principle for all gravity measurements presented in this work. It is based on the one presented in [65, 66] with a few minor modifications. Due to the more stable laser system and a more precise adjustment it was possible to permanently reduce the final temperature of the atomic cloud after the launch from formerly $6\,\mu$K to only $1.9 \pm 0.1\,\mu$K. This results in an improved signal to background ratio during detection. The detection sequence has been extended by a third pulse to get additional information on the flight curve of the cloud. In addition, the computer control system has been improved enabling for a more advanced measurement protocol with alternating directions of the effective Raman wave vector between single runs. Both measures will be of use for the analysis of systematic effects later on. Finally, in Sec. 4.3 the results of a first gravity measurement showing typical influences from the Earth's tides are discussed.

This chapter also provides the basis for all gravity measurements taken for the analysis of systematic effects and during the comparison campaigns for long-term characterization of the instrument which are discussed in Chapters 5 and 6.

4.1. Experimental sequence

The atom interferometer is operated in pulsed operation and every single measurement lasts for approximately 1.5 s. Each cycle starts with the preparation and launch of a cold atomic cloud during the MOT and molasses phase which is followed by a selection process. Afterwards, the cloud is left in free fall on its parabolic trajectory only interacting with three Raman light pulses which create the interferometer and are separated by the time T. Finally, the population ratio of the inner states is determined via fluorescence detection.

4.1.1. MOT and optical molasses

Within the magneto-optical trap (MOT) zone six laser beams with circular polarizations are arranged in a 1-1-1 configuration and meet each other at the center of the chamber at right angles (see Sec. 3.1.1). In combination with a magnetic quadrupole field from anti-Helmholtz coils a MOT configuration is formed which allows for trapping of atoms in its center and also for cooling of the emerging atomic cloud [75–77]. In our configuration all laser beams are tuned 20 MHz to the red of the ^{87}Rb $|F = 2\rangle \rightarrow |F' = 3\rangle$ closed transition, which corresponds to

about three atomic linewidths, such that atoms more often scatter photons from a counter-propagating than from a co-propagating beam. This is due to the Doppler effect which shifts the laser frequency closer to the atomic resonance in the former case and further away in the latter case. As a result the atoms are decelerated and a lower mean velocity is achieved which can be connected to a lower temperature via the Maxwell-Boltzmann distribution.

In addition, a magnetic field gradient of 0.5 mT/cm causes a spatially dependent Zeeman shift lifting the degeneracy of magnetic sub-levels. Thus, the scattering rate is enhanced for either σ^+ or σ^- polarized light while the other one is reduced in dependence of the position of the atom relative to the center of the MOT. This gives a spatially dependent force and creates a trap. Three Helmholtz coils are used to compensate for background magnetic fields to ensure the field minimum to be in the center of the chamber.

A second overlapped laser beam, the repumper, is in resonance with the ^{87}Rb $|F = 1\rangle \rightarrow |F' = 2\rangle$ transition and transfers atoms scattered by chance to the $|F = 1\rangle$ state back to the atomic levels involved in the cooling process. The beam diameters are 30 mm ($1/e^2$) and have 40 mW of cooling light per beam and 5 mW of repump light in total.

During the MOT loading time of 600 ms some 10^8 rubidium 87 atoms are captured from the vapor emitted by the dispenser and from the background vapor present in the vacuum chamber. At the same time the atoms are cooled due to the velocity dependent light forces. During the last 5 ms the magnetic coils are switched off and residual magnetic fields decay resulting in an optical molasses without spatially dependence of the light forces. Afterwards, the upper and lower beam triplets are detuned by 3 MHz to the red and blue respectively for 3 ms. This way the atomic cloud is accelerated to a mean velocity of 4.05 m/s upwards in vertical direction. During the last 2 ms laser intensities are in a first step reduced and then adiabatically ramped down and the mean red detuning is increased to 144 MHz to further decrease the temperature of the cloud. The repump laser is switched off only 3 ms afterwards to ensure that all atoms finally are in the $|F = 2\rangle$ state.

Final temperature of the atomic cloud

The final temperature of the molasses determines the mean velocity of the atoms and as a consequence the expansion rate of the atomic cloud. This influences its spatial extension at the time of the Raman pulses of the interferometer and also during the detection sequence after 778 ms of free fall. In order to detect as many of the atoms as possible in the limited detection area the temperature should be as low as possible.

The temperature of the atomic cloud is determined by testing the population of different velocity classes [78]. A velocity selective Raman pulse transfers a certain velocity class from the $|F = 2\rangle$ to the $|F = 1\rangle$ internal state. In our configuration both Raman beams enter the vacuum from the top with equal linear polarization and are retro-reflected at the reference mirror below the vacuum chamber. A $\lambda/4$ retardation plate mounted on top of the mirror turns the polarization of the reflected beams by 90°. The atomic transition is driven by one beam coming from the top and one from the bottom with orthogonal linear polarizations (lin $\perp$ lin configuration). Therefore, the frequency difference between the lasers is tuned to match the sum of the hyperfine splitting and twice the Doppler shift of the atom (there is a Doppler shift for each beam with a different sign depending on the pointing direction of the laser beam). As

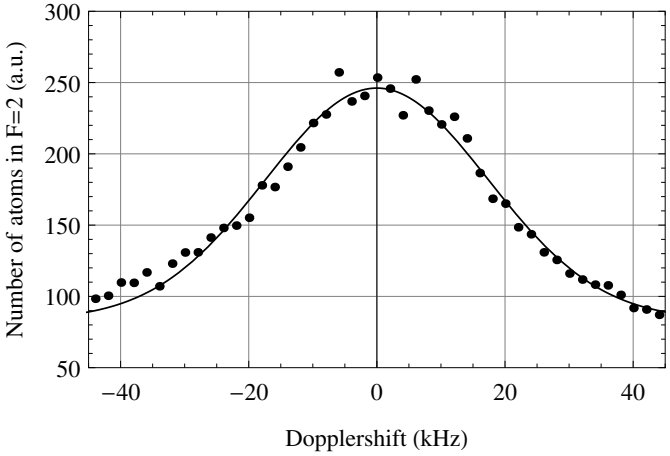

Figure 4.1.: Temperature determination using velocity selective Raman pulses. A Gaussian fit (black line) reveals a corresponding temperature of the rubidium cloud after optical molasses of $1.9 \pm 0.1\,\mu$K.

a consequence the second beam pair is shifted out of resonance and only the first beam pair drives the Raman transition. After the Raman pulse, a fluorescence detection scheme is used to determine the population of the two internal states (see Sec. 4.1.4).

In a series of experimental runs, each performed with a slightly different frequency of the Raman pulse, atoms of different velocity classes are transferred. Figure 4.1 shows the number of atoms in the $|F = 2\rangle$ state plotted against the relative Doppler shift. The full width at half maximum of the Gaussian distribution is $40.9 \pm 1.3\,$kHz corresponding to a temperature of $1.9 \pm 0.1\,\mu$K. This result is almost identical to the coldest temperature value of $1.8\,\mu$K for an optical molasses with ^{87}Rb found in literature [79].

4.1.2. Selection process

In the interferometer sequence for the measurement of the gravity acceleration a Raman π pulse is used to select atoms of one central velocity class shortly after the launch. The pulse has a Gaussian intensity variation in time with a width of $56\,\mu$s. It only transfers atoms within a certain velocity spread which is determined by its spectral width $\Delta\omega$ according to the Heisenberg uncertainty principle $\Delta\omega\tau \geq \frac{1}{2}$. The corresponding temperature to this spread is approximately 13 nK. The pulse length is chosen to last about three times longer than the π pulse of the interferometer applied later on. By this means, nearly uniform resonance conditions can be ensured for all remaining atoms leading to more efficient Raman pulses during the interferometer sequence.

The selection pulse only transfers atoms from the $|F = 2, m_F = 0\rangle$ magnetic sub-level due to a magnetic bias field which is applied directly after the molasses phase. The magnetic field shifts the energy levels of the non-zero magnetic sub-levels out of resonance of the Raman pulse and those atoms remain in the $|F = 2\rangle$ state. They are accelerated by a subsequent blow-away laser pulse resonant to the $|F = 2\rangle \rightarrow |F' = 3\rangle$ closed transition and are thereby removed from

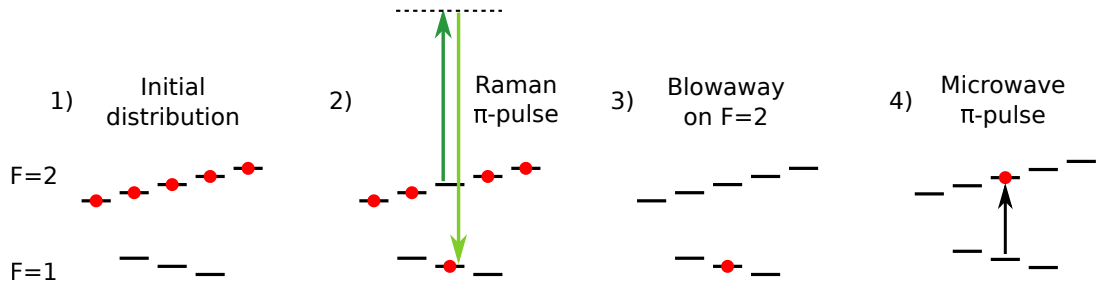

Figure 4.2.: Populated magnetic sub-levels of the internal atomic states $|F = 1\rangle$ and $|F = 2\rangle$ indicated by the red dots at four different stages of the selection process.

the selected cloud. Afterwards, a resonant microwave π pulse transfers the remaining atoms back to the $|F = 2, m_F = 0\rangle$ state followed by a blow-away pulse clearing the $|F = 1\rangle$ state. Thereby, atoms are removed which have been optically pumped to other magnetic sub-levels by the Raman pulse. The population of the atomic states and their magnetic sub-levels is visualized in Fig. 4.2.

In the end we have prepared an atomic cloud in the $|F = 2, m_F = 0\rangle$ state with a velocity distribution corresponding to $1.9\,\mu$K in both horizontal directions and to 13 nK in the vertical direction.

4.1.3. Interferometer phase

When the well-prepared atomic cloud enters the interferometer zone with the magnetic shielding the $\pi/2$-π-$\pi/2$ Raman sequence is applied. The pulses create a superposition of the two ground states with different velocities, re-direct the two spatially separated clouds after the time T and finally close the interferometer at $2T$ (see Sec. 2.2). They have a rectangular shape in time with typical pulse lengths of $20\,\mu$s ($\pi/2$ pulse) and $40\,\mu$s (π pulse) and are separated by $T = 260$ ms. Their short lengths in comparison to the velocity selection pulse makes them less velocity selective causing approximately the same transition probabilities for all atoms and ensure a high interferometer contrast. The intensities for the Raman master and Raman slave beam are 60 mW and 35 mW respectively with a beam diameter of 29.5 mm. In combination with the chosen Raman detuning of 700 MHz the AC Stark shift is canceled for the interferometer (see Sec. 2.3 and Sec. 5.6).

The central pulse is switched on a few milliseconds after the atoms reach the apex of their trajectory ensuring nearly equal long times for rise and fall inside the magnetic shield before and after the pulse. This allows a long time spacing between the pulses. At the same time a non-zero Doppler shift is present at the central pulse such that only one beam pair drives the atomic transition while the second is shifted out of resonance.

During the complete interferometer sequence the frequency difference between both Raman beams is chirped at a rate of $\alpha = d\omega/dt \approx 2\pi\times 25.1$ MHz/s to compensate for the Doppler shift of the atoms and keep the Raman pulses resonant to the hyperfine transition. In addition, the frequency of the Raman master laser is chirped at half this rate to keep the Raman detuning constant over time.

4.1.4. Detection

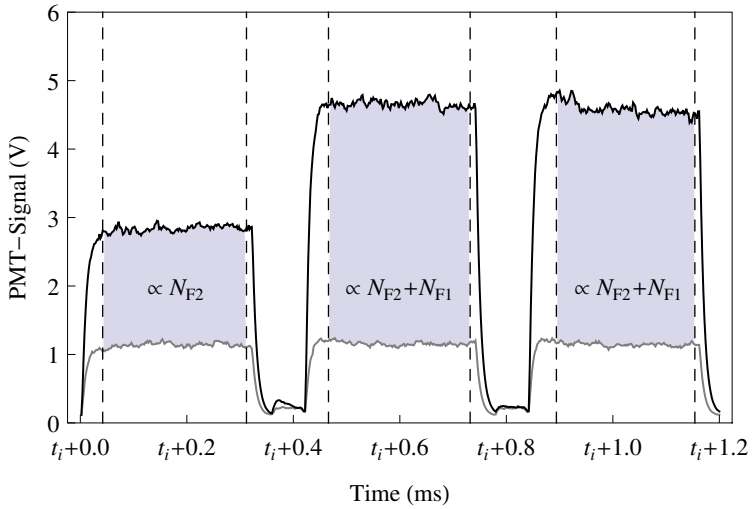

Figure 4.3.: Fluorescence signal of the atomic cloud observed by the PMT during the detection sequence starting at $t_i = t_{\mathrm{Detection}}$ (black curve). The background signal (gray curve) was detected using the same sequence at $t_i = t_{\mathrm{Background}}$ when the complete cloud had passed for the purpose of normalization. Three windows of equal length (dashed lines) exclude rising and falling slopes from further analysis. The marked areas are proportional to the number of atoms in $|F = 2\rangle$ and to the total number of atoms.

When the atoms reach the detection zone again at the time $t_{\mathrm{Detection}}$, they are subjected to a sequence of three resonant detection light pulses and their fluorescence light is collected by a photomultiplier tube (PMT). The detection pulses are slightly detuned to the red relative to the $|F = 2\rangle \rightarrow |F' = 3\rangle$ closed transition frequency and test for atoms in the $|F = 2\rangle$ state. Two intermediate repump pulses transfer atoms initially in the $|F = 1\rangle$ to the $|F = 2\rangle$ state. The complete sequence is repeated after the cloud has passed the detection zone at the time $t_{\mathrm{Background}}$ for the purpose of normalization. This time only stray light and fluorescence from background vapor is present. Both PMT signals, from detection and background detection, are shown in Fig. 4.3. The detected signals are segmented in three parts of equal length each covering one detection pulse but excluding the rising and falling slope of it. The areas inside the windows and between the two curves give the detected fluorescence light of the atomic cloud. The first area is proportional to the number of atoms in the $|F = 2\rangle$ state N_{F2} and the second and third areas to the total number of atoms $N_{F2} + N_{F1}$. The ratio between the areas of the first and second pulse then gives the relative fraction of atoms P_2 which were already in the $|F = 2\rangle$ state at the output of the interferometer

$$P_2 = \frac{N_{\mathrm{F2}}}{N_{\mathrm{F2}} + N_{\mathrm{F1}}} \tag{4.1}$$

The gravity value is then calculated from the transition probability $P = 1 - P_2$ applying Eq. (2.45). The ratio of the second and third pulses is used as a supplementary test to ver-

ify that the detection has been performed at the right instant when the cloud is at the height of the detection beam and that the flight curve of the cloud has not changed in height between runs.

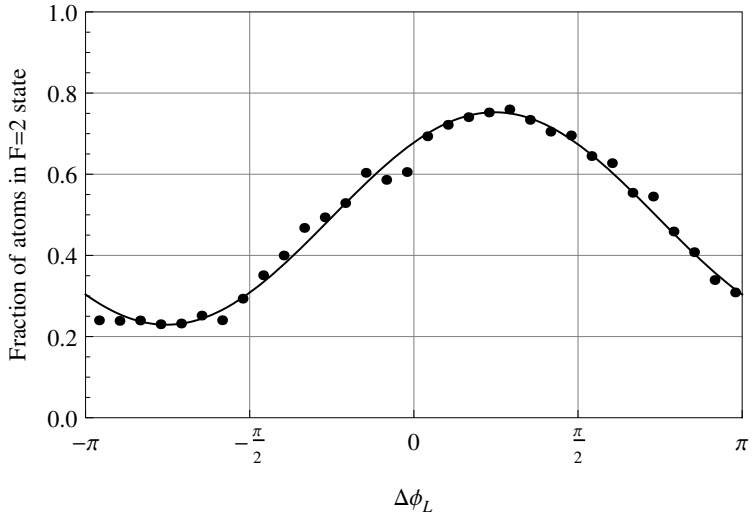

Figure 4.4.: Phase scan of the last Raman laser pulse $\Delta\phi_L$ of the atom interferometer measured at a pulse separation time T of 260 ms: The population of the $|F = 2\rangle$ state underlies a sinusoidal change. A mathematical fit (black curve) of the data points is used to extract the mean population, contrast, and phase of the fringe.

According to Eq. (2.45) a change of the interferometer phase causes a sinusoidal change of the population of the hyperfine ground states of the atoms. This relation can be observed by applying different phases for the last Raman laser pulse of the interferometer during subsequent interferometer runs. The resulting sinusoidal fringe is shown for a pulse separation of $T = 260$ ms in Fig. 4.4. The mean population, the contrast, and the phase of the fringe can be extracted from a mathematical fit which is plotted as a black line. It gives a fringe contrast (twice the amplitude of the cosine function) of 0.52 ± 0.02 and a phase of 773 ± 20 mrad for the position of the maximum.

The phase can now be calculated from each data point individually to increase the temporal resolution by keeping the former two parameters and the approximate position of the fringe maximum constant.

The processing, which extracts the phase and gravity information from the experimental parameters and the raw data obtained from the PMT and which is used for their analysis, has been realized with home-made software routines implemented with the computational program Mathematica [80]. A correct evaluation could be verified by comparing the resulting gravity values of early measurements to the ones of independent realizations, e.g. [65].

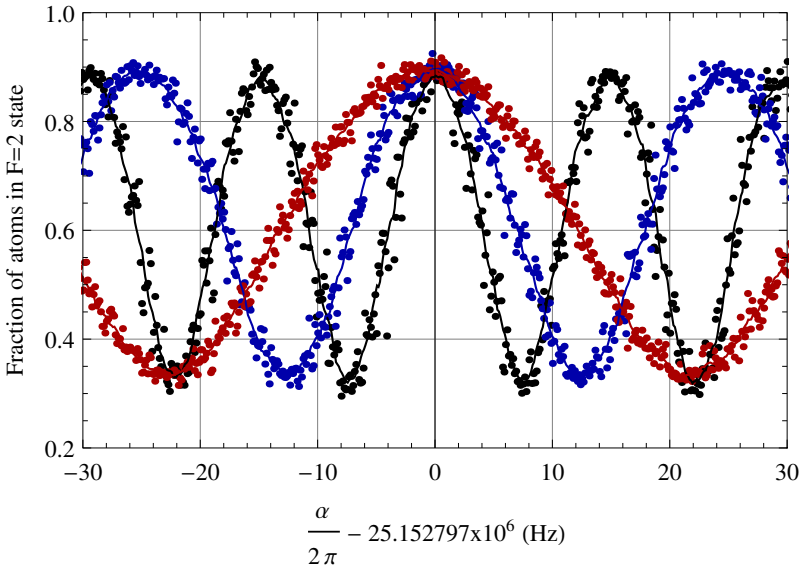

Figure 4.5.: Variation of the chirp rate α between subsequent interferometer runs taken at different pulse separations T of 150 (red), 200 (blue), and 260 ms (black points). The common maximum leads to the correct chirp rate. The solid lines show moving averages of the measured data for better clearness.

4.2. Gravity measurement protocol

Determination of the full phase information

The phase of the interferometer can only be determined modulo 2π from a single fringe pattern. Patterns obtained from different pulse separations of the interferometer T are analyzed in order to get the full phase information. For each pulse spacing the chirp rate of the Raman slave laser α is varied between consecutive runs to observe its effect on the relative state population of the atoms. According to Eq. (2.44) the phase of the interferometer is zero and the interferometer output becomes independent of T when the chirp rate exactly cancels with the product of the effective light vector and the gravity acceleration $\boldsymbol{k}_{\text{eff}}\boldsymbol{g}$.

Figure 4.5 shows the relative population of the $|F = 2\rangle$ state plotted against the applied chirp rate measured at $T = 150$, 200, and 260 ms. Only for the chirp rate of interest the state population is maximal during all configurations at the same chirp rate. In this case the maximum is at $\alpha = 2\pi \times 25.152\,797\,\text{MHz/s}$ and corresponds to an acceleration of $9.812\,628\,\text{m/s}^2$.

High-precision gravimeter

Once the correct chirp rate is determined with adequate precision, it is used to reduce the remaining interferometer phase to the interval $(-\pi, \pi)$ where it can unambiguously be calculated from the position of the fringe's maximum. Without any cancellation by the chirp rate the interferometer phase would reach almost 1×10^7 rad at $T = 260$ ms, which gives a phase response of $1.09\,\text{mrad}/(\text{nm/s}^2)$ for accelerations along the direction of the effective light vector. This gives

an operational range of $\pm 3.1\,\mu\mathrm{m/s^2}$ for the interferometer in this high-precision mode. As long as residual vibrations of the reference mirror or other influences do not cause changes larger than this number within a few experiment cycles it is possible to adjust the chirp rate in time and extract the full phase information. Under typical conditions the active vibration isolation system is able to keep the scatter between runs below $0.2\,\mu\mathrm{m/s^2}$ which allows for a good estimate of the interferometer phase in advance.

A series of measurements is typically started with a scan of the complete fringe during 32 single measurements to extract its mean population and contrast. Afterwards, the computer adjusts the laser phase of the last Raman pulse ϕ_L to test the population only on the slopes to the right and left of the maximum since they are most sensitive to phase changes. This scheme is followed for approximately 20 minutes while the laser phase is continuously adapted to track the centers of both slopes and therefore also the population maximum.

This scheme is applied to measurements with an effective light vector pointing upwards ($k_\uparrow$ configuration) as well as to measurements with an effective light vector pointing downwards ($k_\downarrow$ configuration). The direction of the light vector is reversed each run in order to measure systematic differences between both configurations with high temporal resolution (see Sec. 5.5). This adds up to 64 runs for the scans of the two fringes followed by measurements on the slopes in groups of four configurations:

1. $k_\uparrow$ “left slope” - 2. $k_\downarrow$ “left slope” - 3. $k_\uparrow$ “right slope” - 4. $k_\downarrow$ “right slope”

From each of the population measurements the position of the fringe maximum is calculated using the information of the mean population and contrast obtained from the corresponding fringe scan. Afterwards, the complete, extended scheme with fringe scans and slope measurements for $k_\uparrow$ and $k_\downarrow$ is repeated.

4.3. Gravity

The gravity acceleration $\boldsymbol{g}$ is calculated from the population using Eq. (2.45). The relative gravity course measured over a period of six days in December 2012 is shown in Fig. 4.6. Each data point represents the average value of all measurements taken within 15 minutes. The observed changes are due to the main tidal effect, which changes its amplitude and shape from day to day. The black line plotted behind the measured data points displays the tidal prediction including ocean loading which have been calculated with the software T-Soft [81]. The program is based on a theoretical model and uses a set of experimentally determined local parameters. The latter was provided by the Institut für Erdmessung (IfE) in Hanover and the Bundesamt für Kartographie und Geodäsie (BKG) and is attached in the Appendix A.

The variations have a magnitude of almost $2000\,\mathrm{nm/s^2}$ during the first day which is a relative change of 2×10^{-7} compared to the absolute gravity value.

Applied corrections

The basic tidal effect is the strongest temporal influence on gravity when the measurement is performed at a fixed location. In order to identify other effects originating either from environmental

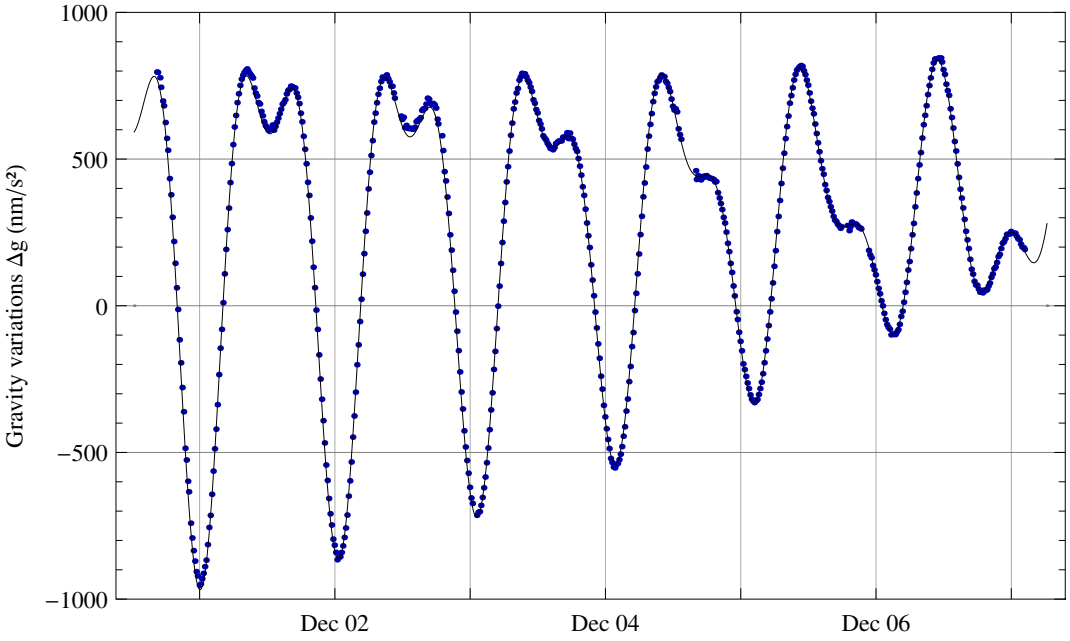

Figure 4.6.: Gravity variations measured by the GAIN atom interferometer. Each point represents the average value of all measurements taken within 15 minutes. The solid line shows a tidal prediction calculated using a theoretical model.

or instrumental influences, the tidal effect, ocean loading, polar motion, and atmospheric mass redistribution are subtracted from the measured signal (compare Sec. 1.1). Remaining residuals of the first measurements revealed variations at the order of several $10\,\mathrm{nm/s^2}$ over periods of a few hours up to one day. Their origins and efforts carried out for further improvement are discussed in the following chapter. Absolute gravity values are obtained by correcting the mean residual value also for the influence of the gravity gradient using Eq. (2.58).

5. Systematic effects

In this chapter, the influences of several systematic effects are discussed which had been identified as possible causes for drifts in early measurements. They include the alignment of the Raman laser beams (Sec. 5.2), where a new method has been developed, the stability and accuracy of frequency references (Sec. 5.3), and influences from the detection (Sec. 5.4). Methods implemented for their temporal stabilization and for the suppression or correction of possible offsets are introduced. It is shown that changes due to a reversed light vector are constant in time (Sec. 5.5) and that the AC-Stark shift has been canceled to a great extent (Sec. 5.6). The suppression of the Coriolis effect of the Earth has been realized by Christian Freier. It is presented in Sec. 5.1, since, for one thing, it is an important improvement and, for another thing, the hardware has been included in the tilt control. An overview of the different impacts on the gravity value and further effects discussed in other works is given in the last part of this chapter.

5.1. Coriolis effect of the Earth

Besides the phase contribution arising from accelerations there is another contribution occurring from the Coriolis effect of the Earth [29]. Earth's rotation in combination with a horizontal velocity of the atoms in East-West direction causes a systematic shift of the measured phase[1]. The resulting bias for the measured acceleration is

$$\Delta g_{\mathrm{Cor}} = 2\boldsymbol{\Omega}(\boldsymbol{v}_0 \times \hat{\boldsymbol{k}}_{\mathrm{eff}}) \tag{5.1}$$

where $\boldsymbol{\Omega}$ and $\boldsymbol{v}_0$ denote the rotation rate of the Earth and the mean velocity of the atomic cloud. $\hat{\boldsymbol{k}}_{\mathrm{eff}}$ is the pointing direction of the effective wave vector. Equation (5.1) can be simplified using the Earth's rotation rate of $73\,\mu$rad/s and the local latitude (52° for Berlin). This gives

$$\Delta g_{\mathrm{Cor}} \approx 2 \cdot 44\,\mu\mathrm{rad/s} \cdot v_{\mathrm{EW}} \tag{5.2}$$

where v_{EW} is the mean horizontal velocity of the cloud in east-west direction.

One way to avoid this bias would be to null the mean velocity v_{EW} for the detected atoms. However, the remaining velocity would have to be less than $60\,\mu$m/s in order to achieve the targeted accuracy of $5\,\mathrm{nm/s^2}$. This would correspond to a horizontal displacement between the initial MOT position and the final detection area of below $43\,\mu$m. This level of alignment is hard to achieve in the current experimental set-up.

[1] The centrifugal force, which also arises due to Earth's rotation, is in contrast included in the definition of gravity.

A second possibility to suppress the additional phase shift is to compensate the Raman beams for the rotation of the Earth. Therefore, the retro-reflecting reference mirror is mounted on a piezo driven tip-tilt platform (S-330 2SL by PI) rotating the mirror counterclockwise to the Earth's rotation rate during the interferometer sequence (similar to [82–84]). This way the phase shift is reduced and the alignment requirements relax to an acceptable level. The implementation into our experimental setup was done by Christian Freier.

The bias of the measured acceleration Δg_{Cor} was determined to $100\,\mathrm{nm/s^2}$ from two consecutive measurement series, one with enabled and one with disabled Coriolis compensation. This corresponds to a horizontal velocity v_{EW} of $\approx 1\,\mathrm{mm/s}$. The remaining uncertainty with enabled Coriolis compensation is dominated by the quality of the orientation of the tilt axis. Assuming an inaccuracy of less than 3° and similar mean velocities of the cloud in east-west and north-south direction, the uncertainty in g becomes smaller than $5\,\mathrm{nm/s^2}$.

5.2. Tilt

The direction of the effective Raman wave vector determines the measurement axis of the interferometer and its scalar product with the vertical unit vector can be read as a scaling factor of the instrument. It is reduced for tilted Raman beams and causes systematic drifts in the case of changing tilts.

In this experiment the tilts of the incoming and retro-reflected beams are controlled in two separate steps. In a first step, the tilt of the reference mirror is monitored and actively stabilized using a newly developed method. This results in a constant and maximized absolute value of the effective Raman wave vector in Eq. (5.4). In a second step, the pointing direction of $\boldsymbol{k}_{\mathrm{eff}}$ is ascertained and the vector aligned parallel to the vertical.

5.2.1. Alignment and active tilt stabilization of the reference mirror

For initial alignment of the reference mirror and the retro-reflected Raman beam an autocollimator setup is used. An additional beam splitter is inserted into the Raman beam path and directs 50 % of the incoming beam from the telescope on the top of the chamber to a another output. This second beam is retro-reflected by a hollow corner cube within an angle of less than $5\,\mu\mathrm{rad}$ (according to its specifications) and is then overlapped with the retro-reflected beam from the reference mirror, see Fig. 5.1a. Both beams are focused by a lens on a CCD camera chip at the remaining output of the beam splitter where their distance is minimized to align the reference mirror. This procedure allows for an accuracy of approximately $20\,\mu\mathrm{rad}$ to $50\,\mu\mathrm{rad}$, which almost meets the minimum requirement of $22\,\mu\mathrm{rad}$ for an accuracy of $\Delta g/g = 5 \times 10^{-10}$ for the atom interferometer.

A new method without additional optics in the beam path was developed for a better alignment clearly fulfilling the requirements. It also permits permanent monitoring and re-alignment while the interferometer measurements are in progress. The tip/tilt stage below the retro-reflecting mirror is utilized to scan both angles until the pre-aligned, retro-reflected beam is coupled back into the optical fiber, see Fig. 5.1b. Behind the fiber a PBS directs the beam, which has a linear polarization perpendicular to the initial beam, to a second output port where it is detected by

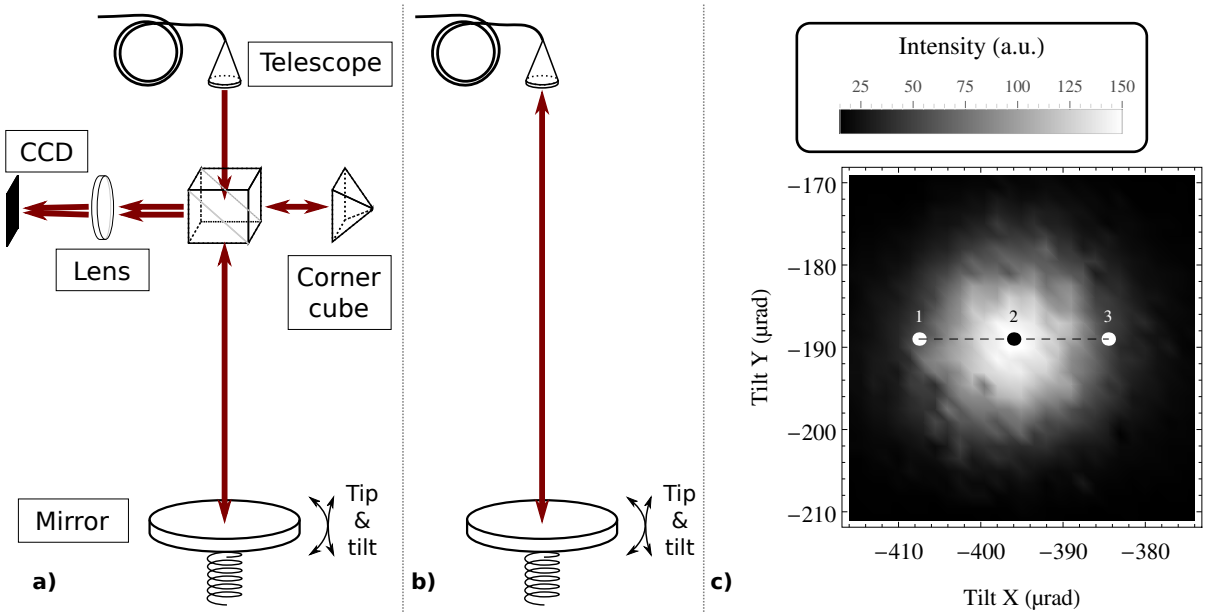

Figure 5.1.: Alignment of the reference mirror: a) initial alignment with beam splitter and corner cube. The two beams are focused on a CCD camera chip. b) coupling of the retro-reflecting beam back into the fiber and c) the corresponding signal of the photodiode situated behind the fiber during a scan of the mirror tilts. The three points indicate the tilt positions and photodiode signals of the three Raman pulses during the later interferometer sequence with enabled Coriolis compensation.

a photodiode (PD2 in Fig. 3.12 in Sec. 3.2.5). The resulting signal, displayed in Fig. 5.1c, has a FWHM of 17 μrad. In this method, in contrast to the method used for the pre-alignment, the position of the maximum does not suffer from systematic shifts arising from additional optics.

Once aligned, the signal of the photodiode is monitored during the three Raman pulses. The rotation of the mirror carried out for Coriolis suppression causes different signal strengths on the photodiode. While the middle pulse reaches maximum intensity, the first and third pulses have lower but equal intensities because of the tilt introduced by the rotating mirror. Any deviations from this relation indicate a change of the alignment. The mirror tilt in the perpendicular direction is observed during the MOT phase with three additional Raman pulses and a rotation of the reference mirror round the axis perpendicular to the one used before. The additional pulses are far off-resonant and no mutual influence between them and the MOT could be observed. The signals of the photodiode are used to control a slow feedback loop which compensates for tilt drifts arising, e.g., from the vibration isolation system.

5.2.2. Tilt and alignment of the Raman telescope

The pointing direction of the Raman telescope is likewise adjusted in two steps. In the first step, the autocollimator set-up from the initial alignment of the reference mirror is adapted. The mirror is replaced with a bin containing paraffin whose surface serves as a horizontal reference and retro-reflects part of the light beam. Both beam spots are then overlapped on the camera

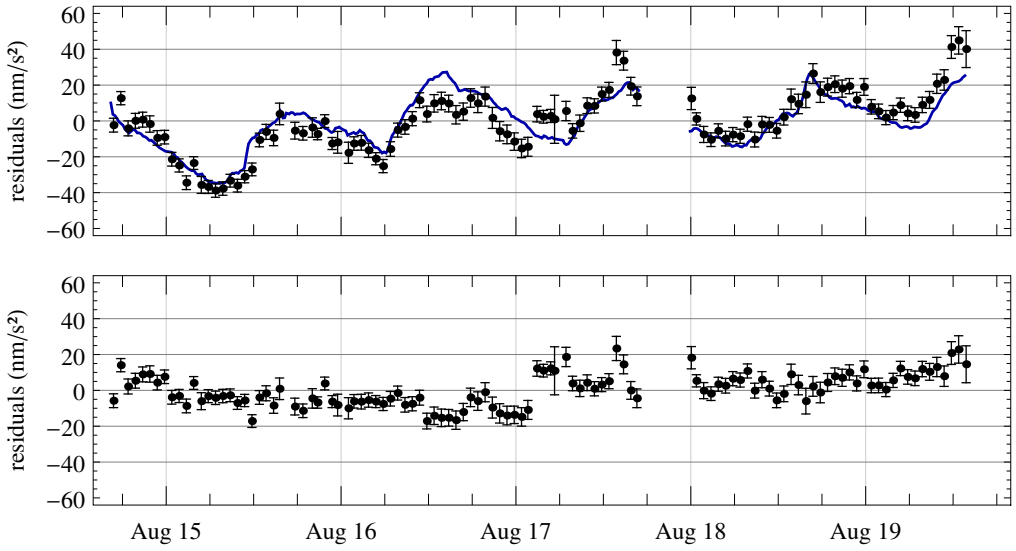

Figure 5.2.: Top: Residual gravity variations (black dots) observed during a time series of five days in August 2012 and the calculated influence from tilts (blue line). Bottom: Remaining variations after additional correction for tilt effects. Each data point is the mean value of one hour of measurement.

by tilting the telescope to the correct angle. The accuracy is limited by the additional optics and also by the accuracy of the liquid's surface influenced by the surface tension. An additional angle between the vertical and the beam inside the vacuum chamber is expected to be introduced by a wedge profile of the lower window of the chamber.

The limitations can be circumvented in a second alignment step. Therefore, the gravity value is measured at different tilts of the telescope and the results are evaluated using the following relation between the measured gravity values g_i and the appendant tilts.

$$g_i = g_0 \cos\left(\theta_{x,\text{offset}} + \theta_{x,i}\right) \times \cos\left(\theta_{y,\text{offset}} + \theta_{y,i}\right) \tag{5.3}$$

The tilts $\theta_{x,i}$ and $\theta_{y,i}$ are measured with two tilt meters[2] mounted directly to the telescope and pointing to orthogonal axes. $\theta_{x,\text{offset}}$ and $\theta_{y,\text{offset}}$ denote the initially unknown offsets of the tilt meters and g_0 is the gravity value in vertical direction. The offsets are determined by applying the method of least squares to a measurement series containing different tilts.

The top of Fig. 5.2 shows remaining variations of the measured gravity after the applied corrections described in the previous chapter. The blue line corresponds to variations calculated from the appendant tilt values and the tilt offsets determined from the series. The differences between measured and calculated values are shown at the bottom of Fig. 5.2. In order to shorten the time necessary for this procedure and to avoid possible influences from gravity variations caused by other effects, the beam can actively be tilted in several larger steps. Figure 5.3 shows

[2]Applied Geomechanics, 755-Series

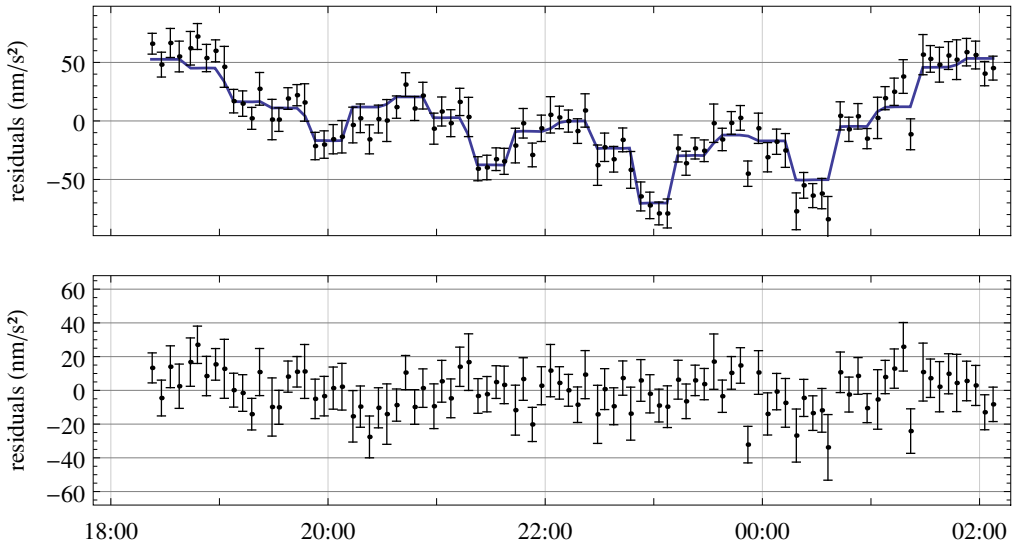

Figure 5.3.: Top: Stronger and more targeted tilt influences during a shorter period are observed when the Raman beam direction is actively tilted. Bottom: Remaining variations after correction. Each data point is the mean value of 5 min of measurement.

the variations obtained during the alignment procedure at a measurement campaign in October 2013. The influence of the single tilt steps are clearly visible. During the complete procedure the active tilt stabilization of the reference mirror ensured the correct alignment of the retro-reflected beam.

Once the tilt offsets $\theta_{x,\text{offset}}$ and $\theta_{y,\text{offset}}$ are determined, the gravity values already measured can be corrected with the help of Eq. (5.3) and the telescope is set to the correct tilt values for proper vertical alignment to decrease the effect of tilt drifts. The process has been repeated for several times during a measurement campaign lasting for two weeks. The obtained tilt offsets for the vertical direction revealed a remaining statistical uncertainty of only 5 μrad which is well below the requirements for the targeted accuracy.

5.3. Reference frequencies

The atom interferometer allows to relate accelerations very precisely to the absolute frequencies of the two Raman lasers f_1 and f_2 via Eq. (2.44) derived in the beginning. The frequencies determine the effective light vector

$$\boldsymbol{k}_{\text{eff}} = \boldsymbol{k}_1 + \boldsymbol{k}_2 = \frac{2\pi}{c}(f_1\hat{\boldsymbol{k}}_1 + f_2\hat{\boldsymbol{k}}_2) \tag{5.4}$$

where $\hat{\boldsymbol{k}}_1$ and $\hat{\boldsymbol{k}}_2$ denote the two unit vectors of the Raman beams and c the speed of light. Therefore, it is not only necessary to control the exact pointing of the light vectors, but also their absolute frequencies.

The Raman master frequency is stabilized by an electronic offset lock which adjusts the beat frequency between the master laser and a reference laser to a radio frequency generated by a DDS. For the Raman slave laser similar electronics control the offset relative to the Raman master laser. Consequently, the frequency of the reference laser and the frequency of the radio reference for the DDS both directly influence the two Raman laser frequencies and need to be tested for stability and absolute accuracy on the level of the desired relative atom interferometer accuracy of 5×10^{-10}.

5.3.1. Radio frequency reference

All radio frequencies used in the experiment are directly or indirectly generated from the 10 MHz and 100 MHz outputs of the frequency reference from Spectra Dynamics which is based on a Blue Top quartz working at 5 MHz. Its impact on the Raman laser phase noise was already examined during a former thesis by Malte Schmidt [66] and found to be below $10\,\mathrm{nm/s^2}$ for $T = 230\,\mathrm{ms}$ and $\tau > 5\,\mu\mathrm{s}$. Its absolute frequency is compared to a 10 MHz signal of a GPS receiver or to another frequency standard. It is adjusted to the correct absolute frequency by manual control before a measurement campaign or alternatively, if the frequency noise of the standard is low enough, permanently by an included electronic phase lock.

5.3.2. Frequency of the reference laser

The reference laser is stabilized to 40 MHz below the ^{85}Rb D_2 $|F = 3\rangle \rightarrow |F' = 4\rangle$ transition. The stabilization is achieved with the help of a Doppler free spectroscopy (see Sec. 3.2). The offset is due to the frequency shift of an AOM inside the optical setup.

A relative frequency accuracy of better than 5×10^{-10} implies an absolute accuracy of the laser frequency of better than 200 kHz which is more than one order of magnitude smaller than the natural line width of the optical transition (6 MHz). At this level deviations due to, e.g., electronics, cannot be completely excluded in the current setup. In order to determine the actual absolute frequencies of the reference and so of the Raman lasers and their stability over time, a series of additional spectroscopy measurements has been performed at the atomic cloud inside the vacuum chamber.

Using the experimental sequence described in Sec. 4.1 a cloud of ^{87}Rb is trapped, cooled, and launched. After the selection process only a single pulse with one laser resonant to the ^{87}Rb $|F = 2\rangle \rightarrow |F' = 1\rangle$ transition is applied instead of the Raman interferometer pulses. The mirror below the chamber still retro-reflects the beam. The pulse optically pumps part of the atoms initially in the $|F = 2\rangle$ state to the $|F = 1\rangle$ state. Finally, the relative population is measured as described before. During the pump pulse the second laser of the Raman laser pair is tuned far off from any resonance or blocked to prevent any influence. The transfer efficiency of the pump pulse is tested at different frequencies during consecutive iterations to determine the resonance frequency.

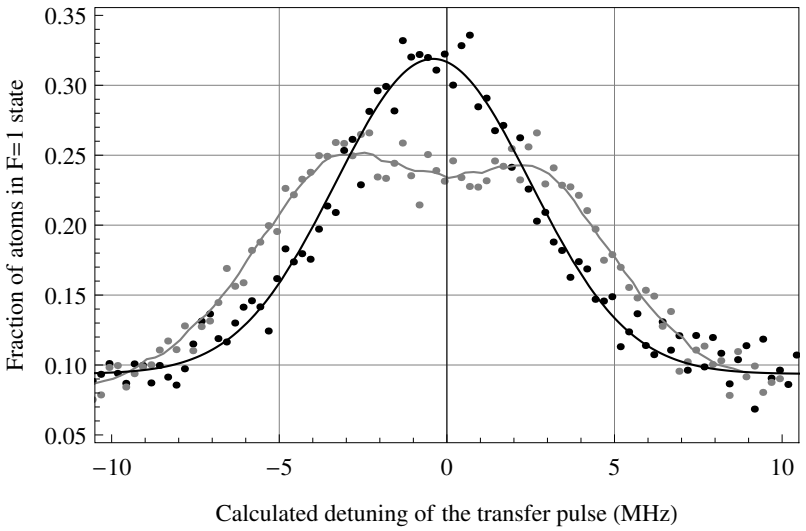

Figure 5.4.: Spectroscopy of cold atoms at the apex of the atomic fountain (black dots) with Gaussian fit (black curve) and at a vertical velocity (gray dots) with a moving average (gray curve).

Figure 5.4 shows two series of measurements, one performed at the apex of the fountain with a vertical mean velocity of the atomic cloud of nearly zero (in black) and one performed further downwards but still inside the magnetic shield with a vertical mean velocity of the cloud of 2.3 m/s (in gray). The difference between the frequency of the pump laser pulse and the expected resonance (for a perfectly accurate reference laser) is listed on the x-axis. The center of the signal obtained from the scan at the apex is shifted by -0.41 ± 0.06 MHz which is also the deviation of the reference laser from its nominal value. Shifts of the optical transition are not expected at this level due to the well-controlled environment inside the vacuum chamber with its magnetic shield and the preparation of the atoms in the $|m_F = 0\rangle$ internal state.

The width of the spectroscopy signal is 6.85 ± 0.07 MHz and hence only slightly above the natural linewidth of the transition. The very narrow vertical velocity distribution of the atomic cloud, which equals to a temperature of only 13 nK after the velocity selection process, reduces Doppler broadening to below 50 kHz. The second series of measurement (in gray) has a reduced maximal population in $|F = 1\rangle$ and a wider resonance. The atomic cloud which is moving downwards observes a frequency of the laser pump pulse which is shifted to the red for the light coming from the top of the chamber and shifted to the blue for the retro-reflected light. As a result, two resonances with lower height occur which are equally shifted to opposite sides by the Doppler effect.

The observed shift of the reference laser causes an offset of $-10 \pm 1\,\mathrm{nm/s^2}$ for the gravity measurements.

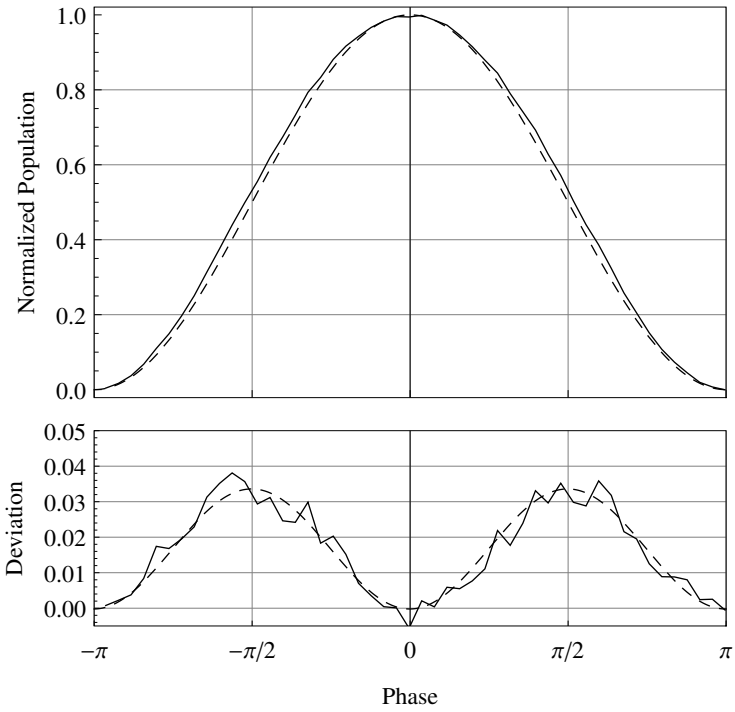

Figure 5.5.: Influence of the detection. Top: The detected, normalized signal (solid line) slightly differs from the expected signal (dashed line), especially on the slopes. Bottom: The deviation (solid line) resembles a sinusoidal curve oscillating at twice the phase (dashed line).

5.4. Detection

5.4.1. Shape of the detected fringe

The output of the atom interferometer gives a sinusoidal change of the relative population of the $|F = 2\rangle$ hyperfine state of the atoms. After the last interferometer pulse, atoms in the two different states still have different momenta because of the coupling of their inner state and their external momentum. Consequently, they slowly move apart. In our configuration the distance between the centers of the two clouds amounts to about 0.4 mm when they reach the detection zone and the direction of the photon recoil $\hat{\boldsymbol{k}}_{\text{eff}}$ determines which atomic state enters first. A second, even larger, displacement occurs because the clouds keep falling during detection. In order to collect a reasonable amount of light the detection pulses are separated by about 0.4 ms. During this time the clouds fall a distance of 1.4 mm.

The displacements of the clouds cause slightly different detection efficiencies of the light scattered by the atoms. This effect can be observed when a single cloud is detected for a long time while passing the detection zone. The efficiency coefficient $\eta(d)$ decreases in a good approximation symmetrically and exponentially for vertical displacements d above and below the center

of the detection zone. This is due to detection light with a non-uniform intensity profile and a non-perfect projection of the fluorescence light on the PMT. In our detection scheme the consecutive pulses are applied via the same telescope and thus at the same height. The falling cloud causes changes of the coefficient during the detection process and thereby slightly distorts the observed relative population P_2 of the $|F = 2\rangle$ state. The effect becomes apparent when $\eta(d)$ is included into the calculation of P_2 (see Sec. 4.1.4). Hence, the observed relative population becomes

$$P_2 = \frac{\eta(d_1)N_{\mathrm{F2}}}{\eta(d_2)N_{\mathrm{F2}} + \eta(d_2 + d_{\Delta\mathrm{F}})N_{\mathrm{F1}}}. \tag{5.5}$$

Here, d_1 and d_2 denote the mean displacements of the center of the $|F = 2\rangle$ cloud during the first and second detection pulse and $d_{\Delta\mathrm{F}}$ the displacement between the two hyperfine states populated with the number of N_{F2} and N_{F1} atoms.

As a consequence of a non-constant coefficient the fringe obtained from a phase scan is slightly deformed. Its slopes are either lowered or elevated because the denominator changes with the population ratio. Nevertheless, the positions of its maximum and minimum stay the same.

Figure 5.5 shows the average of more than 600 fringe scans each normalized to full contrast and each center shifted to zero phase. Its slopes are symmetrically elevated around the maximum above the expected population drawn as a dashed line. Its deviation, shown in the lower figure, is a sinusoidal curve oscillating at twice the interferometer phase. Here, the dashed line shows a mathematical fit.

The systematic deformation of the fringe has consequences for the analysis of the interferometer output signal, when the expected fringe shape is used to calculate the phase of the single measurements. It introduces systematic offsets to the calculated phases which are maximal in the middle of the slopes and whose signs differ for the right and left hand side of the maximum. In addition, the amplitude of the deformation depends on the exact timing of the detection pulses. Thereby systematic errors are introduced into the single measurements which reach a maximum of $\pm 70\,\mathrm{nm/s^2}$ on the center of the slopes for the deformation shown here for an interferometer pulse separation of T =260 ms. As a consequence, the effect increases the scatter of a set of measurements (when taken at different phases). Secondly, the resulting mean phase for the fringe's maximum obtained from a data set depends on the distribution of the measured values on the fringe. There is no shift for a set which is symmetrically distributed around the maximum, while any imbalance causes an offset.

The additional scattering introduced by this effect is below the single shot sensitivity of typically $150\,\mathrm{nm/s^2}$ per shot and can be further reduced by applying a correction to the detection signal before calculating the interferometer phases. The effect is also visible in the ASD of the gravity data where the four different measurement configurations, including opposite fringe slopes and Raman light vectors, cause a spike at a quarter of the experiment's repetition rate (see also the ASD of the gravity data from one of the comparison campaigns which is shown in Fig. 6.7 in Chapter 6). During this work a symmetric tracking of the fringe's maximum during the measurements and a correction for the deviations in the analysis has been used. The remaining systematic phase error is expected to be well below the targeted absolute accuracy of $5\,\mathrm{nm/s^2}$.

5.4.2. Arrival time of the atomic cloud

The arrival time of the atomic cloud at the detection zone mainly depends on two initial starting parameters: the vertical position of the prepared atoms and their vertical velocity component. Temporal changes of the gravity value, e.g., due to tides, are too small to notably influence this quantity. While the velocity is selected directly after the launch of the atomic cloud and determined via precise frequencies, the initial position is among others dependent on the MOT beam intensities and the magnetic fields. Small variations therefore can affect the cloud's trajectory and the effective measurement height.

The second and third detection signals both detect the fluorescence of all atoms. Their ratio can be analyzed to gain further information in this context. It changes with the vertical position of the atomic cloud at the moment of the detection or in other words with the arrival time of the cloud. Measurements reveal an approximately linear relation in our setup between the ratio of the signals and a time displacement of the detection sequence within the range of $\pm 1\,\mathrm{ms}$. During gravity measurements the mean variations typically correspond to displacements of less than 0.2 ms for the arrival time on time scales of several hours. This is equivalent to vertical shifts of the MOT position and the cloud's trajectory of only 0.7 mm. The resulting variations of the measured gravity due to the gravity gradient of $3080\,\mathrm{nm/s^2/m}$ are well below the targeted absolute accuracy.

5.5. Reversed Raman light vector

There are several systematic effects which are independent of the pointing direction of the Raman light vector $\hat{\boldsymbol{k}}_{\mathrm{eff}}$, which means that the induced phase shift $\Delta\Phi_{\mathrm{indep}}$ does not change its sign when the light vector is reversed. They include phase shifts arising from second order Zeeman shifts, residual AC Stark shifts, and a non-linear frequency ramp due to electronics [29, 30, 85]. In order to separate their influence from the one of the dependent effects the total interferometer phase can be written as

$$\Phi_{\uparrow/\downarrow} = \pm\left(|\boldsymbol{k}_{\mathrm{eff}}\boldsymbol{g}|T^2 + \Delta\Phi_{\mathrm{grad}} \pm \Delta\Phi_{\mathrm{rec}} + \Delta\Phi_{\mathrm{dep}}\right) + \Delta\Phi_{\mathrm{indep}} \tag{5.6}$$

where the arrows indicate the pointing direction, up or down, of the light vector and $\Delta\Phi_{\mathrm{dep}}$ denotes the influence of other, dependent effects. $\Delta\Phi_{\mathrm{rec}}$ is a phase contribution arising from the slightly different trajectories of the atomic cloud due to the reversed recoil in combination with the gravity gradient (see Sec. 2.2.4). For $T = 0.26\,\mathrm{s}$ the center of mass of the cloud is on average 3 mm lower during the interferometer sequence when the photon recoil is pointing downwards compared to a recoil pointing upwards. This results in a slightly stronger gravity acceleration due to the gravity gradient and the calculation gives $\Delta\Phi_{\mathrm{rec}} = -5\,\mathrm{mrad}$. Further influences of the gravity gradient are summarized in $\Delta\Phi_{\mathrm{grad}}$. The influence of the recoil and the independent effects cancel out in the half difference $\bar{\Phi}$ of the two configurations

$$\bar{\Phi} = \frac{\Phi_{\uparrow} - \Phi_{\downarrow}}{2} = |\boldsymbol{k}_{\mathrm{eff}}\boldsymbol{g}|T^2 + \Delta\Phi_{\mathrm{grad}} + \Delta\Phi_{\mathrm{dep}}. \tag{5.7}$$

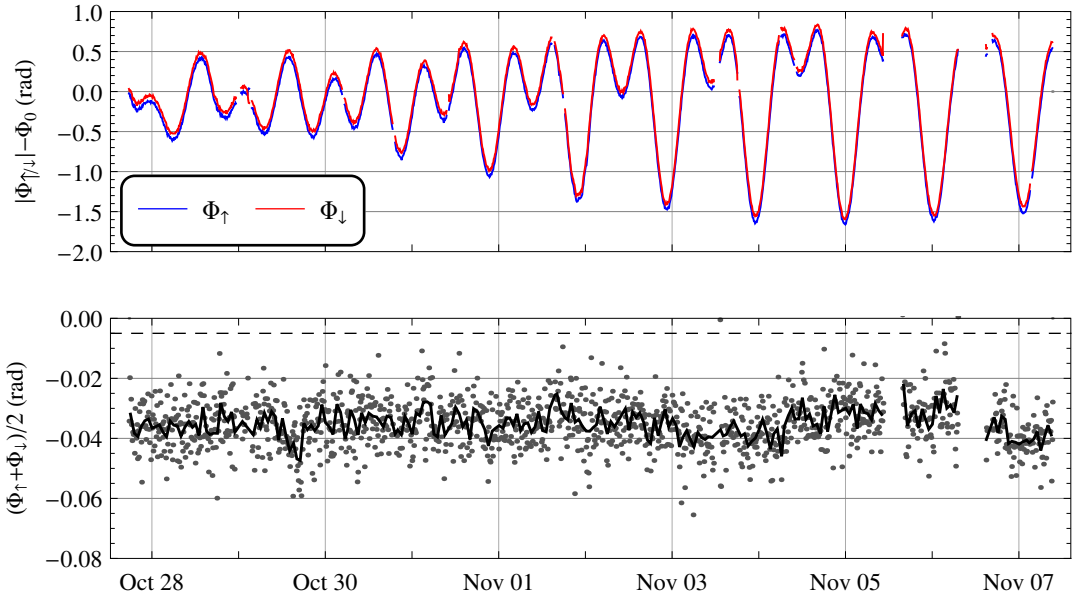

Figure 5.6.: Influence of reversing the wave vector $\boldsymbol{k}_{\text{eff}}$ and thereby the transferred photon recoil on the interferometer phase. Top: The absolute phase values for the $\Phi_\uparrow$- (in blue) and $\Phi_\downarrow$-configurations (in red) both show the tidal signal each with a small offset (bins of 10 min, $\Phi_0 = 1.068\,457\,2 \times 10^7$ rad). Bottom: Half sum $(\Phi_\uparrow + \Phi_\downarrow)/2$ of the configurations for bins of 10 min (gray) and 60 min (black). The dashed line indicates the calculated phase contribution $\Delta\Phi_{\text{rec}}$.

In contrast to the half difference, the half sum solely includes the influence of the recoil and the independent effects but excludes the acceleration and the dependent effects.

$$\frac{\Phi_\uparrow + \Phi_\downarrow}{2} = \Delta\Phi_{\text{rec}} + \Delta\Phi_{\text{indep}} \tag{5.8}$$

Its value could be significantly stabilized and reduced in our atom interferometer setup by applying the correct intensity ratio for the Raman beams and with the upgrade to the improved laser system. The absolute values of the interferometer phases for both wave vector configurations, subtracted by a constant $\Phi_0 = 1.068\,457\,2 \times 10^7$ rad, are shown in the upper part of Fig. 5.6. For each configuration the measurements are time-averaged over intervals of 10 min. The lower part shows the half sum of both phases time-averaged over intervals of 10 min and 60 min as gray dots and a black curve. The dashed line indicates the calculated effect of the photon recoil in combination with the gravity gradient. There is no global drift and the mean value is −35 mrad. Subtracting $\Delta\Phi_{\text{rec}}$ gives $\Delta\Phi_{\text{indep}} = -30$ mrad corresponding to -2.8×10^{-9} g with a standard deviation of $\sigma_{\text{indep}} = 4$ mrad for the time average of 60 min corresponding to 0.4×10^{-9} g.

The observed stability of the independent effects excludes an influence on long-term recordings of relative gravity changes at a sufficient level also for potential, non-perfect cancellation of the half difference $\bar{\Phi}$. In contrast, the latter aspect might still cause a systematic offset to the absolute gravity value which will be subject to future studies. The stability of the independent

effects is also an improvement if compared to other works. Louchet-Chauvet et al. [30] found a minimum temporal deviation of 0.8×10^{-9} g around integration times of 2×10^3 s to 4×10^3 s for the half sum which increased again for longer integration times. In another work by Peters et al. [29] values corresponding to a relative half sum of $\approx 4 \times 10^{-9}$ and $\approx 7 \times 10^{-9}$ are shown for two different instants of the interferometer Raman π pulse while other parameters such as T and τ are kept constant. They are equally spaced before and after the atomic cloud reaches the apex. It would also be of interest to test the additional configurations with the GAIN sensor. This was not realized because of an existing influence of the switched MOT coils on the vibration isolator. A shift of the timing of the interferometer pulses relative to the coil switching causes a changing offset and has to be postponed after the installation of a magnetic shield.

At the time of this measurement in October 2013 all improvements made during this work had been implemented. Other aspects of this data are discussed in Sec. 6.3.

5.6. AC-Stark shift

The Raman laser beams can cause phase shifts in the interferometer due the AC-Stark shifts of the hyperfine levels, see Sec. 2.3. In order to estimate their influence an additional Raman test pulse, which is slightly off-resonant to the transition ($\delta = 6.6\,\mathrm{MHz}$), has been included between the first and second interferometer pulse. The measured interferometer phase has been compared between runs with and without enabled test pulse. It has been measured for detunings of the virtual level Δ between $-0.2\,\mathrm{GHz}$ to $-1.8\,\mathrm{GHz}$ and for three different ratios of the Raman Master and Slave optical powers: $40\,\mathrm{mW} : 40\,\mathrm{mW}$ ($= 1:1$), $60\,\mathrm{mW} : 31.6\,\mathrm{mW}$ ($\approx 1.9:1$) and $54.2\,\mathrm{mW} : 31.6\,\mathrm{mW}$ ($\approx 1.72:1$).

The necessary pulse lengths of the three regular interferometer pulses have been determined in advance and been adapted for each of the combinations. They yielded $11\,\mu\mathrm{s}$ to $90\,\mu\mathrm{s}$ for the π pulse with linearly increasing values for larger detuning Δ and were also slightly dependent on the chosen intensities. This behavior reflects the dependence of the effective Rabi frequency on the detuning found in Eq. (2.19). A linear fit to the data gives

$$\tau_\pi = \begin{cases} 42\,\mu\mathrm{s/GHz} \cdot |\Delta| & ,60\,\mathrm{mW} : 31.6\,\mathrm{mW}\ ,\ 54.2\,\mathrm{mW} : 31.6\,\mathrm{mW} \\ 51\,\mu\mathrm{s/GHz} \cdot |\Delta| & ,40\,\mathrm{mW} : 40\,\mathrm{mW} \end{cases} \tag{5.9}$$

The measured phase shifts introduced by the test pulses have been normalized by the pulse lengths τ_{TP} of either $20\,\mu\mathrm{s}$ or $30\,\mu\mathrm{s}$. It is shown for different combinations of the Raman intensity ratio and the detuning of the virtual level Δ in Fig. 5.7. An intensity ratio of $1:1$ (black data points) causes a strong offset per pulse length of $40\,\mathrm{mrad}/\mu\mathrm{s}$ and more in the interferometer outcome. Considering the required length of a $\pi/2$ pulse this results in offsets of the order of $10^3\,\mathrm{mrad}$ ($\approx 10^3\,\mathrm{nm/s^2}$ for $T = 260\,\mathrm{ms}$). For a ratio of $1.9:1$ (red data points) the shifts are much lower and there exist two detunings with zero shift. The smallest influence over a wide detuning range has been observed for a ratio of $1.72:1$ (blue data points). The solid lines represent the theoretical influence of the AC-Stark shift $A\,\delta^{\mathrm{AC}}(\Delta, \Omega_{\mathrm{eff}})$, compare Eq. (2.66), where the constant A is included as a conversion factor between the AC-Stark shift and its influence on the atom interferometer phase. It has been fitted to the data for each intensity

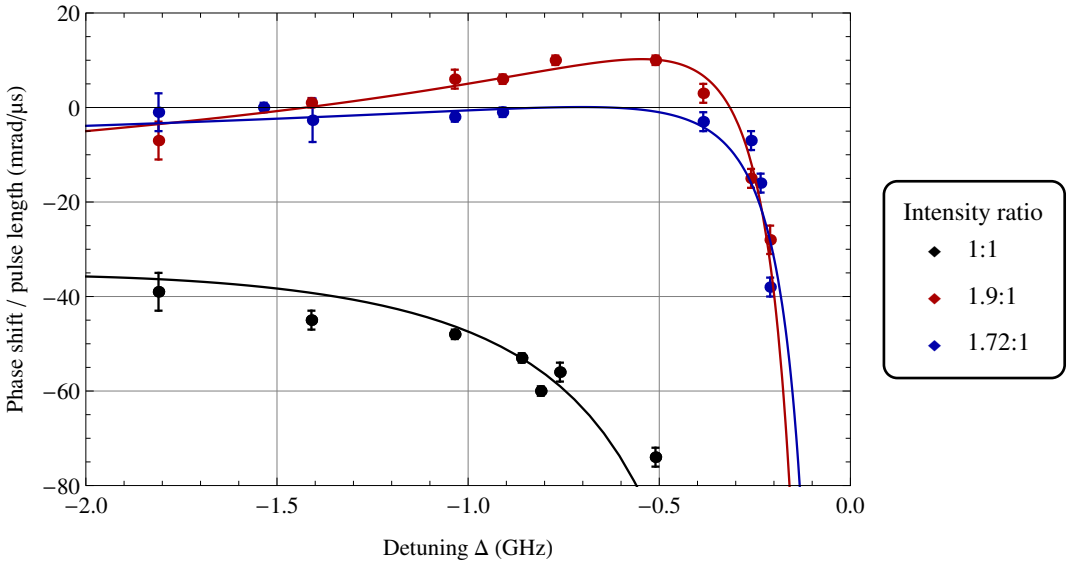

Figure 5.7.: Influence of a non-resonant Raman test pulse on the interferometer phase depending on its detuning Δ and intensity ratio between Master and Slave beam. The values are normalized to a pulse of 1 μs length. The intensity ratio 1.72 : 1 (in blue) shows minimal influence over a wide frequency range and for a ratio of 1.9 : 1 two detunings with zero shift appear. Pulses with a ratio of 1 : 1 cause much stronger phase shifts (in black). The values are in good agreement with the fitted model from theory (solid lines).

ratio. For the calculation the effective Rabi frequencies have been estimated from the condition $\Omega_{\text{eff}}\tau_\pi = \pi$ and the required pulse lengths given by Eq. (5.9). The measured values are in good agreement with this model.

In this measurement the violation of the interferometer symmetry excludes any cancellation of the effect. During gravity measurements at least a partial suppression can be expected via the terms $(\theta_1^0 - \theta_3^0)$ which are included in Eq. (2.37) and represent the effect during the first and last pulse. The measured data can be used for a coarse estimate of the effect in the regular interferometer. At a detuning of $\Delta = -0.7\,\text{GHz}$, which was used during the gravity measurements, the difference between the influences for the ratios 1.72 : 1 and 1.9 : 1 yields $\approx 10\,\text{mrad}/\mu\text{s}$ and a $\pi/2$ pulse has a length of 15 μs. Assuming that the total laser powers are correct to within 0.2 mW and that the effect is approximately linear with the ratio in this regime, this gives a shift of below 10 mrad for the interferometer phase. The effect will even be further suppressed by the symmetry of the sequence. During long-term measurements the stability is ensured by the Raman intensity stabilization, see Sec. 3.2.5. If a lower remaining uncertainty of the absolute offset is required, the suppression factor could be determined by measuring the influence of a test pulse near the last Raman pulse and comparing both results. For a different detuning Δ the changing interferometer pulse lengths have to be considered and that varying intensity ratios also shift the positions of zero influence, see Fig. 2.8.

Systematic effect	typical effect [nm/s^2]	remaining uncertainty after suppression [nm/s^2]
AC Stark shift	1000	< 10
Coriolis effect	100	5
Vertical alignment	50	< 0.3
Wave front distortions	(50)	(50)
Magnetic fields from MOT coils	(50)	(50)
Non-perfect detection	20	< 5
Self attraction (from [65])	19	1
Reference laser offset	10	1

Table 5.1.: Overview of systematic effects ordered by their strengths.

5.7. Overview of systematic effects

Table 5.1 summarizes systematic effects, their typical order of magnitude, and their remaining uncertainty in our current setup. The largest shifts have been observed without cancellation of the AC Stark shift, when equal Raman beam intensities were used instead of the correct ratio, and without Coriolis compensation. Besides the ones already discussed three more effects are listed. Self attraction of the instrument, which is induced by the mass distribution of our vacuum chamber, has been calculated in another work [65]. It increases the measured value by $19 \pm 1\,\mathrm{nm/s^2}$. The other two effects listed arise from pulsed MOT coils and from wave front distortions of the Raman laser beams. They are still under investigation and given numbers are meant as first estimates. Therefore, they cause the largest remaining uncertainties.

The MOT coils are switched on and off at a fixed time during each measurement. Hence, they can influence the vibration isolation stage and potentially also the seismometer. An additional magnetic shielding will be installed around the MOT zone in the near future to avoid this effect.

Wave front distortions of the Raman laser beams arise from imperfect optics and deformation of the windows due to the vacuum. In combination with the remaining horizontal velocities of the atoms they cause slightly different Raman phases at different Raman pulses. Primary simulations and measurements performed for this instrument [86, 87] and measurements by other groups [30] show that wave front distortions induce offsets and uncertainties presumably at the order of $50\,\mathrm{nm/s^2}$.

6. Gravity comparison campaigns

Several aspects of the GAIN instrument were tested during the course of overall three comparison campaigns. Each of them was performed together with another state-of-the-art classical gravimeter, including the mechanical spring gravimeter gPhone-98, the freely falling corner-cube gravimeter FG5X-220, and the superconducting gravimeter SG-30. The sensitivity under different vibrational conditions was compared to the classical instruments and the relative precision and stability was analyzed over the course of several days. In addition, a preliminary absolute value of the GAIN sensor was compared to the one obtained with the absolute gravimeter FG5X and in another comparison to the one transferred by the superconducting gravimeter. During all three campaigns the measurements with the atom interferometer were carried out in close collaboration with Vladimir Schkolnik and Christian Freier.

The first comparison was performed with the original version of the GAIN laser system (see Sec. 3.2) and for the second comparison the modifications were only partly completed. For the last campaign, the laser setup was finished and the intensity stabilization for the Raman beams could be applied for the first time. As a consequence the reliability, especially for long-term observations, was clearly increased. A second important aspect of the third campaign is the quality of the gravity data we could compare our results with. The superconducting gravimeter had a much lower intrinsic noise than the other two gravimeter types and was operated at an optimal location with a low seismic background. For this reason, the measurements of the last campaign allowed to analyze additional aspects and is discussed in greater detail than the first and second one.

The improvements achieved in mobility of the atom interferometer during this time are illustrated at the end of this chapter.

6.1. Comparison with the gPhone

The first parallel comparison measurement was performed together with the gPhone-98 in our laboratory in Berlin-Adlershof in December, 2012. The latter is a mechanical spring-type gravimeter build for relative gravity recordings (see Sec. 1.3). It allows for operation at most different locations including field use and measurements on the second floor of a building as in the present case. The instrument was operated by the Institut für Erdmessung (IfE) about two meters away from the GAIN sensor. It had already been installed several weeks prior to the comparison in order to let the spring settle down until initial run-in effects had decayed for the most part.

The upper part of Fig. 6.1 shows a selection of the gravity changes recorded by the atom interferometer and the theoretical prediction, which includes tidal effects and ocean loading. The middle and lower figure display the gravity signals of the GAIN instrument and the gPhone

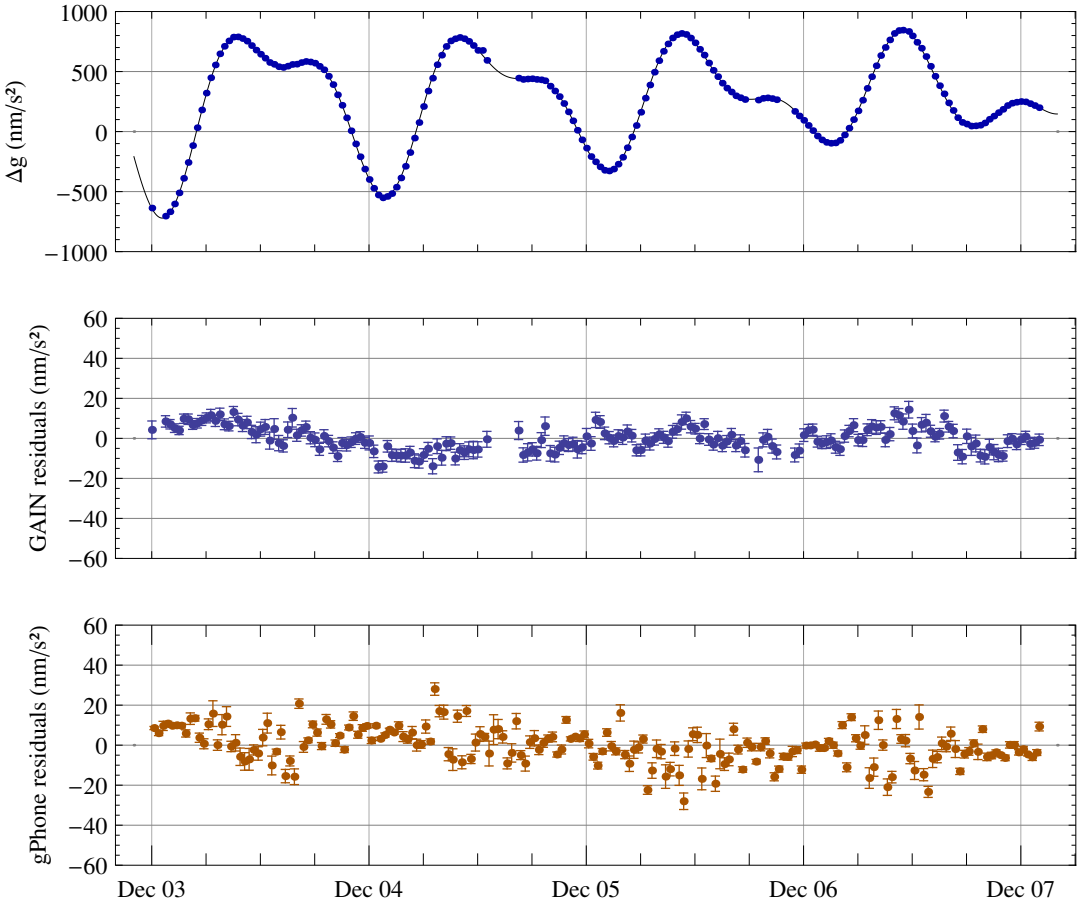

Figure 6.1.: Top: Signal of the atom interferometer (blue dots) and theoretical prediction (black solid line). The middle and lower figure show the residuals of the GAIN and gPhone-98 sensors. The residuals of the gPhone have been corrected for a linear drift of 102 nm/s^2 per day. Each point is the average of all measurements taken within 30 min.

after applying corrections for tidal effects, ocean loading, and atmospheric mass variations as described in Sec. 4.3. In addition, the data taken by the gPhone has been corrected for a linear drift of 102 nm/s^2 per day which had been extracted from the data by the IfE [88]. Each point is the average of all measurements taken within 30 min. The remaining measured variations are below 20 nm/s^2 for both time series which gives a mutual agreement at the lower 10^{-9} g level. A direct comparison between both series reveals different trends on a daily timescale indicating instrumental influences instead of small gravity variations not covered by the models. In the case of the atom interferometer they might be due to intensity fluctuations of the Raman beams which were not automatically stabilized during this measurement.

One apparent difference between the signals of the two instruments is the quality of their noise and their dependence on the time of the day. The effect is also shown in Fig. 6.2 with a higher temporal resolution of 1 sample/min on December 4. The residuals of the gPhone, in the lower

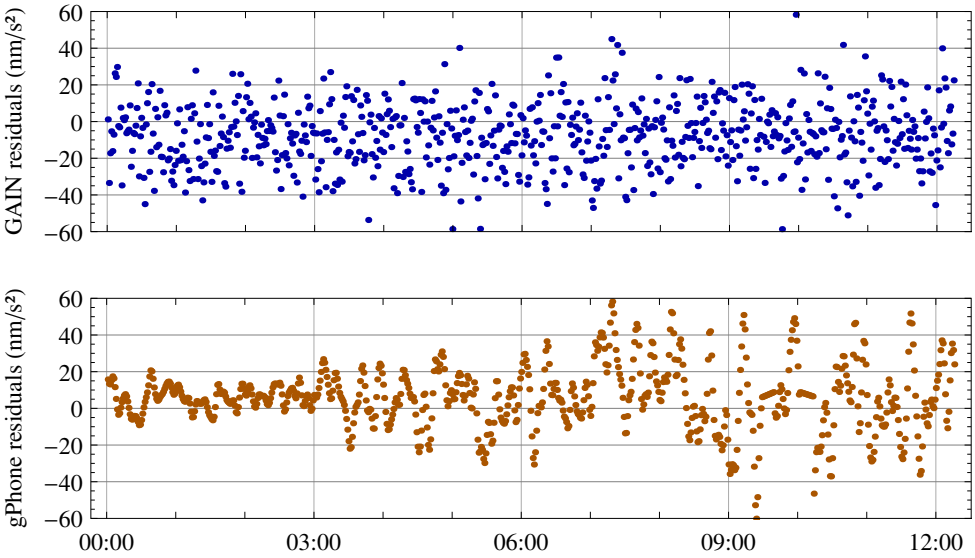

Figure 6.2.: Detail of the gravity residuals measured on December 4. Top: Atom interferometer, each point represents the average value of all measurements taken within 1 min. Bottom: Residuals from the gPhone are influenced by the increasing vibrational noise level in the building. Here, data was recorded with 1 sample/min.

figure, shows small variations at timescales of about 10 min and amplitudes of 20 nm/s^2 during the night. They significantly increase after 3 am[1]. The noise level further increases and reaches its maximum around 9 am. The effect is also measured by an additional seismometer sensing an increasing vibrational noise level inside the building during the day. The first increase coincides with the start of operation of the suburban train which is only 0.6 km away at 4 am local time. The signal of the GAIN sensor reveals a scatter which is in the beginning three times larger than the variations present in the signal of the gPhone. In contrast, it remains almost constant during the day. The increasing variations of the gPhone signal are practically not visible and do rarely influence the longer averaged signal in Fig. 6.1.

The residuals of the atom interferometer in Fig. 6.2 are in a good approximation normally distributed and have a standard deviation of 18 nm/s^2. This statistics also applies to the data when only averaged over two consecutive measurements, $k_\uparrow$- and $k_\downarrow$-configuration, with a duration of $t = 3$ s and a standard deviation of 80 nm/s^2. The values follow the $1/\sqrt{t}$ relation for uncorrelated noise and give a sensitivity of 113 nm/s^2/shot or 139 nm/s^2/$\sqrt{\text{Hz}}$.

Apart from the qualitative differences and the strong, global drift of the gPhone which is already corrected here, the mean amplitudes of the scatter and of the residual variations during day time have a comparable level.

[1] All times stamps used in the figures are given in coordinated universal time (UTC). The local winter time is one hour ahead of it.

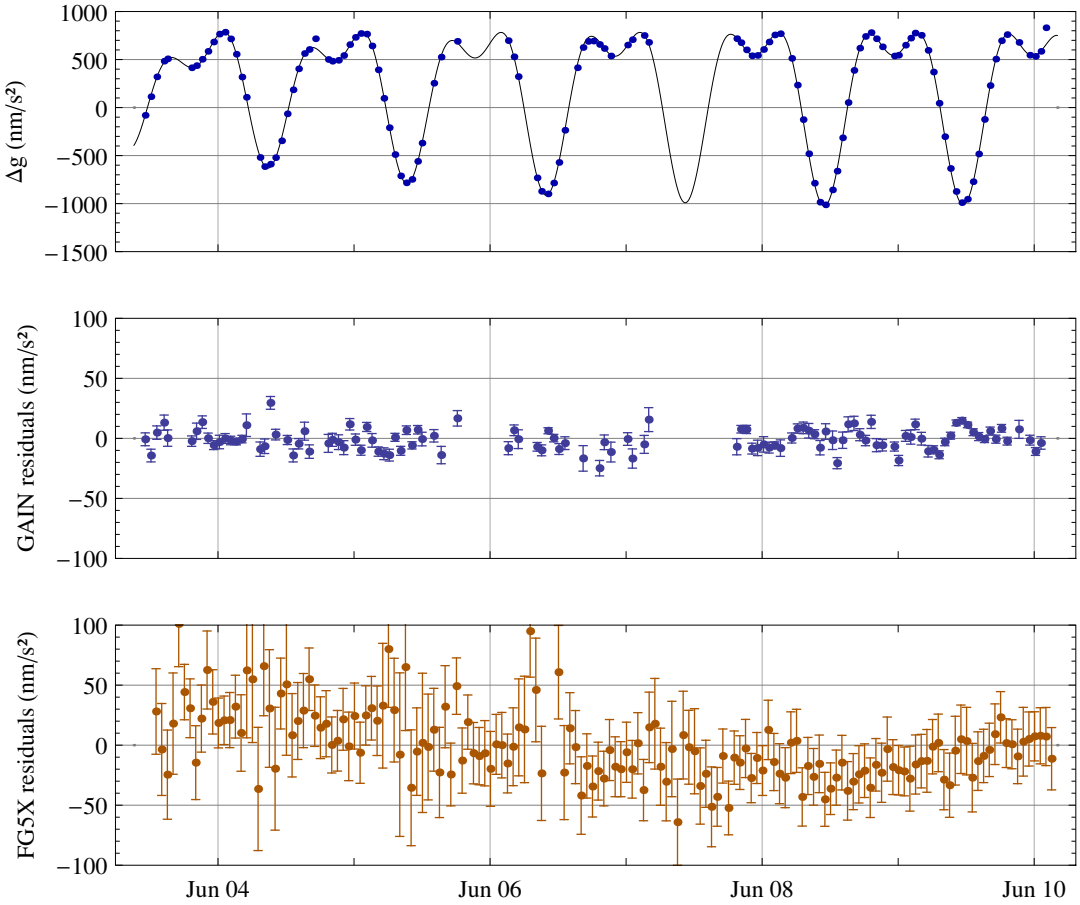

Figure 6.3.: Top: Signal of the atom interferometer (blue dots) and theoretical prediction (black solid line). The middle and lower figure show the residuals of the GAIN and FG5X-220 sensors. Each point represents all measurement within 1 hour.

6.2. Comparison with the FG5X

Another campaign was performed together with the absolute gravimeter FG5X-220 even though not all systematic effects of the atom interferometer had been characterized at the targeted accuracy level. The opportunity still was taken in order to compare the preliminary absolute gravity value of the GAIN sensor with the absolute value of the well established FG5X and to analyze their differences in the context of the expected uncertainties. The measurements were taken in June, 2013 in our mechanical workshop which is situated on the first floor of our physics building. There, an absolute gravity reference point had already been established for this purpose by the BKG in 2010 [89].

The FG5X-220 was operated by the IfE on top of the reference point and the atom interferometer was installed about 2 m next to it. The former performed 50 free fall experiments (drops) each hour with drop intervals of 10 s which are combined in one measurement set. During the

Instrument	Date	Gravity value (nm/s^2)	Comment
FG5-101	Sept, 2010	9 812 641 390 ± 30	measured by BKG [89]
GAIN	Dec, 2010	9 812 641 650	transferred from next room
FG5X-220	June, 2013	9 812 641 436 ± 23	measured by IfE [90]
GAIN	June, 2013	9 812 641 742	transferred from different height

Table 6.1.: Gravity values measured at 1.25 m above the reference point in our physics building in Berlin-Adlershof. Values obtained with the GAIN instrument are transferred using gradients and connections from [89].

remaining time the instrument was idle in order to keep wear and tear low and increase the life-time of the instrument. The atom interferometer was operated at its standard repetition rate of 0.7 Hz. After parallel registration for a period of 3 days the FG5X was removed and the atom interferometer was moved to the reference point and once again run for a few days.

The gravity time series of the atom interferometer and the residuals of both instruments are shown in Fig. 6.3. The residuals include corrections for tidal effects, ocean loading, and atmospheric mass variations. Each data point represents the average value of all measurements taken within 60 min which corresponds to the length of one set for the FG5X. The residuals of the FG5X reveal different qualities of their scatter on the individual days. On the weekend, from June 8, and during the nights it is much lower than during daytime of the working days. The standard deviations double from 14 nm/s^2 on June 8 to 29 nm/s^2 on June 5. For the GAIN sensor they yield 9 nm/s^2 for both days. On shorter time scales, e.g., in the early morning of June 8, standard variations of about 3.6 nm/s^2 corresponding to 176 nm/s^2 per single shot are reached. Another difference between the two sensors are trends visible in their signals. The residuals of the FG5X decrease from the 4th to the 8th at the order of ≈ 50 nm/s^2 in total. Afterwards, they partly return during the last day. This drift is not present in the signal of the atom interferometer. On the other hand, smaller features measured by the latter which are at time scales of several hours cannot clearly be identified in the FG5X signal, e.g., on June 9.

The effective measurement height of the atom interferometer when operated on the reference point was 1.388 m. Its absolute value has been transferred to a height of 1.25 m using the local gravity gradient of $-3.08\,\mu$m/s^2/m in order to compare it to the value of the FG5X. The gradient had been determined by the BKG when the reference point was installed. In Tab. 6.1 the absolute gravity values are listed. It also contains results which were obtained during previous measurements in 2010. One was performed by the BKG and another value was measured with the atom interferometer in a different room and then transferred (see [65, 66]). The differences between the absolute values of the GAIN sensor and the FG5/FG5X yield 260 nm/s^2 and 306 nm/s^2 in 2010 and 2013 respectively. The values measured in 2013 are a little higher compared to the ones in 2010 which might be due to new buildings constructed in the near neighborhood and new machines in the workshop.

Finally, it has to be emphasized that the remaining drifts and features all have very small amplitudes, at the order of a few 10^{-9} g, and that the location is not perfectly suited for such precise gravity measurements. In order to reach even better results it is necessary to use special, dedicated pillars which are decoupled from the buildings. This has been realized during a third

campaign which is presented in the following part.

6.3. Comparison with the superconducting gravimeter

Another comparison was performed in October, 2013 at the Geodetic observatory Wettzell which is situated in the South of Germany. The observatory is operated by the German Federal Agency for Cartography and Geodesy (BKG). At the station the superconducting gravimeter SG-30 is installed for permanent gravity registration and has already been characterized and calibrated in the course of regular comparisons with absolute gravimeters. The SG-30 is a dual sphere superconducting gravimeter including two measurement systems aligned on top of each other. They have much lower scatter and drift rates compared to mechanical spring-type gravimeters and offer also a higher temporal resolution than the laser interferometer absolute gravimeters. The SG-30 was installed in 2010 and its sensors have now, after initial run-in effects, almost linear drifts which are determined to only $-161.84 \pm 0.24\,\mathrm{nm/s^2}$ per year and $-54.03 \pm 0.24\,\mathrm{nm/s^2}$ per year for the lower and upper system respectively [91]. As a consequence its signal can be used for a more precise characterization of the atom interferometer.

In between the comparison campaigns the atom interferometer had been equipped with a complete new switching and distribution system for the MOT laser beams (see Sec. 3.2). It allows for continuous operation without re-alignment of the MOT system when operated at a fixed location even outside of optics laboratories with temperature variations of up to a few degree Celsius and possibly also at higher variations. It also drastically reduces efforts and the time required for re-installing at a new location after transportation. In addition, an automatic intensity stabilization system for the Raman laser beams was implemented. Both systems ensure stable operation conditions with very constant laser intensities on all optical fibers which are also monitored by integrated photodiodes.

After transportation from Berlin to Wettzell the atom interferometer was re-installed within a few days inside the gravimeter house. It was placed on a special pillar dedicated to gravimeter measurements which was decoupled from floor vibrations and only a few meters away from the superconducting gravimeter. A map of the gravimeter house can be found in the Appendix E.

6.3.1. Gravity recordings

The top figure in 6.4 shows the measured gravity variations recorded by the atom interferometer (blue dots) and by the lower sensor of the superconducting gravimeter (solid black line) over a period of 11 days. Both time series have been averaged over 10 min. In the middle figure the residuals of both signals are plotted after correction for tides, ocean loading, and atmospheric mass effects calculated by the theoretical models. Here, each data point is the average of all measurements taken by the atom interferometer within an interval of 60 min. Data from the lower sensor of the SG-30 is equally averaged and in addition corrected for the sensor's well-known linear drift. It is plotted as a solid black line. The lower figure shows the difference between both gravimeter signals. Error bars of the SG-30 are not displayed because they are below $0.1\,\mathrm{nm/s^2}$.

The time series of both instruments show almost the same course of the measured gravity

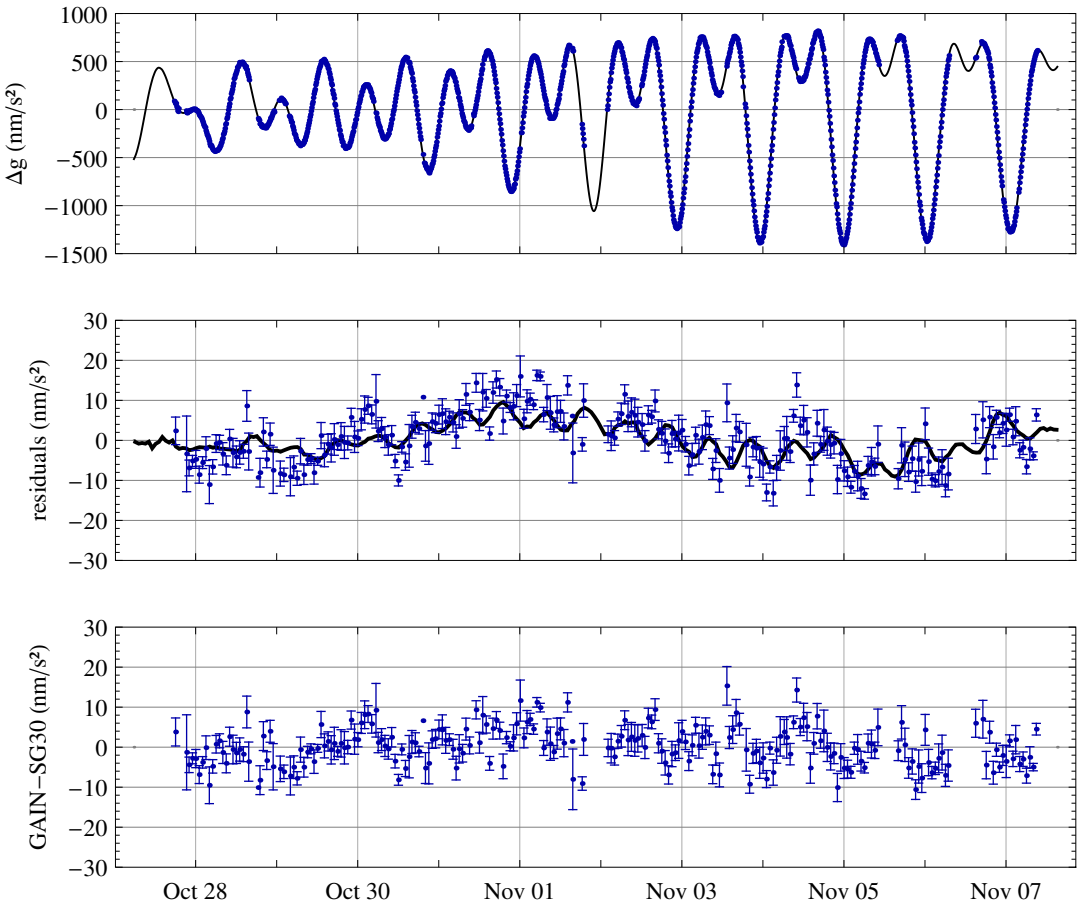

Figure 6.4.: Top: Gravity variations measured by the atom interferometer (blue dots) and the superconducting gravimeter (black solid line). Middle: residuals for both instruments after correction for tides, ocean loading, and atmospheric mass effects. Bottom: difference between both gravimeter signals.

variations which are mainly dominated by the basic tidal effect. Differences become only apparent in the residuals and the difference signal between the instruments. A slow oscillation with a period of approximately one week and a peak-to-peak value of about $10\,\mathrm{nm/s^2}$ can be identified in both signals. In contrast, semidiurnal oscillations with a slightly lower amplitude are only visible in the superconducting gravimeter signal. Both of these oscillations are probably due to marginally imperfect local parameters available for the tidal corrections [91]. Remaining variations in the difference signals are basically below $\pm 10\,\mathrm{nm/s^2}$.

6.3.2. Long-term stability

The long-term stability of the atom interferometer can be characterized by the Allan deviation of the corrected gravity signal. This two-sample deviation, which is often used to characterize

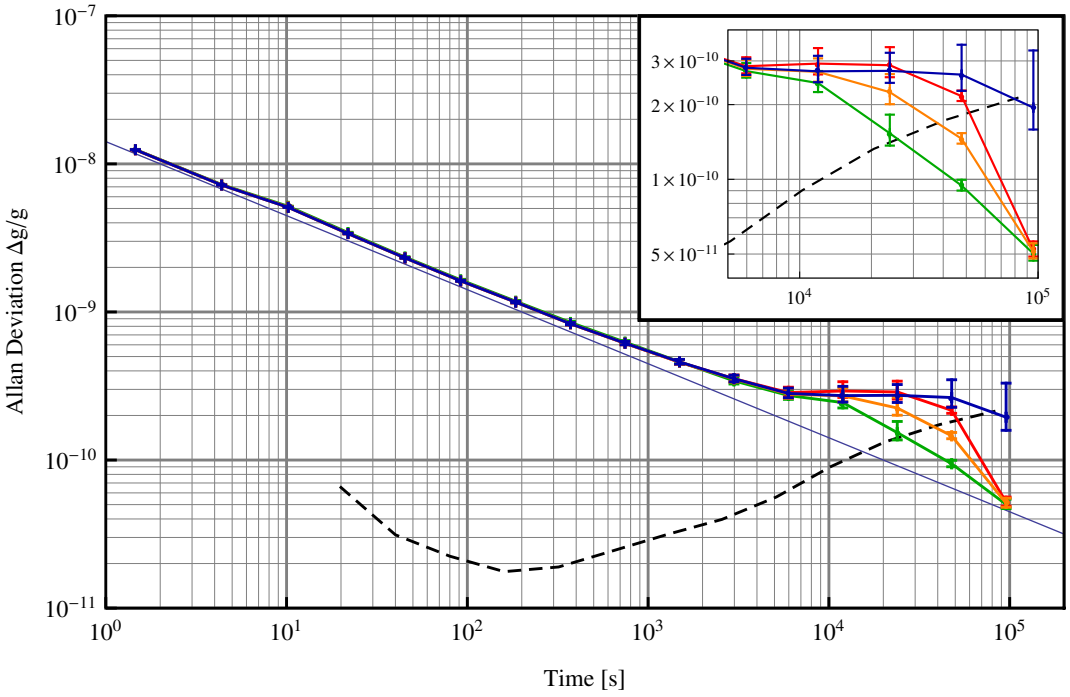

Figure 6.5.: Allan deviation: The blue solid line and the dashed black line show the Allan deviations of the residuals of the GAIN and the SG-30 sensors, respectively. The 3 additional, solid lines represent the Allan Deviation calculated for the difference signal between the two gravimeters without and with different corrections explained in the text. The thin, straight line indicates the expected slope in the case of perfect white noise. The inlet shows an enlarged detail.

the frequency stability of precise clocks, is defined as [92, 93]

$$\sigma_y(\tau) = \sqrt{\frac{1}{2}\langle(\bar{y}_{k+1} - \bar{y}_k)^2\rangle} \tag{6.1}$$

with the expected value of the normalized deviations $\bar{y}_k = \langle\frac{\Delta g}{g}\rangle_k$ within the kth time interval of length τ, see Appendix C.

For the calculation, only data taken after November 1 has been used, since during the first 4 days a daily oscillation of the room temperature with an amplitude of about 1 K has been observed. Including these days would result in a different behavior on this timescale ($\tau \approx 1 \times 10^5$ s) which is also the period of the daily tides and therefore important for the determination of the scaling factor of the superconducting gravimeter in the following. During the other days room temperature fluctuations could be slightly reduced and also showed a different temporal behavior.

In Fig. 6.5 the blue solid line and the dashed black line show the Allan deviations for the residuals of the atom interferometer and the superconducting gravimeter respectively when corrected with the help of the theoretical models introduced before. The Allan deviation for the atom interferometer decreases in the beginning almost with a slope of $\tau^{-1/2}$, which corresponds

Scaling factors (SF)	lower sensor	upper sensor
previous mean SF ($\mathrm{nm/s^2/V}$)	-739.0 ± 1.1	-678.4 ± 1.0
SF from this campaign ($\mathrm{nm/s^2/V}$)	-740.4 ± 0.3	-680.6 ± 0.3

Table 6.2.: Previous and newly determined scaling factors for the SG-30 sensors.

to white noise (indicated by a thin linear slope in the figure). For times longer than 6×10^3 s (≈ 1.5 hours), its value stays almost constant and only slightly decreases to lower values at 1×10^5 s (more than one day). The dashed slope for the SG-30 is calculated to estimate the reliability of the theoretical models at different timescales. Its rising for times longer than 200 s is due to the fact that the models do not cover all environmental influences affecting the gravity value. A drift of the SG-30 is not expected to be the reason because of former characterizations of the instrument. This is also supported by the Allan deviation for the difference signal between both instruments (red line). For observation periods longer than 5×10^4 s, the signals of the atom interferometer coincides to a higher extent with the superconducting gravimeter than with the models.

The two additional curves are obtained when two corrections, an improved scaling factor for the SG-30 and a time delay for the atom interferometer, are fitted and applied to the data. The yellow curve includes the correction for the SG-30, the green curve includes both corrections. Motivations and implementations are described in the following.

6.3.3. Scaling factor of the SG-30

Superconducting gravimeters levitate a superconducting sphere with the help of magnetic fields. They compensate changing forces with a feed-back loop on the current and the latter gives their output signal (see Sec. 1.3.2). In order to convert the values into accelerations it is necessary to do a precise calibration and work out the scaling factor of the instrument. The factor has to be determined by analyzing the influences of known gravity changes on the superconducting gravimeter which typically allow for an accuracy of about 0.1 % [47, 48].

The scaling factors for the two sensors of the SG-30 had been determined during former comparisons with different absolute gravimeters. The mean values yield $-739.0 \pm 1.1\,\mathrm{nm/s^2/V}$ and $-678.4 \pm 1.0\,\mathrm{nm/s^2/V}$ for the lower and upper sensor, respectively. However, the values might be improved by further campaigns [91].

In the analysis of the current data we therefore used the large signal of the tidal effect during the last five days of the measurement to improve the agreement between the time series of both gravimeters by applying a fit of the scaling factor to the data. A linear regression gives slightly increased factors of $-740.4 \pm 0.3\,\mathrm{nm/s^2/V}$ and $-680.6 \pm 0.3\,\mathrm{nm/s^2/V}$. The new scaling factor improves the Allan deviation of the difference signal between both instruments at the expected timescale of about half a day, see yellow curve in Fig. 6.5. Their uncertainties are below 0.05 %. The previous and new scaling factors are summarized in Table 6.2.

6.3.4. Time delay

The tidal signals of the superconducting gravimeter are affected by a constant time delay due to its anti-aliasing filter and its electronics [13]. For the SG-30 this delay amounts to approximately 13 s [91]. For the atom interferometer no significant time delay τ is expected since the delay introduced by the vibration isolator becomes negligible at the tidal frequencies (see Sec. 3.1.2) which have dominating amplitudes at semi-diurnal and diurnal tides. In order to verify the expected relation, the correlation coefficient $R[\tau]$, which is a measure of linear dependence between two signals, has been used.

$$R[\tau] = \frac{\frac{1}{N}\sum_{i=1}^{N}(g_{\mathrm{gain}}[t_i] - \bar{g}_{\mathrm{gain}})(g_{\mathrm{sg30}}[t_i + \tau] - \bar{g}_{\mathrm{sg30}})}{\sigma_{\mathrm{gain}}\sigma_{\mathrm{sg30}}} \tag{6.2}$$

Here, t_i denotes the discrete times of the single measurements taken by the atom interferometer and σ_{gain} and $\bar{g}_{\mathrm{gain}}$ are the standard deviation and mean value of the corresponding data set. Gravity data from the SG-30 has already been filtered by an analog anti-aliasing filter included in the instrument before it has been sampled and allows for interpolation. Hence, corresponding values for all times t_i and for arbitrary time delays between both instruments can be calculated.

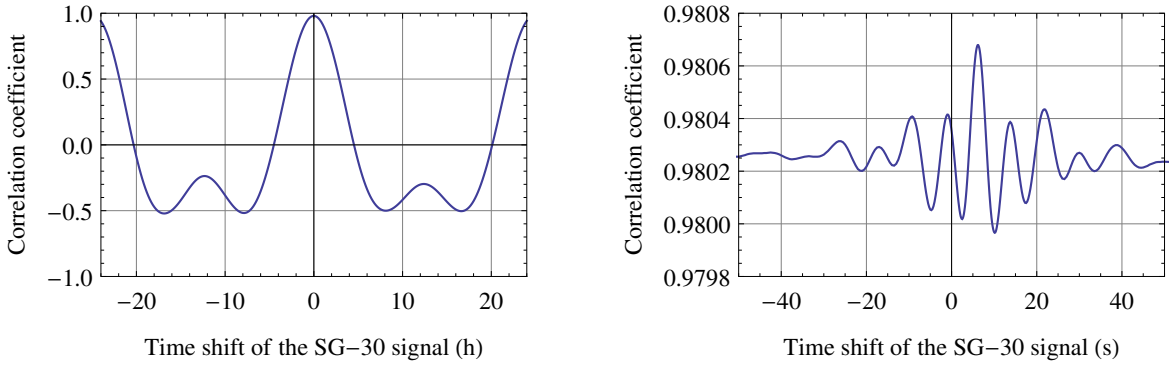

Figure 6.6.: Correlation coefficient between the GAIN and SG-30 signals. Left: Coarse time shifts from several hours up to one day reveal the self-similarity of the tidal effect. Medium shifts around the center allow for the calculation of time delay at low frequencies (see text). Right: Fine shifts of a few seconds show a very small oscillation near the center. Note the very different scales on both axes of the two figures.

The correlation coefficient in Fig. 6.6 shows different features for small and large time shifts. On a coarse time scale the correlation function reflects the self-similarity of the dominating tidal effect. It starts at 0.98 around zero shift showing the linear correlation and decreases to both directions to below −0.6 for shifts of approximately six hours. Another strong maximum is reached near ±24 hours. Around its maximum the coefficients shape can be approximated by a parabola. A mathematical fit to points within ±10 min from the maximum reveals its central position at -20 ± 2 s. This means that the signals of the atom interferometer are delayed by 20 s relative to the SG-30 lower sensor at these low frequencies with periods of several hours and

Time delay of	relative to	for microseism	for tidal signals
GAIN	SG-30	−6 s	+20 s
SG-30	Seismometer	+6 s	-

Table 6.3.: Relative time delays between sensors. A positive value indicates a time lag of the instrument in the first column relative to the one in the second column.

longer. A correction of the atom interferometer's signal for this delay results in an even more improved Allan deviation between 1×10^4 s to 1×10^5 s and therefore supports the outcome. The result does not depend, within the stated errors, on the order of the determination of the scaling factor and this time delay. The Allan deviation including both corrections is shown as a green curve in Fig. 6.5. The relative delay plus the time delay of the SG-30 of 13 s gives a total delay of 33 s for the GAIN sensor.

A second feature of the correlation coefficient can be observed on a smaller time scale ($\tau <$ 1 min), where the parabola is almost flat. The coefficient shows a very small oscillation with a period of approximately 7.5 s and a decaying amplitude for increasing time shifts. The corresponding frequency for this period is about 0.13 Hz and can also be found in the ASD of the superconducting gravimeter, see Fig. 6.7. It is part of the microseism of the Earth and thus influences both instruments although it is barely visible in the signal of the atom interferometer due to its larger noise and the suppression of the vibration isolator. The maximum correlation value for this oscillation is reached for a time shift of 6 s implying a (longer) delay for the superconducting gravimeter at this frequency. The oscillation enhances by a factor of 30 when the correlation coefficient is calculated for gravity data taken on November 1 when a stronger microseism background was present. It has a peak to peak amplitude of almost 0.02 and a period of 8.5 s which corresponds to a frequency of 0.12 Hz. Its maximum value again indicates a delay of 6 s for the SG-30 sensor. The increased strength and changed period on this day can also be seen in the ASD. An analog analysis has been performed using the signals of an additional seismometer, CMG-40 from Guralp, which was operated on the same pillar as the atom interferometer. Its internal bandwidth only allows to measure microseism and not tidal signals. The data of the CMG-40 have been low pass filtered with a discrete Bessel filter (fifth order, cutoff-frequency of 1 Hz) for the analysis. The delay of the SG-30 relative to the CMG-40 yields 6 s. The time delays of the seismometer and the applied filter have been estimated from the manufacturer's data and from simulation respectively. Their sum is ≈ 0.5 s. Time delays for frequencies around the resonance of the vibration isolator are expected to be strongly frequency dependent and would need a more detailed analysis of this sub-component. However, there are no signals present in this regime which reach amplitudes above the instrumental noise of the atom interferometer, see ASD in Fig. 6.7. The relative delays are listed in Table 6.3.

The stronger time delay of the SG-30 for the microseism can be explained when the delays of the individual instruments are considered. Data from the SG-30 is processed by a strong low pass filter with a cutoff frequency near the microseism. A value of several seconds and below the delay of 13 s for tidal signals seems reasonable. In the case of the atom interferometer the frequencies are clearly above the resonance of the active vibration isolator such that a negligible influence is expected. The relative delay between SG-30 and CMG-40 is consistent. In contrast,

the total time delay of 33 s for the atom interferometer is contradictory to the expectations. A contribution of the vibration isolator is again expected to be negligible (see Sec.3.1.2). One possible explanation might be the influence of the detection and the deformation of the fringe (see Sec. 5.4). During the measurements a slow tracking of the fringe's maximum with a time constant of around 15 minutes has been used. As a consequence the tested phases on the right and left slope have not been perfectly symmetric to the maximum when gravity changed at large rates as in the case of tidal influences. The observed influence at $\approx 2 \times 10^{-10}$ g in the Allan deviation corresponds to about 3 % of the maximal effect when measured on a single slope. Therefore, the deformation might simulate such a delay. For the future, a better detection with more homogeneous projection optics minimizing the deviation and a faster tracking should easily reduce this influence.

6.3.5. Amplitude spectral densities

Different signal and noise components of the two sensors can be analyzed with the help of their amplitude spectral density (ASD). Figure 6.7 shows the ASD[2] for gravity variations observed on two days with different microseismic background. This time the data also includes the tidal signals to demonstrate at which frequencies the signals and the instrumental noise are dominating. Solid and dashed lines show the ASD for November 4 and 1, respectively. The ASD of the atom interferometer signal shows an almost constant noise level corresponding to white noise at approximately $2 \times 10^{-7}\,\mathrm{ms}^{-2}\mathrm{Hz}^{-1/2}$ over several frequency decades. This behavior agrees with the observed slope of the Allan deviation in Sec. 6.3.2. The ASD increases for both instruments below 2×10^{-3} s due to tidal variations, which are still included in the analyzed time signals, and cause a broad maximum for times around one day. It has a slightly different shape on the two days but looks the same for both instruments at each measurement period. The peak at 0.17 Hz is situated at a quarter of the experiment's repetition rate and is not included in the spectral density of the SG-30. It is caused by the 4 different measurement configurations of the experiment including changes between Raman light vectors and slopes of the fringe. Using an extended model for the fringe pattern obtained from the detection (see Sec. 5.4), its original amplitude could be slightly reduced.

The spectrum of the SG-30 signal in general shows a lower noise level. It includes two broader peaks around 0.06 Hz and 0.13 Hz which belong to the microseismic background of the Earth. On November 1 both peaks are strongly increased and slightly shifted to lower frequencies (dashed black line). The peak at the higher frequency is now also visible in the GAIN ASD (dashed blue line) though it is damped by the vibration isolator system. The other one is still completely filtered. Figure 6.8 shows an enlarged detail of the microseism. It also includes the corresponding ASDs of the seismometer CMG-40 (orange lines), which was operated next to the atom interferometer. A comparison between the ASDs of November 1 illustrates the suppression of seismic vibrations for the GAIN and SG-30 sensors. On November 4 its signal is limited by its internal noise at lower frequencies. The peak at 0.87 Hz is due to the MOT coils of the GAIN sensor, which are pulsed at the repetition rate.

[2]The ASD has been calculated from the gravity values using the LTPDA toolbox [94] for the computational environment MATLAB [95].

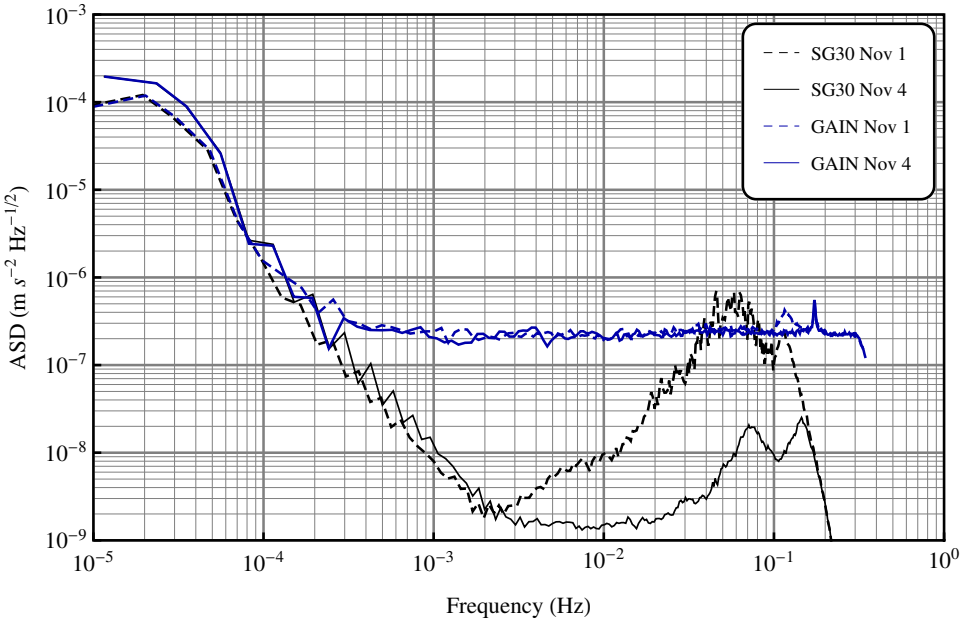

Figure 6.7.: Amplitude spectral densities of the atom interferometer (blue lines) and superconducting gravimeter (black lines) signals. Solid and dashed lines represent different measurement times.

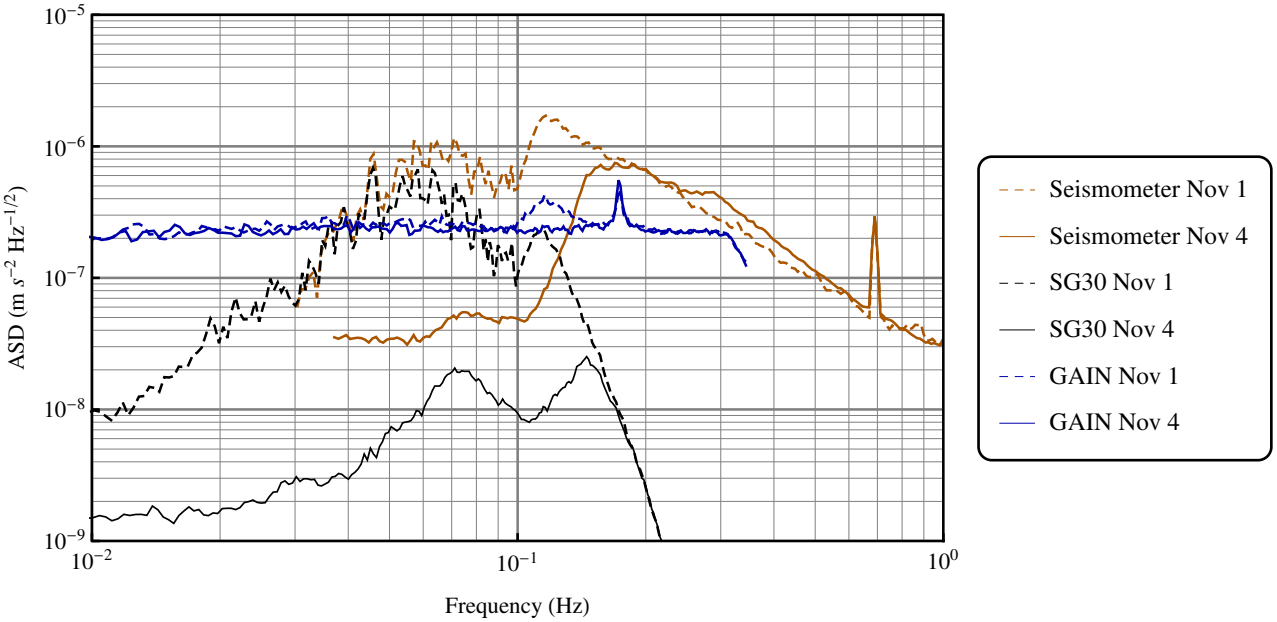

Figure 6.8.: Enlarged detail of the amplitude spectral densities with additional seismometer signals (orange lines).

6.3.6. Absolute gravity value

The absolute gravity value has been measured for several times on the pillars in the gravimeter house mainly by FG5 absolute gravimeters. It applies to a height of 1.25 m at the position of the pillar the atom interferometer has been operated at. The observations made by the superconducting gravimeter have been used to identify temporal variations between different measurement times and to correct for them. For the period of our measurement the time series of the SG-30 indicates an absolute level which is 10 $\mathrm{nm/s^2}$ below the mean value. This gives $9\,808\,369\,623 \pm 18\,\mathrm{nm/s^2}$ for the period between October 27, 2013 and November 07, 2013 [91, 96].

The absolute value measured by the atom interferometer is, up to now, only a preliminary value since not all possible systematic effects have been investigated to the full extent. Therefore, no number is given for the uncertainty here. The value has been transferred from the effective measurement height of 1.388 ± 0.002 m to the height given above with the help of Eq. 2.58 and the local gravity gradient of $2900\,\mathrm{nm/s^2/m}$. The latter was also provided by the BKG. The preliminary absolute value yields $9\,808\,369\,754\,\mathrm{nm/s^2}$ which is only $131\,\mathrm{nm/s^2}$ above the expected value for this period. A large part of the difference might be due to the influence of wave fronts and MOT coil switching (see Chapter 5).

6.4. Mobility of the instrument

Another aspect of the comparison campaigns is the level of mobility of the GAIN instrument. The campaigns were performed at different locations and their order reflect the level of mobility reached at the correspondent time. The locations also determined the choice of the classical gravimeter to compare with because of their different flexibilities.

- During the first campaign in December, 2012 the GAIN sensor was operated at its regular place in our laboratory on the second floor. The gPhone, which is highly flexible, e.g., it can be operated in this environment with only slightly reduced performance, was operated next to our sensor. This way, operative readiness of the atom interferometer could be assured in advance.

- For the second campaign it was important to perform the measurements on the first floor, i.e., at ground level, to achieve a good performance with the FG5 instrument. Therefore, the GAIN sensor was moved in June, 2013 to another room in the same building where it was reinstalled over the period of a few weeks to full operation. This period also included part of the changes made to the laser system. The temperature variations inside the new room, which was equipped with an air conditioning not designed for an optics laboratory, increased to approximately 5 °C. The new installed switching modules as part of the laser cooling system (see Seq. 3.2) allowed for almost continuous operation also in this more demanding environment with, at the same time, a drastically reduced need for realignment during the campaign. The migration within a building was also a first test of the mobility.

- The third comparison campaign was performed together with the superconducting gravimeter SG-30, which is installed at the geodetic observatory Wettzell operated by the BKG.

Location:	December 4, 2012 2nd floor	June 8, 2013 1st floor	November 2, 2013 Dedicated pillar
Extracted from:			
RMS standard deviation	$113\,\mathrm{nm/s^2}$	$176\,\mathrm{nm/s^2}$	$142\,\mathrm{nm/s^2}$
Limit from mirror vibrations	$115\,\mathrm{nm/s^2}$	$173\,\mathrm{nm/s^2}$	$167\,\mathrm{nm/s^2}$
Allan deviation for $\tau = 1.5\,\mathrm{s}$ [(a)]	$115\,\mathrm{nm/s^2}$	$151\,\mathrm{nm/s^2}$	$126\,\mathrm{nm/s^2}$
ASD "white noise level" [(a,b)]			$163\,\mathrm{nm/s^2}$

Table 6.4.: Atom interferometer noise per single shot in different environments, obtained with different methods. [(a)]The Allan deviation and ASD have been calculated for periods of several days. [(b)]ASD level around $10^{-2}\,\mathrm{Hz}$ in Fig. 6.7 divided by $\sqrt{1.5\,/\mathrm{Hz}}$.

In September, 2013 the GAIN instrument was transported over 600 km to the South of Germany to compare it to the most sensitive gravimeter type. This time reinstalling and complete alignment was achieved within a few days.

- The time needed for reassembling could be further reduced to less than a day after the return transport to Berlin by optimizing the work flow.

6.5. Noise analysis

During the campaigns the atom interferometer was operated at three different locations with changing vibrational levels. Table 6.4 summarizes the the RMS standard deviations and also the expected limitations calculated from the residual vibrational noise of the reference mirror (see 3.1.2). Both have been calculated for the same periods. In addition, the interferometer noise is extracted from the Allan deviation and the ASD which represent longer periods.

The analysis reveals two important information. The first aspect is the limit due to the residual mirror vibrations. It is very similar to the interferometer noise in each of the campaigns. Hence, the vibrations seem to be the dominant limitation of the interferometer. This also matches with other observations. Noise measurements in a Doppler-free configuration, where the two Raman beams from the top drive the interferometer transitions and the influence of the reference mirror is excluded, showed RMS phase noise corresponding to only $38\,\mathrm{nm/s^2}$ per shot. A second aspect are the differences of the noise levels between the campaigns. They slightly vary between $113\,\mathrm{nm/s^2}$ to $176\,\mathrm{nm/s^2}$ while the best result was observed at the laboratory on the second floor which was the location with the strongest floor vibrations. The resulting limitation on the dedicated pillar in Wettzell is unexpectedly not lower but even slightly higher. In this regard, it was not possible to profit from the significantly lower floor vibrations (see Fig. 6.8 and Fig. 3.3). This behavior indicates an effective noise floor on top of the active vibration isolator resulting in a decreased damping at seismic quiet sites. It would also explain the stable noise level observed during day- and nighttime.

7. Conclusion and perspectives

During this thesis the GAIN atom interferometer has undergone a number of modifications which all have also been designed with regard to mobile measurements and increased long-term stability of the sensor. The newly developed laser switching modules clearly reduce the amount of maintenance during operation and after transportation. They build one key component for the achievement of the presented results. In addition, their volume has been reduced to approximately 10 % of the former module and thus their design can be seen as one first building block for a potential further miniaturized atom interferometer in the future. The Raman laser subsystem has been equipped with an additional intensity stabilization system which is capable of controlling the two Raman laser beams after their overlapping. Their ratio is kept constant at a position from whereon there are only common perturbations. This way possible AC Stark shifts influencing the interferometer are kept constant. A new method for tilt control has been developed. It suppresses another systematic effect to a sufficient level and allows for instantaneous monitoring.

The atom interferometer has been compared to the three well-established gravimeter types commonly used. During the first and second campaign sensitivities as low as $138\,\mathrm{nm/s^2}/\sqrt{\mathrm{Hz}}$, which was similar to the one of the gPhone and superior to the one of the FG5X, have been demonstrated. It has been found that the sensitivity is mainly limited by the residual vibrations of the reference mirror and not by the atom interferometer itself. After completion of all modifications an improved level of mobility of the instrument has been reached. It has been proven during the transport to Wettzell and by the efficient recommissioning. At this new location the long-term stability has been investigated in a comparison with a superconducting gravimeter. Residual variations of below $\pm 10\,\mathrm{nm/s^2} \approx 10^{-9}\,\mathrm{g}$ without observable long-term drifts and an Allan deviation of 5×10^{-11} for an integration time of $\approx 10^5\,\mathrm{s}$ has been reached. To our best knowledge this is the first time this level of stability could be achieved with a gravimeter based on atom interferometry. It enables the atom interferometer to determine the scaling factor of the superconducting gravimeter with very high precision. If the observed time delay of the GAIN sensor can be sufficiently suppressed in the future, the instrument will offer the ability to characterize two important properties of superconducting gravimeters.

The realization of drift-free measurements provides the basis for the determination of the absolute gravity value with the targeted precision of $5 \times 10^{-10}\,\mathrm{g}$. The preliminary value measured during the last campaign only differs by $1.5 \times 10^{-8}\,\mathrm{g}$ from the value provided by the BKG. It is expected that a closer analysis of the two major remaining systematic effects, wave front distortions and pulsed magnetic fields from the MOT coils, will reduce this offset and reveal an uncertainty at the lower $10^{-9}\,\mathrm{g}$ level or better. This is also the order of magnitude for deviations between other established absolute gravimeters [52]. A complete understanding of the systematic effects of the atom interferometer at this level could help to improve gravity observations in general. An appropriate magnetic shield will be installed within the next months.

Further improvements might also be possible for the sensitivity of the GAIN sensor, since it has become clear that limitations are mainly due to the residual vibrations and that they, in the current setup, don't decrease at seismic quiet locations. Vibration isolation stages based on the scheme used here have already demonstrated enhanced sensitivities by a factor of ≈ 3 at seismic quiet locations [33, 97]. Other interesting developments include a combination of an atom interferometer and a classical accelerometer without an vibration isolation platform but with real time correction of the phase of the atom interferometer. It reaches a larger bandwidth which could be used for navigation [98]. In another experiment [23, 99] two separated atomic clouds are used for a dual simultaneous atom interferometer in order to measure the gravity gradient at the same time. The differential acceleration measurement has the advantage of a common-mode rejection of the vibrational noise. This scheme could in principle also be implemented into the existing GAIN setup.

A. Tidal parameters

The tidal prediction, ocean loading, and polar motion have been calculated with the software T-Soft [81] using the parameters the following parameter sets. Earth orientation parameters for the calculation of polar motion effects have been obtained from the IERS (`ftp://hpiers.obspm.fr/iers/eop/eopc04_05/`).

For Berlin

Frequency		Amplitude	Phase	Tide symbol
from	to			
0.000000	0.002427	1.000000	0.0000	DC
0.002428	0.249951	1.160000	0.0000	Long
0.721500	0.906315	1.154250	0.0000	Q1
0.921941	0.974188	1.154240	0.0000	O1
0.989049	0.998028	1.149150	0.0000	P1
0.999853	1.216397	1.134890	0.0000	K1
1.719381	1.906462	1.161720	0.0000	N2
1.923766	1.976926	1.161720	0.0000	M2
1.991787	2.002885	1.161720	0.0000	S2
2.003032	2.182843	1.161720	0.0000	K2
2.753244	3.081254	1.07338	0.0000	M3
3.791964	3.937897	1.03900	0.0000	M4

Table A.1.: Tidal parameters for Berlin-Adlershof from [89]

Component	Amplitude	Phase
cM2 :	1.0115e-008	52479
cS2 :	3.4929e-009	25350
cK1 :	1.7434e-009	75865
cO1 :	1.3859e-009	142457
cN2 :	2.1046e-009	76773
cP1 :	6.3896e-010	83687
cK2 :	8.9715e-010	24409
cQ1 :	3.0384e-010	-133923
Mf :	0.0000	0.0000
Mm :	0.0000	0.0000
Ssa :	0.0000	0.0000

Table A.2.: Ocean loading parameters for Berlin-Adlershof from [89]

For Wettzell

0.000000	0.000010	1.00000	0.0000	long
0.000011	0.003426	1.16000	0.0000	SA
0.004709	0.010952	1.16000	0.0000	SSA
0.025811	0.031745	1.16000	0.0000	MSM
0.033406	0.044653	1.16413	-0.2564	MM
0.060131	0.068640	1.13394	-2.6340	MSF
0.069845	0.080798	1.14618	0.5581	MF
0.096422	0.104932	1.05720	-2.7465	MSTM
0.106136	0.115412	1.15201	0.4617	MTM
0.130192	0.143814	1.07174	1.4338	MSQM
0.145166	0.249952	1.07405	2.7620	MQM
0.721499	0.833113	1.15321	-0.5698	SGQ1
0.851181	0.859691	1.15099	-0.6368	2Q1
0.860895	0.892332	1.14803	-0.5287	SGM1
0.892639	0.892951	1.09091	1.0752	3MK1
0.893096	0.896130	1.14598	-0.1533	Q1
0.897806	0.906316	1.14643	-0.0698	RO1
0.921940	0.930450	1.14852	0.1212	O1
0.931963	0.940488	1.15457	0.3437	TAU1
0.958085	0.963857	1.14417	0.3892	NTAU
0.965532	0.965828	1.14991	0.3143	LK1
0.965842	0.966285	1.08257	0.5669	M1
0.966298	0.966757	1.15184	0.1653	NO1
0.968564	0.974189	1.15037	0.1650	CHI1
0.989048	0.995144	1.14713	0.3049	PI1

Frequency		Amplitude	Phase	Tide symbol
from	to			
0.996967	0.998029	1.14896	0.1671	P1
0.999852	1.000148	1.12173	3.0010	S1
1.001824	1.003652	1.13560	0.2230	K1
1.005328	1.005624	1.24923	0.8594	PSI1
1.007594	1.013690	1.16486	-0.1826	PHI1
1.028549	1.034468	1.15449	0.0787	TET1
1.036291	1.039193	1.15557	0.1071	J1
1.039323	1.039649	1.08156	0.3972	3MO1
1.039795	1.071084	1.15508	0.1947	SO1
1.072582	1.080945	1.15285	0.1639	OO1
1.099160	1.216398	1.15369	0.3790	NU1
1.719380	1.823400	1.13564	1.7441	3N2
1.825517	1.856954	1.14920	1.5689	EPS2
1.858776	1.859382	1.06597	0.0086	3MJ2
1.859542	1.862429	1.16147	2.3841	2N2
1.863633	1.895070	1.16150	2.1001	MU2
1.895362	1.895689	1.07294	0.0679	3MK2
1.895834	1.896749	1.17662	1.9754	N2
1.897953	1.906463	1.17787	1.9107	NU2
1.923765	1.927418	1.18174	1.8966	GAM2
1.929388	1.930155	1.22538	-0.4048	ALF2
1.931360	1.933188	1.18426	1.4344	M2
1.934392	1.935322	1.22596	1.0342	BET2
1.936982	1.942754	1.16266	-0.1161	DEL2
1.958232	1.963709	1.18772	0.8189	LAM2
1.965826	1.968566	1.18615	1.0721	L2
1.968727	1.969170	1.06721	-0.1797	3MO2
1.969183	1.976927	1.18773	1.0716	KNO2
1.991786	1.998288	1.18409	0.4838	T2
1.999705	2.000767	1.18393	0.3400	S2
2.002590	2.003033	1.20345	1.0792	R2
2.004709	2.005167	0.98011	-1.0829	3MQ2
2.005312	2.013690	1.18461	0.5371	K2
2.031287	2.047391	1.18205	0.1235	ETA2
2.067578	2.073660	1.16462	-0.6703	2S2
2.075939	2.182844	1.16938	-0.3883	2K2
2.753243	2.869714	1.07009	0.5366	MN3
2.892639	2.903887	1.06944	0.3803	M3
2.927106	2.940326	1.08194	0.1090	ML3
2.965989	3.081255	1.05853	0.2767	MK3

Frequency		Amplitude	Phase	Tide symbol
from	to			
3.791963	3.833114	0.52662	-81.2471	N4
3.864399	3.901459	0.31428	61.6901	M4
3.937748	3.937898	1.05822	37.2413	K4

Table A.3.: Tidal parameters for Wettzell from [91]

B. Raman intensity controller

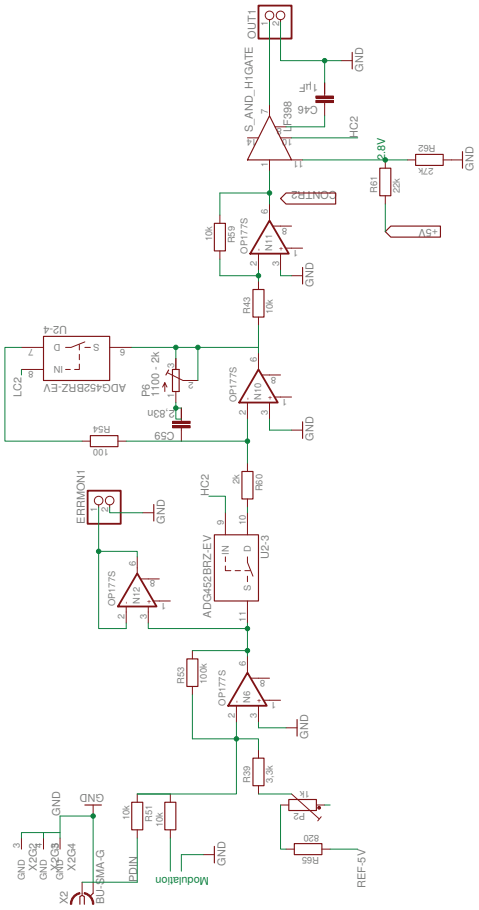

Figure B.1.: Raman intensity controller circuit: The feedback control loop includes a proportional-integral (PI) circuit and an additional sample and hold chip at the output (OUT1). During the control phase, when the appropriate photodiode signal is present at the input (PDIN), the feedback signal passes the sample and hold chip. When switching into hold state the output is kept constant at its latest value. A copy of the circuit controls the second laser beam intensity. The logic for switching between states is implemented using a microcontroller, see Fig. B.2.

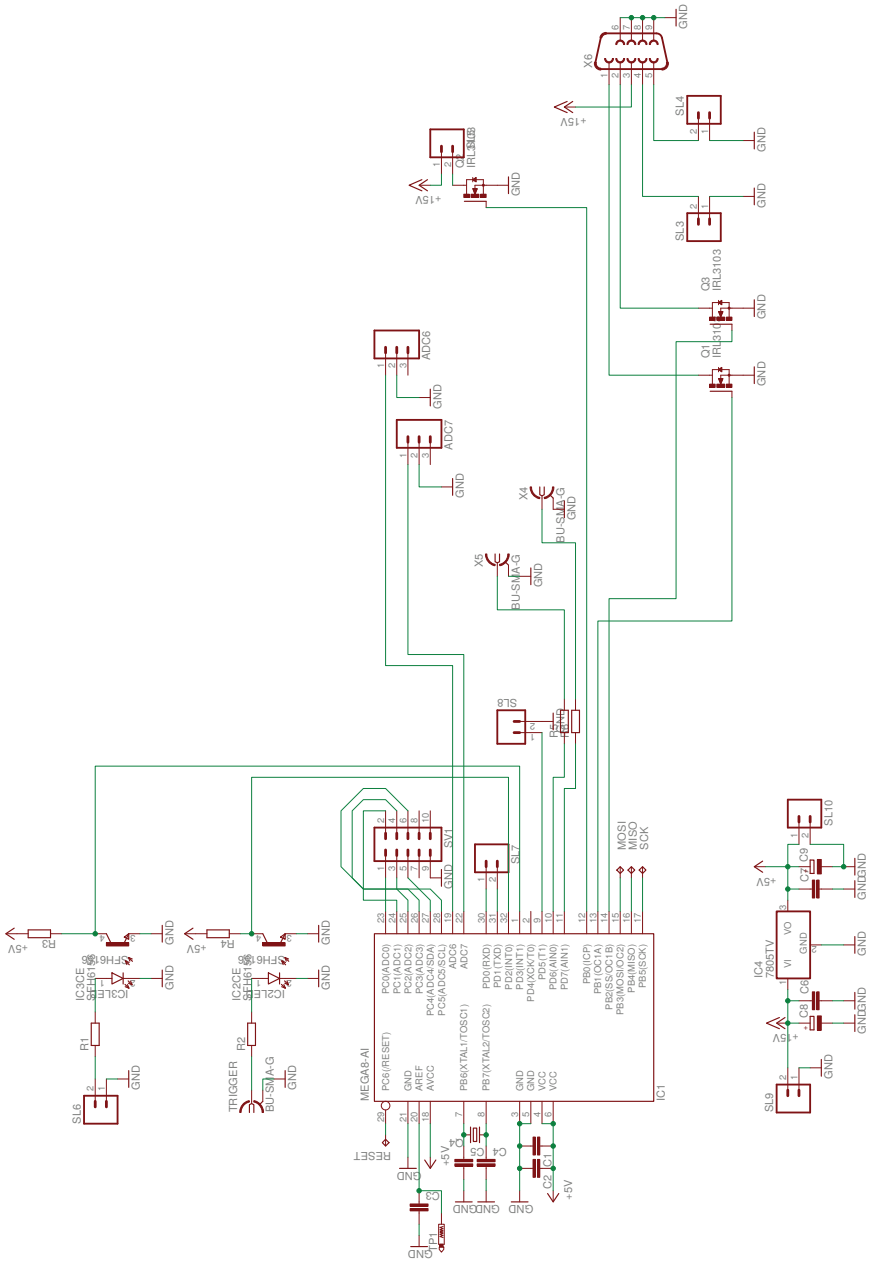

Figure B.2.: Raman intensity controller logic: When triggered at its input the microcontroller itself sends trigger signals with a certain timing to interrupt the frequency stabilization of the Raman slave laser and hold its latest feedback parameters constant. Then, the controller consecutively closes the shutters for the two Raman laser beams and activate the corresponding intensity control loops. Finally, the frequency stabilization is reactivated and the control signals for the laser intensity are hold constant.

C. Allan variance

The Allan variance is a measure for the stability of a signal in the time domain. It is commonly used for the noise analysis of the frequencies of clocks but can also be applied to other signals. In contrast to the standard variance it is convergent for most types of noise which can be found in frequency sources [93].

The standard variance over N samples is given for a time series of measured frequencies ν_n by

$$s^2 = \frac{1}{N-1}\sum_{i=1}^{N}(y_i - m)^2 \tag{C.1}$$

with the fractional or normalized frequency deviations

$$y_i = \frac{\nu_i - \nu_0}{\nu_0}. \tag{C.2}$$

ν_0 is the carrier frequency and the single measurements are sampled over the observation period τ_0 and spaced by the time $T \geq \tau_0$. The mean value is $m = \frac{1}{N}\sum_{i=1}^{N} y_i$. For measurements without dead time, i.e., $\tau_0 = T$, the expected value of the two sample variance ($N = 2$) gives the Allan variance. It is defined as [92, 93]

$$\begin{aligned}\sigma_y^2(\tau_0) &= \frac{1}{2}\langle (y_{i+1} - y_i)^2 \rangle \\ &= \frac{1}{2(M-1)}\sum_{i=1}^{M-1}(y_{i+1} - y_i)^2\end{aligned} \tag{C.3}$$

for the number of M fractional frequency values. It can also be calculated for multiples of the original sampling time $\tau = n\tau_0$ by first averaging n adjacent samples to $\bar{y}_k = \langle y_i \rangle_k$ lying within the kth of $\lfloor M/n \rfloor$ time intervals.

In the case, when the measured frequencies ν_i are still sampled over τ_0 but have spacings due to dead times of the measurement process ($T > \tau_0$), the two sample variance including dead time $\sigma_y^2(N = 2, T, \tau)$ is related to the Allan variance $\sigma_y^2(\tau)$ via the bias function [100]

$$B_2(T/\tau, \mu) = \frac{\sigma_y^2(N = 2, T, \tau)}{\sigma_y^2(N = 2, T = \tau, \tau)} = \frac{\sigma_y^2(N = 2, T, \tau)}{\sigma_y^2(\tau)}. \tag{C.4}$$

The parameter μ is connected to the noise type of the measured data and describes the dependence of the Allan variance on the averaging time

$$\sigma_y^2(\tau) \propto \tau^{\mu}. \tag{C.5}$$

It becomes visible as the slope of the Allan variance when the latter is plotted on a double logarithmic scale. The parameter μ is connected to the exponent α of the power law for the PSD $S_y(f)$

$$S_y(f) \propto f^{\alpha} \tag{C.6}$$

via the relation $\mu = -(\alpha + 1),\ \alpha < 2$. For white noise the parameters yield $\mu = -1$ and $\alpha = 0$ and the relevant bias function is $B_2(T/\tau \geq 1, \mu = -1) = 1$ [100]. The gravity residuals, after correction for the tidal signals, are in good accordance with this noise type and thus the dead time of the measurement process can be neglected.

The Allan deviation $\sigma_y(\tau)$ is the square root of the Allan variance $\sigma_y^2(\tau)$.

D. Effect on gravity from atmospheric mass redistribution

Gravity variations due to atmospheric mass redistribution have been estimated using the following equation

$$g_{\mathrm{atm}} = a_{\mathrm{atm}}(p - p_0) \tag{D.1}$$

with the local air pressure p and the admittance factor $a_{\mathrm{atm}} \approx 3.0\,\mathrm{nm/s^2/hPa}$. The normal atmospheric pressure p_0 is calculated with the help of the international standard atmosphere

$$p_0 = 1013.24\,\mathrm{hPa}\left(1 - \frac{0.0065 \cdot h}{288.15\,\mathrm{m}}\right)^{5.2559} \tag{D.2}$$

and gives 942.5 hPa for Wettzell (606.6 m above sea level) and 1009.0 hPa for Berlin-Adlershof (35.3 m). h is the local height above sea level.

E. Measurement in Wettzell

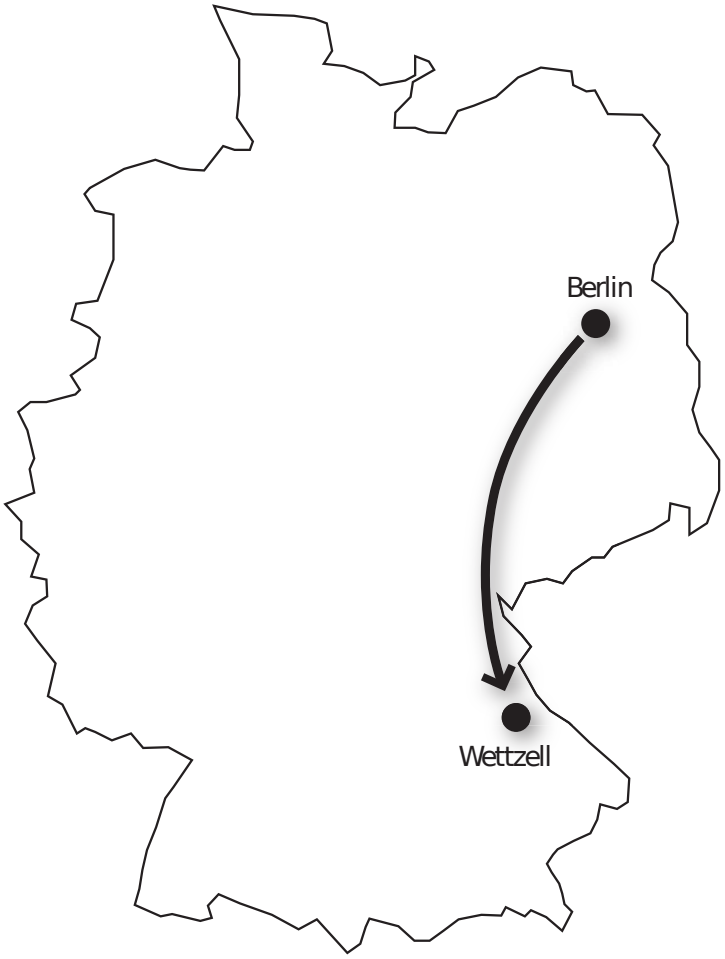

Figure E.1.: Transport from Berlin to Wettzell over a distance of about 500 km.

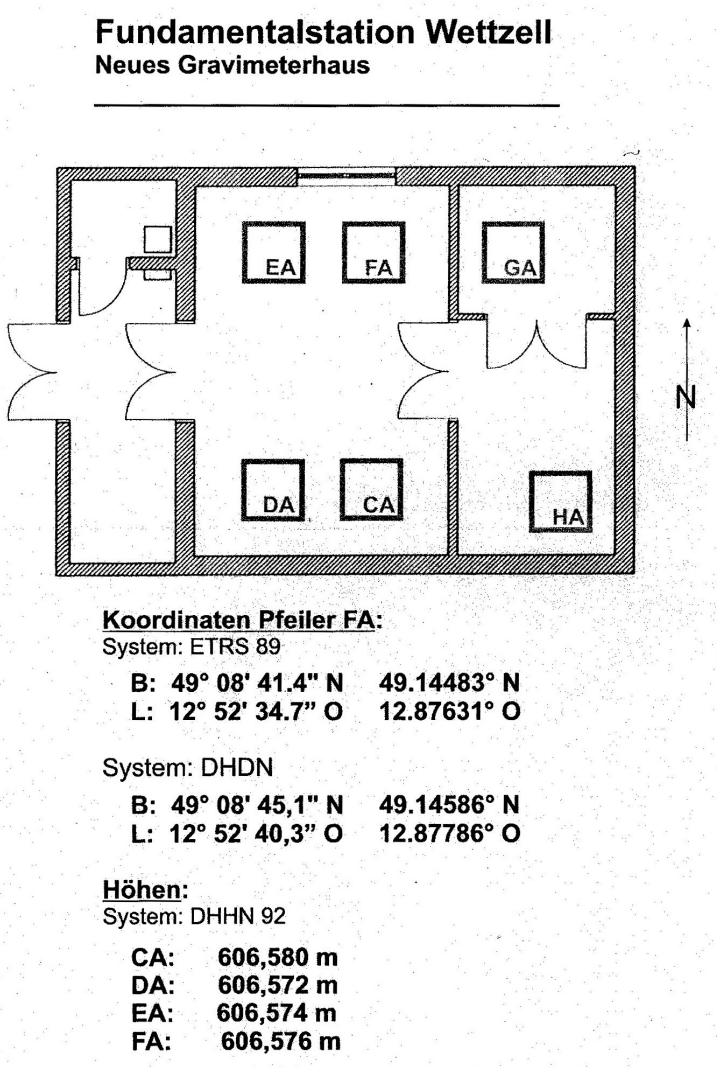

Figure E.2.: Map of the gravimeter house at the Geodetic observatory Wettzell, from [91]. The atom interferometer was installed at the pillar marked with "FA". The superconducting gravimeter was on pillar "GA".

Bibliography

[1] J. Ehlers and G. Börner, editors. *Gravitation*. Spektrum, Heidelberg, 2. edition, 1996.

[2] I. Ciufolini and J. Wheeler. *Gravitation and Inertia*. Princeton University Press, Princeton, New Jersey, 1995.

[3] T. Quinn. Fundamental constants. Measuring big G. *Nature*, 408(6815):919–21, October 2000.

[4] G. T. Gillies. The Newtonian gravitational constant: recent measurements and related studies. *Reports on Progress in Physics*, 60(2):151–225, February 1997.

[5] P. Baldi, E. Campari, G. Casula, S. Focardi, and F. Palmonari. Testing Newton's inverse square law at intermediate scales. *Physical Review D*, 64(8):082001, September 2001.

[6] E. Adelberger, B. Heckel, S. Hoedl, C. Hoyle, D. Kapner, and A. Upadhye. Particle-Physics Implications of a Recent Test of the Gravitational Inverse-Square Law. *Physical Review Letters*, 98(13):13–16, March 2007.

[7] I. Marson and J. E. Faller. g-the acceleration of gravity: its measurement and its importance. *Journal of Physics E: Scientific Instruments*, 19(1):22–32, January 1986.

[8] I. Marson. A Short Walk along the Gravimeters Path. *International Journal of Geophysics*, 2012:1–9, 2012.

[9] W. Torge. *Geodäsie*. Walter de Gruyter GmbH & Co. KG, 10785 Berlin, 2 edition, 2003.

[10] D. Agnew. 3.06 - Earth Tides. In G. Schubert, editor, *Treatise on Geophysics*, pp. 163–195. Elsevier, Amsterdam, 2007.

[11] M. Hauth, C. Freier, V. Schkolnik, A. Peters, H. Wziontek, and M. Schilling. Atom Interferometry for Absolute Measurements of Local Gravity. In G. M. Tino and M. A. Kasevich, editors, *Proceedings of the International School of Physics "Enrico Fermi", Course 188*, pp. 557–586, Amsterdam, 2014. SIF, Bologna and IOS Press.

[12] L. Timmen. Absolute and Relative Gravimetry. In G. Xu, editor, *Sciences of Geodesy - I: Advances and Future Directions*, chapter 1, pp. 1–48. Springer, Berlin, Heidelberg, 2010.

[13] J. Hinderer, D. Crossley, and R. J. Warburton. Gravimetric methods - superconducting gravity meters. In G. Schubert, editor, *Treatise on Geophysics*, chapter 3.04, pp. 65–122. Elsevier, Amsterdam, 2007.

[14] D. Crossley, J. Hinderer, and U. Riccardi. The measurement of surface gravity. *Reports on progress in physics. Physical Society (Great Britain)*, 76(4):046101, April 2013.

[15] O. Carnal and J. Mlynek. Young's double-slit experiment with atoms: A simple atom interferometer. *Physical Review Letters*, 66(21):2689–2692, May 1991.

[16] D. Keith, C. Ekstrom, Q. Turchette, and D. Pritchard. An interferometer for atoms. *Physical review letters*, 66(21):2693–2696, 1991.

[17] F. Riehle, T. Kisters, A. Witte, J. Helmcke, and C. J. Bordé. Optical Ramsey spectroscopy in a rotating frame: Sagnac effect in a matter-wave interferometer. *Physical review letters*, 67(2):177–180, 1991.

[18] M. A. Kasevich and S. Chu. Atomic interferometry using stimulated Raman transitions. *Physical review letters*, 67(2):181–184, 1991.

[19] D. S. Weiss, B. C. Young, and S. Chu. Precision measurement of h/m Cs based on photon recoil using laser-cooled atoms and atomic interferometry. *Applied Physics B Lasers and Optics*, 59(3):217–256, September 1994.

[20] A. Wicht, J. Hensley, E. Sarajlic, and S. Chu. A preliminary measurement of the fine structure constant based on atom interferometry. *Physica Scripta*, 2002:82, 2002.

[21] A. Bertoldi, G. Lamporesi, L. Cacciapuoti, M. de Angelis, M. Fattori, T. Petelski, A. Peters, M. Prevedelli, J. Stuhler, and G. M. Tino. Atom interferometry gravity-gradiometer for the determination of the Newtonian gravitational constant G. *The European Physical Journal D*, 40(2):271–279, September 2006.

[22] J. Fixler, G. T. Foster, J. M. McGuirk, and M. A. Kasevich. Atom interferometer measurement of the newtonian constant of gravity. *Science (New York, N.Y.)*, 315(5808):74–7, January 2007.

[23] F. Sorrentino, Y.-H. Lien, G. Rosi, L. Cacciapuoti, M. Prevedelli, and G. M. Tino. Sensitive gravity-gradiometry with atom interferometry: progress towards an improved determination of the gravitational constant. *New Journal of Physics*, 12(9):095009, September 2010.

[24] G. Rosi, F. Sorrentino, L. Cacciapuoti, M. Prevedelli, and G. M. Tino. Precision measurement of the Newtonian gravitational constant using cold atoms. *Nature*, 510(7506): 518–21, June 2014.

[25] T. L. Gustavson, P. Bouyer, and M. A. Kasevich. Precision Rotation Measurements with an Atom Interferometer Gyroscope. *Physical Review Letters*, 78(11):2046–2049, March 1997.

[26] G. Tackmann, P. Berg, C. Schubert, S. Abend, M. Gilowski, W. Ertmer, and E. M. Rasel. Self-alignment of a compact large-area atomic Sagnac interferometer. *New Journal of Physics*, 14(1):015002, January 2012.

[27] A. Gauguet, B. Canuel, T. Lévèque, W. Chaibi, and A. Landragin. Characterization and limits of a cold-atom Sagnac interferometer. *Physical Review A*, 80(6):063604, December 2009.

[28] A. Peters, K.-Y. K. Chung, and S. Chu. Measurement of gravitational acceleration by dropping atoms. *Nature*, 400:849–852, 1999.

[29] A. Peters, K.-Y. Chung, and S. Chu. High-precision gravity measurements using atom interferometry. *Metrologia*, 38:25, 2001.

[30] A. Louchet-Chauvet, T. Farah, Q. Bodart, A. Clairon, A. Landragin, S. Merlet, and F. Pereira Dos Santos. The influence of transverse motion within an atomic gravimeter. *New Journal of Physics*, 13(6):065025, June 2011.

[31] J. M. McGuirk, G. Foster, J. Fixler, M. Snadden, and M. A. Kasevich. Sensitive absolute-gravity gradiometry using atom interferometry. *Physical Review A*, 65(3):033608, February 2002.

[32] H. Müller, S.-w. Chiow, S. Herrmann, S. Chu, and K.-Y. Chung. Atom-Interferometry Tests of the Isotropy of Post-Newtonian Gravity. *Physical Review Letters*, 100(3):031101, January 2008.

[33] Z.-K. Hu, B.-L. Sun, X.-C. Duan, M.-K. Zhou, L.-L. Chen, S. Zhan, Q.-Z. Zhang, and J. Luo. Demonstration of an ultrahigh-sensitivity atom-interferometry absolute gravimeter. *Physical Review A*, 88(4):043610, October 2013.

[34] B. Canuel, F. Leduc, D. Holleville, A. Gauguet, J. Fils, A. Virdis, A. Clairon, N. Dimarcq, C. J. Bordé, A. Landragin, and P. Bouyer. Six-Axis Inertial Sensor Using Cold-Atom Interferometry. *Physical Review Letters*, 97(1):1–4, July 2006.

[35] R. Geiger, V. Ménoret, G. Stern, N. Zahzam, P. Cheinet, B. Battelier, A. Villing, F. Moron, M. Lours, Y. Bidel, A. Bresson, A. Landragin, and P. Bouyer. Detecting inertial effects with airborne matter-wave interferometry. *Nature Communications*, 2:474, September 2011.

[36] Q. Bodart, S. Merlet, N. Malossi, F. Pereira Dos Santos, P. Bouyer, and A. Landragin. A cold atom pyramidal gravimeter with a single laser beam. *Applied Physics Letters*, 96 (13):134101, 2010.

[37] S. Dimopoulos, P. W. Graham, J. M. Hogan, and M. A. Kasevich. Testing General Relativity with Atom Interferometry. *Physical Review Letters*, 98(11):1–4, March 2007.

[38] S. Herrmann, H. Dittus, and C. Lämmerzahl. Testing the equivalence principle with atomic interferometry. *Classical and Quantum Gravity*, 29(18):184003, September 2012.

[39] G. M. Tino, F. Sorrentino, D. N. Aguilera, B. Battelier, A. Bertoldi, Q. Bodart, K. Bongs, P. Bouyer, C. Braxmaier, L. Cacciapuoti, N. Gaaloul, N. Gürlebeck, M. Hauth, S. Herrmann, M. Krutzik, A. Kubelka, A. Landragin, A. Milke, A. Peters, E. M. Rasel, E. Rocco,

C. Schubert, T. Schuldt, K. Sengstock, and A. Wicht. Precision Gravity Tests with Atom Interferometry in Space. *Nuclear Physics B - Proceedings Supplements*, 243-244:203–217, October 2013.

[40] A. Bonnin, N. Zahzam, Y. Bidel, and A. Bresson. Simultaneous dual-species matter-wave accelerometer. *Physical Review A*, 88(4):043615, October 2013.

[41] D. Schlippert, J. Hartwig, H. Albers, L. Richardson, C. Schubert, A. Roura, W. P. Schleich, W. Ertmer, and E. M. Rasel. Quantum Test of the Universality of Free Fall. *Physical Review Letters*, 112(20):203002, May 2014.

[42] F. Sorrentino, K. Bongs, P. Bouyer, L. Cacciapuoti, M. Angelis, H. Dittus, W. Ertmer, A. Giorgini, J. Hartwig, M. Hauth, S. Herrmann, M. Inguscio, E. Kajari, T. T. Könemann, C. Lämmerzahl, A. Landragin, G. Modugno, F. Pereira Dos Santos, A. Peters, M. Prevedelli, E. M. Rasel, W. P. Schleich, M. Schmidt, A. Senger, K. Sengstock, G. Stern, G. M. Tino, and R. Walser. A Compact Atom Interferometer for Future Space Missions. *Microgravity Science and Technology*, 22(4):551–561, September 2010.

[43] STE-QUEST-Team. STE-QUEST Assessment Study Report (Yellow Book). Technical Report December, 2013. URL `http://sci.esa.int/jump.cfm?oid=53445`.

[44] D. N. Aguilera, H. Ahlers, B. Battelier, A. Bawamia, A. Bertoldi, R. Bondarescu, K. Bongs, P. Bouyer, C. Braxmaier, L. Cacciapuoti, C. Chaloner, M. Chwalla, W. Ertmer, M. Franz, N. Gaaloul, M. Gehler, D. Gerardi, L. Gesa, N. Gürlebeck, J. Hartwig, M. Hauth, O. Hellmig, W. Herr, S. Herrmann, A. Heske, A. Hinton, P. Ireland, P. Jetzer, U. Johann, M. Krutzik, A. Kubelka, C. Lämmerzahl, A. Landragin, I. Lloro, D. Massonnet, I. Mateos, A. Milke, M. Nofrarias, M. Oswald, A. Peters, K. Posso-Trujillo, E. M. Rasel, E. Rocco, A. Roura, J. Rudolph, W. P. Schleich, C. Schubert, T. Schuldt, S. Seidel, K. Sengstock, C. F. Sopuerta, F. Sorrentino, D. Summers, G. M. Tino, C. Trenkel, N. Uzunoglu, W. von Klitzing, R. Walser, T. Wendrich, A. Wenzlawski, P. Weßels, A. Wicht, E. Wille, M. Williams, P. Windpassinger, and N. Zahzam. STE-QUEST—Test of the universality of free fall using cold atom interferometry. *Classical and Quantum Gravity*, 31(11):115010, June 2014.

[45] J. M. Hogan, D. M. S. Johnson, S. Dickerson, T. Kovachy, A. Sugarbaker, S.-w. Chiow, P. W. Graham, M. A. Kasevich, B. Saif, S. Rajendran, P. Bouyer, B. D. Seery, L. Feinberg, and R. Keski-Kuha. An atomic gravitational wave interferometric sensor in low earth orbit (AGIS-LEO). *General Relativity and Gravitation*, 43(7):1953–2009, May 2011.

[46] M. A. Kasevich and S. Chu. Measurement of the gravitational acceleration of an atom with a light-pulse atom interferometer. *Applied Physics B: Lasers and Optics*, 54:321–332, 1992.

[47] J. M. Goodkind. The superconducting gravimeter. *Review of Scientific Instruments*, 70 (11):4131, 1999.

[48] O. Francis and T. van Dam. Evaluation of the precision of using absolute gravimeters to calibrate superconducting gravimeters. *Metrologia*, 39(5):485–488, October 2002.

[49] T. M. Niebauer, G. S. Sasagawa, J. E. Faller, R. Hilt, and F. Klopping. A new generation of absolute gravimeters. *Metrologia*, 32(3):159–180, January 1995.

[50] T. M. Niebauer, R. Billson, B. Ellis, B. Mason, D. van Westrum, and F. Klopping. Simultaneous gravity and gradient measurements from a recoil-compensated absolute gravimeter. *Metrologia*, 48(3):154–163, June 2011.

[51] R. L. Rinker. *Super spring–a new type of low-frequency vibration isolator*. PhD thesis, University of Colorado, 1983.

[52] O. Francis, H. Baumann, T. Volarik, C. Rothleitner, G. Klein, M. Seil, N. Dando, R. Tracey, C. Ullrich, S. Castelein, H. Hua, W. Kang, S. Chongyang, X. Songbo, T. Hongbo, L. Zhengyuan, V. Pálinkás, J. Kostelecký, J. Mäkinen, J. Näränen, S. Merlet, T. Farah, C. Guerlin, F. Pereira Dos Santos, N. L. Moigne, C. Champollion, S. Deville, L. Timmen, R. Falk, H. Wilmes, D. Iacovone, F. Baccaro, A. Germak, E. Biolcati, J. Krynski, M. Sekowski, T. Olszak, A. Pachuta, J. Agren, A. Engfeldt, R. Reudink, P. Inacio, D. McLaughlin, G. Shannon, M. Eckl, T. Wilkins, D. V. Westrum, and R. Billson. The European Comparison of Absolute Gravimeters 2011 (ECAG-2011) in Walferdange, Luxembourg: results and recommendations. *Metrologia*, 50(3):257–268, June 2013.

[53] L. Timmen, O. Gitlein, V. Klemann, and D. Wolf. Observing Gravity Change in the Fennoscandian Uplift Area with the Hanover Absolute Gravimeter. *Pure and Applied Geophysics*, 169(8):1331–1342, September 2011.

[54] B. Young, M. A. Kasevich, and S. Chu. Precision Atom Interferometry with Light Pulses. In *Atom Interferometry*, pp. 367–406. P. Berman, 1997.

[55] K. Moler, D. S. Weiss, M. A. Kasevich, and S. Chu. Theoretical analysis of velocity-selective Raman transitions. *Physical Review A*, 45(1):342–348, January 1992.

[56] N. F. Ramsey. *Molecular beams*. Oxford University Press, Oxford, 1956.

[57] N. F. Ramsey. A Molecular Beam Resonance Method with Separated Oscillating Fields. *Physical Review*, 78(6):695–699, June 1950.

[58] P. Cheinet, B. Canuel, F. Pereira Dos Santos, A. Gauguet, F. Yver-Leduc, and A. Landragin. Measurement of the Sensitivity Function in a Time-Domain Atomic Interferometer. *IEEE Transactions on Instrumentation and Measurement*, 57(6):1141–1148, June 2008.

[59] A. Peters. *High Precision Gravity Measurement using Atom Interferometry*. PhD thesis, Stanford University, 1998.

[60] J. Le Gouët, T. Mehlstäubler, J. Kim, S. Merlet, A. Clairon, A. Landragin, and F. Pereira Dos Santos. Limits to the sensitivity of a low noise compact atomic gravimeter. *Applied Physics B*, 92(2):133–144, June 2008.

[61] C. Lämmerzahl and C. J. Bordé. Rabi oscillations in gravitational fields: exact solution. *Physics Letters A*, 9601(July), 1995.

[62] P. Storey and C. Cohen-Tannoudji. The Feynman path integral approach to atomic interferometry. A tutorial. *Journal de Physique II*, 1994.

[63] K. Bongs, R. Launay, and M. A. Kasevich. High-order inertial phase shifts for time-domain atom interferometers. *Applied Physics B*, 84(4):599–602, August 2006.

[64] D. A. Steck. Rubidium 87 D Line Data, 2008.

[65] A. Senger. *A Mobile Atom Interferometer for High Precision Measurements of Local Gravity.* PhD thesis, Humboldt-Universität zu Berlin, 2011.

[66] M. Schmidt. *A mobile high-precision gravimeter based on atom interferometry.* PhD thesis, Humboldt-Universität zu Berlin, 2011.

[67] M. Schmidt, M. Prevedelli, A. Giorgini, G. M. Tino, and A. Peters. A portable laser system for high-precision atom interferometry experiments. *Applied Physics B*, 102(1): 11–18, October 2010.

[68] M. Schmidt, A. Senger, M. Hauth, C. Freier, V. Schkolnik, and A. Peters. A mobile high-precision absolute gravimeter based on atom interferometry. *Gyroscopy and Navigation*, 2(3):170–177, August 2011.

[69] C. Freier. *Measurement of Local Gravity using Atom Interferometry.* Diploma thesis, Humboldt Universität zu Berlin, 2010.

[70] J. Hensley, A. Peters, and S. Chu. Active low frequency vertical vibration isolation. *Review of Scientific Instruments*, 70(6):2735, 1999.

[71] D. L. Platus. Negative-stiffness-mechanism vibration isolation systems. In E. A. Derby, C. G. Gordon, D. Vukobratovich, P. R. Yoder, Jr., and C. H. Zweben, editors, *Proc. SPIE 3786, Optomechanical Engineering and Vibration Control, 98*, pp. 98–105, September 1999.

[72] M. Hauth, C. Freier, V. Schkolnik, A. Senger, M. Schmidt, and A. Peters. First gravity measurements using the mobile atom interferometer GAIN. *Applied Physics B*, 113(1): 49–55, April 2013.

[73] A. Festbaum. *Aufbau eines Moduls zur stabilen Laserverstärkung auf Basis eines Tapered Amplifiers.* Bachelor thesis, Humboldt-Universität zu Berlin, 2013.

[74] Schäfter+Kirchhoff website. URL `http://www.sukhamburg.com/produkte/faserkollimatoren.html`. visited on 14. Oct. 2014.

[75] E. Raab, M. Prentiss, A. Cable, S. Chu, and D. Pritchard. Trapping of neutral sodium atoms with radiation pressure. *Physical Review Letters*, 59(23):2631–2634, 1987.

[76] K. E. Gibble, S. Kasapi, and S. Chu. Improved magneto-optic trapping in a vapor cell. *Optics letters*, 17(7):526–8, April 1992.

[77] H. J. Metcalf and P. Straten. *Laser Cooling and Trapping*. Graduate Texts in Contemporary Physics. Springer New York, New York, NY, 1999.

[78] M. A. Kasevich, D. S. Weiss, E. Riis, K. Moler, S. Kasapi, and S. Chu. Atomic velocity selection using stimulated Raman transitions. *Physical review letters*, 66(18):2297–2300, 1991.

[79] C. Fertig, J. Bouttier, and K. Gibble. Laser-cooled Rb clock. In *Proceedings of the 2000 IEEE/EIA International Frequency Control Symposium and Exhibition (Cat. No.00CH37052)*, pp. 680–686. IEEE, 2000.

[80] Mathematica 9. URL `www.wolfram.com/mathematica/`.

[81] M. Van Camp and P. Vauterin. Tsoft: graphical and interactive software for the analysis of time series and Earth tides. *Computers & Geosciences*, 31(5):631–640, June 2005.

[82] J. M. Hogan, D. M. S. Johnson, and M. A. Kasevich. Light-pulse atom interferometry. In E. Arimondo, W. Ertmer, W. P. Schleich, and E. M. Rasel, editors, *Proceedings of the International School of Physics Enrico Fermi Course CLXVIII on Atom Optics and Space Physics*, pp. 411–447, Oxford, 2007. IOS Press.

[83] S.-Y. Lan, P.-C. Kuan, B. Estey, P. Haslinger, and H. Müller. Influence of the Coriolis Force in Atom Interferometry. *Physical Review Letters*, 108(9):1–5, February 2012.

[84] S. Dickerson, J. M. Hogan, A. Sugarbaker, D. M. S. Johnson, and M. A. Kasevich. Multiaxis Inertial Sensing with Long-Time Point Source Atom Interferometry. *Physical Review Letters*, 111(8):083001, August 2013.

[85] A. Landragin. *Interférométrie atomique : applications aux capteurs inertiels*. Habilitation thesis, 2009.

[86] B. Leykauf. *The effect of wavefront aberrations in light-pulse atom interferometry*. Bachelor thesis, Humboldt-Universität zu Berlin, 2014.

[87] V. Schkolnik, B. Leykauf, M. Hauth, C. Freier, and A. Peters. The effect of wavefront aberrations in atom interferometry. pp. 1–12, November 2014. arXiv:1411.7914.

[88] M. Schilling, Institut für Erdmessung (Leibniz Universität Hannover) - private communication.

[89] A. Reinhold and W. Hoppe. Technischer Bericht (G4-2010-5) Absolute und relative Schweremessungen in der Humboldt-Universität zu Berlin (Campus Adlershof) vom 10.-12.09.2010. Technical report, Bundesamt für Kartographie und Geodäsie, 2010.

[90] M. Schilling, and O. Gitlein, Institut für Erdmessung (Leibniz Universität Hannover).

[91] H. Wziontek, Bundesamt für Kartographie und Geodäsie - private communication.

[92] D. W. Allan. Time and Frequency (Time-Domain) Characterization, Estimation, and Prediction of Precision Clocks and Oscillators. *IEEE Transactions on Ultrasonics, Ferroelectrics and Frequency Control*, 34(6):647–654, November 1987.

[93] W. J. Riley. *Handbook of Frequency Stability Analysis*. National Institute of Standards and Technology, Washington, 2008.

[94] LTPDA 2.8: a MATLAB toolbox for accountable and reproducible data analysis. URL `http://www.lisa.aei-hannover.de/ltpda/`.

[95] MATLAB (R2014a). URL `https://de.mathworks.com/`.

[96] H. Wziontek, R. Falk, and H. Wilmes. Integration of Regional Absolute Gravimeter Comparisons into the Framework of the International Comparisons. Colloque G2 (Géodésie-Géophysique), 17-19 November 2014, Strasbourg, France.

[97] M.-K. Zhou, Z.-K. Hu, X.-C. Duan, B.-L. Sun, L.-L. Chen, Q.-Z. Zhang, and J. Luo. Performance of a cold-atom gravimeter with an active vibration isolator. *Physical Review A*, 86(4):043630, October 2012.

[98] J. Lautier, L. Volodimer, T. Hardin, S. Merlet, M. Lours, F. Pereira Dos Santos, and A. Landragin. Hybridizing matter-wave and classical accelerometers. *Applied Physics Letters*, 105(14):144102, October 2014.

[99] F. Sorrentino, Q. Bodart, L. Cacciapuoti, Y.-H. Lien, M. Prevedelli, G. Rosi, L. Salvi, and G. M. Tino. Sensitivity limits of a Raman atom interferometer as a gravity gradiometer. *Physical Review A*, 89(2):023607, February 2014.

[100] J. Barnes and D. W. Allan. Variances based on data with dead time between the measurements. In *Time and Frequency*, Boulder, 1987. National Bureau of Standards.

[101] F. Sorrentino, K. Bongs, P. Bouyer, L. Cacciapuoti, M. D. Angelis, H. Dittus, W. Ertmer, J. Hartwig, M. Hauth, S. Herrmann, K. Huang, M. Inguscio, E. Kajari, T. Könemann, C. Lämmerzahl, A. Landragin, G. Modugno, F. Pereira Dos Santos, A. Peters, M. Prevedelli, E. M. Rasel, W. P. Schleich, M. Schmidt, A. Senger, K. Sengstock, G. Stern, G. M. Tino, T. Valenzuela, R. Walser, and P. Windpassinger. The Space Atom Interferometer project: status and prospects. *Journal of Physics: Conference Series*, 327:012050, December 2011.

[102] T. Schuldt, C. Schubert, M. Krutzik, L. G. Bote, N. Gaaloul, J. Hartwig, H. Ahlers, W. Herr, K. Posso-Trujillo, J. Rudolph, S. Seidel, T. Wendrich, W. Ertmer, S. Herrmann, A. Kubelka-Lange, A. Milke, B. Rievers, E. Rocco, A. Hinton, K. Bongs, M. Oswald, M. Franz, M. Hauth, A. Peters, A. Bawamia, A. Wicht, B. Battelier, A. Bertoldi, P. Bouyer, A. Landragin, D. Massonnet, T. Lévèque, A. Wenzlawski, O. Hellmig, P. Windpassinger, K. Sengstock, W. von Klitzing, C. Chaloner, D. Summers, P. Ireland, I. Mateos, C. F. Sopuerta, F. Sorrentino, G. M. Tino, M. Williams, C. Trenkel, D. Gerardi,

M. Chwalla, J. Burkhardt, U. Johann, A. Heske, E. Wille, M. Gehler, L. Cacciapuoti, N. Gürlebeck, C. Braxmaier, and E. Rasel. Design of a dual species atom interferometer for space. December 2014. arXiv:1412.2713, accepted for Experimental Astronomy.

Publications

Print

- M. Hauth, C. Freier, V. Schkolnik, A. Peters, H. Wziontek, and M. Schilling. Atom Interferometry for Absolute Measurements of Local Gravity. In G. M. Tino and M. A. Kasevich, editors, *Proceedings of the International School of Physics "Enrico Fermi", Course 188*, pp. 557–586, Amsterdam, 2014. SIF, Bologna and IOS Press

- M. Hauth, C. Freier, V. Schkolnik, A. Senger, M. Schmidt, and A. Peters. First gravity measurements using the mobile atom interferometer GAIN. *Applied Physics B*, 113(1): 49–55, April 2013

- M. Schmidt, A. Senger, M. Hauth, C. Freier, V. Schkolnik, and A. Peters. A mobile high-precision absolute gravimeter based on atom interferometry. *Gyroscopy and Navigation*, 2(3):170–177, August 2011

- V. Schkolnik, B. Leykauf, M. Hauth, C. Freier, and A. Peters. The effect of wavefront aberrations in atom interferometry. pp. 1–12, November 2014. arXiv:1411.7914

- D. N. Aguilera, H. Ahlers, B. Battelier, A. Bawamia, A. Bertoldi, R. Bondarescu, K. Bongs, P. Bouyer, C. Braxmaier, L. Cacciapuoti, C. Chaloner, M. Chwalla, W. Ertmer, M. Franz, N. Gaaloul, M. Gehler, D. Gerardi, L. Gesa, N. Gürlebeck, J. Hartwig, M. Hauth, O. Hellmig, W. Herr, S. Herrmann, A. Heske, A. Hinton, P. Ireland, P. Jetzer, U. Johann, M. Krutzik, A. Kubelka, C. Lämmerzahl, A. Landragin, I. Lloro, D. Massonnet, I. Mateos, A. Milke, M. Nofrarias, M. Oswald, A. Peters, K. Posso-Trujillo, E. M. Rasel, E. Rocco, A. Roura, J. Rudolph, W. P. Schleich, C. Schubert, T. Schuldt, S. Seidel, K. Sengstock, C. F. Sopuerta, F. Sorrentino, D. Summers, G. M. Tino, C. Trenkel, N. Uzunoglu, W. von Klitzing, R. Walser, T. Wendrich, A. Wenzlawski, P. Weßels, A. Wicht, E. Wille, M. Williams, P. Windpassinger, and N. Zahzam. STE-QUEST—Test of the universality of free fall using cold atom interferometry. *Classical and Quantum Gravity*, 31(11):115010, June 2014

- G. M. Tino, F. Sorrentino, D. N. Aguilera, B. Battelier, A. Bertoldi, Q. Bodart, K. Bongs, P. Bouyer, C. Braxmaier, L. Cacciapuoti, N. Gaaloul, N. Gürlebeck, M. Hauth, S. Herrmann, M. Krutzik, A. Kubelka, A. Landragin, A. Milke, A. Peters, E. M. Rasel, E. Rocco, C. Schubert, T. Schuldt, K. Sengstock, and A. Wicht. Precision Gravity Tests with Atom Interferometry in Space. *Nuclear Physics B - Proceedings Supplements*, 243-244:203–217, October 2013

- F. Sorrentino, K. Bongs, P. Bouyer, L. Cacciapuoti, M. D. Angelis, H. Dittus, W. Ertmer, J. Hartwig, M. Hauth, S. Herrmann, K. Huang, M. Inguscio, E. Kajari, T. Köne-

mann, C. Lämmerzahl, A. Landragin, G. Modugno, F. Pereira Dos Santos, A. Peters, M. Prevedelli, E. M. Rasel, W. P. Schleich, M. Schmidt, A. Senger, K. Sengstock, G. Stern, G. M. Tino, T. Valenzuela, R. Walser, and P. Windpassinger. The Space Atom Interferometer project: status and prospects. *Journal of Physics: Conference Series*, 327:012050, December 2011

- F. Sorrentino, K. Bongs, P. Bouyer, L. Cacciapuoti, M. Angelis, H. Dittus, W. Ertmer, A. Giorgini, J. Hartwig, M. Hauth, S. Herrmann, M. Inguscio, E. Kajari, T. T. Könemann, C. Lämmerzahl, A. Landragin, G. Modugno, F. Pereira Dos Santos, A. Peters, M. Prevedelli, E. M. Rasel, W. P. Schleich, M. Schmidt, A. Senger, K. Sengstock, G. Stern, G. M. Tino, and R. Walser. A Compact Atom Interferometer for Future Space Missions. *Microgravity Science and Technology*, 22(4):551–561, September 2010

- T. Schuldt, C. Schubert, M. Krutzik, L. G. Bote, N. Gaaloul, J. Hartwig, H. Ahlers, W. Herr, K. Posso-Trujillo, J. Rudolph, S. Seidel, T. Wendrich, W. Ertmer, S. Herrmann, A. Kubelka-Lange, A. Milke, B. Rievers, E. Rocco, A. Hinton, K. Bongs, M. Oswald, M. Franz, M. Hauth, A. Peters, A. Bawamia, A. Wicht, B. Battelier, A. Bertoldi, P. Bouyer, A. Landragin, D. Massonnet, T. Lévèque, A. Wenzlawski, O. Hellmig, P. Windpassinger, K. Sengstock, W. von Klitzing, C. Chaloner, D. Summers, P. Ireland, I. Mateos, C. F. Sopuerta, F. Sorrentino, G. M. Tino, M. Williams, C. Trenkel, D. Gerardi, M. Chwalla, J. Burkhardt, U. Johann, A. Heske, E. Wille, M. Gehler, L. Cacciapuoti, N. Gürlebeck, C. Braxmaier, and E. Rasel. Design of a dual species atom interferometer for space. December 2014. arXiv:1412.2713, accepted for Experimental Astronomy

Own Oral Presentations

- M. Hauth, C. Freier, V. Schkolnik, H. Wziontek, A. Peters.
  Das Gravimetric Atom-Interferometer (GAIN), Funktionsweise und Vergleichsmessung mit dem SG-30 in Wettzell
  Herbsttagung des Arbeitskreises Geodäsie/Geophysik, 2014

- M. Hauth, C. Freier, V. Schkolnik, A. Peters.
  GAIN - a portable Atom Interferometer for on site Measurements of Local Gravity
  Frontiers in Optics 2013, volume 113, p. LM4H.2, Washington D.C., April 2013, OSA

- M. Hauth, C. Freier, V. Schkolnik, A. Senger, M. Schmidt, A. Peters.
  Gravity measurements with the mobile atom-interferometer GAIN.
  DPG Tagung Hannover 2013, Q 38.5

- M. Hauth, C. Freier, V. Schkolnik, A. Senger, M. Schmidt, A. Peters.
  Erste Gravitationsmessungen mit dem Atom-Interferometer GAIN.
  Herbsttagung des Arbeitskreises Geodäsie/Geophysik, 2012

- M. Hauth, M. Schmidt, A. Senger, C. Freier, V. Schkolnik, A. Peters.
  GAIN — a high-precision mobile gravimeter based on atom interferometry.
  Frontiers of Matter Wave Optics, 2011

- M. Hauth, M. Schmidt, A. Senger, V. Schkolnik, C. Freier, A. Peters.
  Atom Interferometry in a mobile high-precision setup to measure local gravity.
  DPG Tagung Dresden 2011, Q 25.2

- M. Hauth, V. Schkolnik, C. Freier, A. Senger, M. Schmidt, A. Peters.
  A mobile high-precision atom interferometer to measure local gravity.
  Young Atom Opticians conference 2010

- M. Hauth, M. Schmidt, A. Senger, S. Grede, C. Freier, A. Peters.
  Atom Interferometry in a mobile setup to measure local gravity.
  WE-Heraeus-Physikschule: Frontiers in Matter-Wave Interferometry, 2010

Own Poster Presentations

- M. Hauth, V. Schkolnik, C. Freier, A. Senger, M. Schmidt, A. Peters.
  A mobile high-precision atom interferometer to measure local gravity.
  DPG Tagung Stuttgart 2012, Q 34.87

- M. Hauth, M. Schmidt, A. Senger, S. Grede, C. Freier, A. Peters.
  Atom interferometry - From thought experiment to application.
  Opening IRIS Adlershof, 2010

- M. Hauth, A. Senger, M. Schmidt, S. Grede, C. Freier, A. Peters.
  Atom Interferometry in a mobile setup to measure local gravity.
  DPG Tagung Hannover 2010, Q 21.33

List of Figures

List of Tables

List of Abbreviations

AG	absolute gravimeter
AOM	acousto-optic modulator
ASD	amplitude spectral density
BKG	Bundesamt für Kartographie und Geodäsie
CAD	computer-aided design
DDS	direct digital synthesizer
DFB	distributed feedback laser
ECAG	European Comparison of Absolute Gravimeters
ECDL	extended cavity diode laser
ESA	European Space Agency
FPGA	field programmable gate array
GAIN	Gravimetric Atom Interferometer
IERS	International Earth Rotation and Reference Systems Service
IfE	Institut für Erdmessung
MOPA	master oscillator power amplifier
MOT	magneto-optical trap
MTS	modulation transfer spectroscopy
NA	numerical aperture
PBS	polarizing beam splitter
PFD	phase frequency detector
PI	proportional-integral
PM	polarization maintaining
PMT	photomultiplier tube
PSD	power spectral density
RF	radio frequency
SG	superconducting gravimeter
STE-QUEST	Space-Time Explorer and Quantum Equivalence Principle Space Test
TA	tapered amplifier
RWA	rotating wave approximation
SAI	Space Atom Interferometer
UFF	universality of free fall
UHV	ultra-high vacuum
UTC	coordinated universal time

Acknowledgments

It is time to thank all those people who participated in this project and supported me during this work. Without their help this project would not have been possible.

First of all, I would like to thank my supervisor Achim Peters who gave me the opportunity to work on this project. I could develop and realize my own ideas and I could profit from his in-depth expertise in physics and especially in atom interferometry. In his group I could also gain experience on conferences and in European collaborations while working for the STE-QUEST project.

Second, I thank the GAIN fellow campaigners Christian Freier and Vladimir Schkolnik. The progress in so many aspects of this project and the measurement campaigns would not have been possible without this team work. Thanks to Christian also for proof-reading this work.

Special thanks go to Hartmut Wziontek from the BKG and to Manuel Schilling, Olga Gitlein and Ludger Timmen from the IfE who helped with the appropriate gravity models and parameters. They contributed with their gravimeters and also their experience to the successful comparison campaigns.

I also want to thank Klaus Palis, Eugen Dischke and Matthias Schoch for their help in designing electronics and programming of microcontrollers and all members of the work group for the nice atmosphere.

Finally, I would like to thank my family and friends for all their support.

Selbständigkeitserklärung

Ich erkläre, dass ich die vorliegende Arbeit selbständig und nur unter Verwendung der angegebenen Literatur und Hilfsmittel angefertigt habe. Ich habe mich anderweitig nicht um einen Doktorgrad beworben und besitze einen solchen auch nicht. Die dem Verfahren zugrunde liegende Promotionsordnung der Mathematisch-Naturwissenschaftlichen Fakultät der Humboldt-Universität zu Berlin habe ich zur Kenntnis genommen.

Berlin, den 20.01.2015 Matthias Hauth